AN ABSTRACT OF THE THESIS OF

Ronald Blair Baker for the degree of Master of Science in Mechanical Engineering presented on December 13, 1976.

Title: Modeling the Thermal Effects of Fabricated Fuel-to-Cladding Gap in Fast Reactor Fuel

Redacted for Privacy

Abstract approved: _____

Dr. R. E. Collingham

This report presents a refined method for the calculation of fuel centerline temperatures and the linear-heat-rating-to-incipient melting, Q'_m, of mixed-oxide fuel typical of that to be used in the Fast Flux Test Facility and in Liquid Metal Fast Breeder Reactors. Of primary concern are the effects of the fabricated fuel-to-cladding gap and accumulated burnup up to 10,900 MWd/MTM (1.1 At%) on the thermal performance of the fuel pins. Specifically described in this report are:

1) The analysis and normalization of fuel thermal performance data from two unique fast reactor fuel tests. The effect of fabricated gap size on "integral" Q'_m is developed.
2) A proposed set of heat transfer formulations and corresponding material properties for modeling the radial heat transfer path through the fuel and cladding.

3) The calibration of a fuel-to-cladding gap conductance model, which is part of a thermal performance computer code incorporating the expressions from item 2, to the data developed from the analyses in item 1.

The data used in this study are from the HEDL P-19 and P-20 experiments which were irradiated in the Experimental Breeder Reactor 2, EBR-II, for the Hanford Engineering Development Laboratory, HEDL.

Modeling the Thermal Effects of Fabricated Fuel-to-Cladding Gap in Fast Reactor Fuel

by

Ronald Blair Baker

A THESIS

submitted to

Oregon State University

in partial fulfillment of
the requirements for the
degree of

Master of Science

Completed December 13, 1976

Commencement June 1977

APPROVED:

Redacted for Privacy

Professor of Mechanical Engineering in Charge of Major

Redacted for Privacy

Head of Department of Mechanical Engineering

Redacted for Privacy

Dean of Graduate School

Date thesis is presented December 13, 1976

Typed by Robin E. Horton for Ronald B. Baker

ACKNOWLEDGEMENTS

The author gratefully acknowledges the encouragement, guidance and suggestions of Dr. R. E. Collingham, of the Joint Center for Graduate Study, and Dr. R. D. Leggett, of the Westinghouse Hanford Company, in the development of this thesis. Further, I would like to acknowledge the technical advice from Mr. D. S. Dutt, and the assistance of Mrs. B. B. Pravato in compilation of portions of this work.

Irradiation experiments such as HEDL P-19 and P-20 draw upon talents and expertise of many people. I would particularly like to acknowledge the major contributions of J. E. Hanson in test conception and definition, E. O. Ballard (now with LASL) in test design, and S. A. Chastain in the coordination of postirradiation examination.

The author would also like to take this opportunity to acknowledge the help and support of his wife, D'Arcy, and the patience of his children, Angela and Aaron, who also endured the "long hours" that made this thesis possible.

This research is based on work that was done at the Hanford Engineering Development Laboratory, operated by the Westinghouse Hanford Company under contract to the United States Energy Research and Development Administration.

TABLE OF CONTENTS

LIST OF ILLUSTRATIONS

LIST OF ILLUSTRATIONS (Cont'd)

LIST OF ILLUSTRATIONS (Cont'd)

MODELING THE THERMAL EFFECTS OF FABRICATED FUEL-TO-CLADDING GAP IN FAST REACTOR FUEL

A.1 Introduction

This thesis presents analyses made to refine the calculation of centerline temperature and the linear-heat-rating needed to cause incipient melting, Q'_m, of mixed-oxide (75% UO_2 - 25% PuO_2) fuel typical of that to be used in the driver assemblies of the Fast Flux Test Facility, FFTF (Figure 1). The results also have direct application to Liquid Metal Fast Breeder Reactor, LMFBR, fuel pins. The analysis is specifically concerned with the effects of fabricated fuel-to-cladding gap and accumulated fuel burnup up to 10,900 MWd/MTM (1.1 At%) on the thermal performance of the fuel pins. The data used in this analysis are from the HEDL P-19 and P-20 experiments which were irradiated in the Experimental Breeder Reactor 2, EBR-II, for the Hanford Engineering Development Laboratory, HEDL.

The fuel and cladding system of interest in this analysis, Figure 1, is made up of a cladding with an outside diameter, OD, of 0.230 inch (0.58 cm) and an inner diameter, ID, of 0.200 inch (0.51 cm). The fuel contained in this cladding is normally fabricated with a diameter about 0.005 inch (0.13 mm) less than the ID of the cladding. For all calculational purposes in this report it is assumed the fuel is concentric within the cladding ID. The pin plenum and gap between the fuel and cladding are originally filled with a gas mixture of 90% He + 10% (Xe + Kr) in present FFTF/LMFBR fuel pins. The majority of the data used in this report, however, are from pins which were back-filled with pure He. Only radial heat transfer is assumed in this study because the length, 36 inches (81 cm) for FFTF pins and 13.5 inch (34 cm) for the test pins,

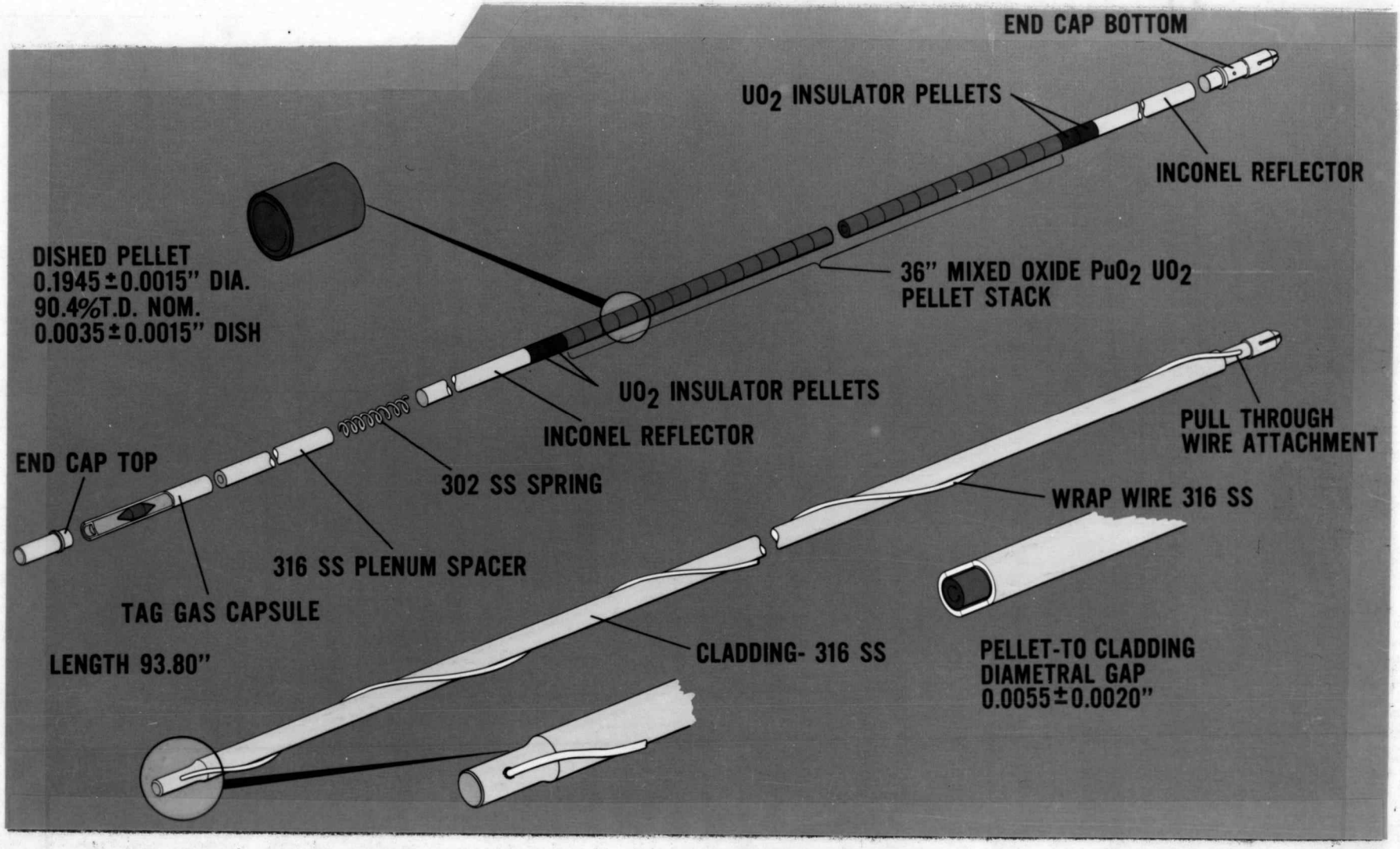

Figure 1. Schematic Illustration of the FFTF Driver Fuel Pin

of the fuel columns is much greater than the radii of the fuel and cladding involved.

During irradiation, a number of changes occur in the fuel and cladding early in life. Cracks form in the fuel due to thermal stresses and the fuel-to-cladding gap tends to close due to fuel swelling and crack healing mechanisms. The fuel and cladding also naturally expand due to increased temperatures. The solid ceramic fuel operating at high, greater than 10 kW/ft (330 W/cm), linear heat rates develop fuel restructuring regions. Normally an inner radius of high density columnar grains form and a corresponding central void of significant proportions is also created. Gases, both absorbed during fabrication (H, N_2 and Ar) and those generated from fissioning (Xe and Kr) in the fuel, are released to the gap and fuel pin plenum, this results in lower thermal conductivity gas in the gap. If temperatures are high enough, about 5000°F (2760°C), the fuel will begin to melt and can relocate in the central void under the influence of gravity and/or gas pressure.

The calculation of fuel centerline temperature is of interest to LMFBR's because reactor design limits normally require that there be a low probability of fuel melting even during a 15% overpower condition. This requirement has a direct effect on the steady state power limit of the fuel element and the reactor. Optimization of this power is important to reactor thermal efficiency and economy of operation. Design factors, that are probably unnecessarily conservative because of a small data base, are applied in fuel temperature calculations causing a penalty in power limits that may not be needed. This uncertainty also causes very conservative fuel-to-cladding gap specification tolerances

to be used (requiring grinding of each fuel pellet) which increases fuel fabrication costs.

The calculation of fuel centerline temperatures in the complex heat transfer system of the fuel pin is difficult. With the edge of the central void of a typical "fresh" experimental fuel pin, (assuming a 0.005 inch diametral fuel-to-cladding gap), at the melting point, the temperature drop across the hot radial gap is about 800°F (430°C), and the drop across the fuel itself is about 2300°F (1650°C). Looking at the calculation of radial temperature drops from the coolant to the fuel melt boundary we have:

$$(A)\quad \int_{T_I}^{T_m} dT = \Delta T_{Fl} + \Delta T_C + \Delta T_G + \Delta T_F + \Delta T_{RF}$$

where

T_m = Melting temperature of fuel

T_I = Sodium coolant temperature

ΔT_{Fl} = Temperature drop between coolant and cladding

ΔT_C = Temperature drop through cladding

ΔT_G = Temperature drop through fuel-to-cladding gap

ΔT_F = Temperature drop through unrestructured fuel region

ΔT_{RF} = Temperature drop through restructured fuel regions.

There are two methods of characterizing this heat transfer system with respect to melting. The right side of Equation A can be used, with each regions' temperature drop being characterized from the coolant to the fuel center, or the left side can be used, looking only at the "integral" effect based on prototypic test data.

Using the right side of Equation A to calculate fuel temperatures at linear heat rates high enough to cause melting results in a large uncertainty. The characterization of the temperature drops in the gap and fuel is not simple. Each has significant uncertainty due its complexity, the present "state of the art" of understanding and the limited data base. For example, calculation of the temperature drop across the gap depends on the hot gap size, the gas composition in the gap, interface pressure, gas pressure, and the surface conditions of the fuel and cladding. The thermal conductivity of the mixed-oxide fuel depends on temperature, density, size and shape of porosity, the oxygen-to-metal-ratio, (O/M), and perhaps several other parameters. Uncertainty for fuel conductivity above 1700°C is large because of very little data being available. Further, for calculating fuel temperatures the size of the columnar grain region and central void, and the density of the columnar grain must be calculated since these have a significant effect on fuel temperatures (in a high power fuel the centerline temperature can drop as much as 600°F due to restructuring). Development of the columnar grain region and central void is generally qualitatively understood but prediction of them still involves significant uncertainty.

The characterization of individual temperature drops, the right side of Equation A, and the summing of corresponding uncertainties led to the development of "integral" heat-rating-to-incipient fuel melting, Q'_m, ("power-to-melt") tests to decrease uncertainties. These tests, in effect, use the left hand side of Equation A. These experiments, based on prototypic parameters, result in Q'_m values which can be applied to

reactor design with a minimum of additional calculation. Uncertainty is mainly reduced to characterizing local linear heat rates in the test fuel. The HEDL P-19 and P-20 tests were conducted to develop integral data for FFTF. The fuel pins and test operating conditions were as near prototypic of the FFTF design as possible. The prime concern and variable was fabricated fuel-to-cladding gap size because of the major uncertainty in calculating fuel-to-cladding gap conductance.

The HEDL P-19 test was irradiated to investigate the effects of initial fuel-to-cladding gap size on Q'_m at beginning-of-life (BOL) conditions[1][3][4]. It included 0.230 inch OD fuel pins, and 0.250 inch OD pins to assure sufficient heat generation to have partial fuel melting in a major number of the pins. The P-20 test followed and was designed to determine the effects of fuel burnup up to 10,900 MWd/MTM on Q'_m at several different gap sizes[2][4].

The data from the HEDL P-19 test provided the basis for establishing the specifications for fuel-to-cladding gap size in the FFTF driver fuel pins in order to assure that the fuel has the capability for 400 MW reactor operation under the most severe "design" conditions. P-19 and P-20 simulated the most severe history expected for a 15% overpower in the FFTF.

Normalization of the "integral" Q'_m data from the tests is necessary since the experimental values of Q'_m are derived at different coolant temperatures, pellet densities (in some cases) and, as noted previously, sometimes different fuel and cladding OD sizes. All the Q'_m values need to be adjusted to a single set of design conditions. This type analysis

requires an understanding of the heat transfer mechanisms used on the right side of Equation A but involves a minimum of adjustment calculations, thus minimizing introduced uncertainty. The final result in this analysis is a curve of normalized Q'_m values as a function of fabricated fuel-to-cladding gap.

However, there are several reasons for which the calculations considering the temperature drops through all the regions, the right side of Equation A, are required. First it is needed to the study Q'_m predictions for advanced fuels and/or operating conditions where the parameters deviate significantly from the integral tests. Secondly, there is a need for predicting fuel temperatures at linear heat rates lower than Q'_m, where the fuel will normally be operating under steady state conditions. Thus calibrated thermal performance digital computer codes which in effect calculate values for, or model, the right side of Equation A have been and are being developed.

Since a known isotherm in the fuel occurs at the extent of melting, data from the integral P-19 and P-20 experiments can be used directly for calibrating fuel thermal performance codes. At Q'_m these provide an in-reactor check on the total integral calculation.

The P-19 and P-20 experiments represent a unique set of data in the United States fast reactor program. Only one other test, the General Electric F-20[79] test, resulted in this type of data. Complete results of the F-20 test remain to be published but are expected to extend the data ranges found in these analyses. The use of the known isotherm in

the fuel that occurs at the extents of fuel melting provides the best available data to date, for calibrating fuel thermal performance models. Other possible methods for measuring temperatures introduce "something extra", i.e. thermocouples or melt wires, into the fuel which may effect the results. Further, because of the high temperatures and environment involved, tests using these other methods in fast reactor fuel have been used very little in the U.S.

Using the P-19 and P-20 data the later portion of this thesis describes the calibration of the gap conductance model in a revised version of the SIEX[5] thermal performance code. Because of the nature of the model involved information from other work is also used. The gap conductance model was chosen to be calibrated because, as noted previously, it is considered to have the most significant uncertainty in the calculation of fuel temperatures. Prior to calibration of the model, summaries of the heat transfer formulations used in the revised code, SIEX-M1, are made and reviews of related material properties are discussed. Here the effort was made to choose the most realistic models possible for calculating the radial temperature drops over each region. As is seen by Equation A any gap conductance model calibrated using integral Q'_m data is meaningful only if the complete heat transfer path is specified since assumptions made for the other region models are not unique. The gap conductance model and heat transfer system developed in this manner will have a minimum of uncertainty in predicted fuel temperature drops through each region and in the system as a whole.

The SIEX[5] thermal performance code was chosen for calibration purposes because of the author's involvement in its development and its successful and extensive use at HEDL[8] for fast reactor fuel prediction. It offers quick running times and the ability to be correlated to large data bases. Other codes in use in the U.S., GAPCON[6], FMODEL[23], LIFE[77] and UNCLE[78] use methods similar to those used in versions of SIEX for calculating gap conductance though detailed assumptions vary considerably.

The HEDL P-19 data have been previously described in past reports[1][3] with preliminary analyses. Similarly, P-20 data have been reported[2][4] and preliminary analyses discussed. The current analysis of the raw data is the first one using the combined P-19 and P-20 results with the same analysis tools, and should reflect the best analysis to date. The present study incorporates many analysis refinements not used on the data previously (i.e. special handling of fuel restructuring and use of the SIEX thermal performance code). All measurements from P-19 ceramography were remeasured as part of these analyses to assure the same criteria were applied in interpreting the observations as were used for P-20 data. On the whole the P-19 measurements changed very little. In addition, a change in power levels used for the P-19 experiment (and thus P-20) has also been made. This power adjustment reflects more detailed analyses[71] made by the EBR-II project to establish the actual power the reactor is running at.

Appendix C includes summary descriptions of the nomenclature used in this report which may not be familiar to those not working

directly in this field. It also includes definition of mathematic variables and constants used in the later portion of this thesis.

A.2 Summary

The object of this study is to:

1) Make a refined analysis of the combined results of experiments HEDL P-19 and P-20 to find the integral linear-heat-rate-to-cause incipient fuel melting, Q'_m.

2) Set forth a realistic set of mathematical models for the radial heat path from the fuel centerline to coolant.

3) Use the experimental data, item 1, with the mathematical models, item 2, to calibrate a fuel-to-cladding gap conductance model.

The data from the HEDL P-19 and P-20 test represent a unique set of information in the U.S. fast reactor program. The HEDL P-19 test was irradiated to investigate the effects of initial fuel-to-cladding diametral gap sizes, from 0.003 to 0.010 inch (.08 to .25 mm), on Q'_m at beginning-of-life conditions. The P-20 test was irradiated primarily to determine the effects of fuel burnup to 10,900 MWd/MTM on Q'_m at several selected diametral gap sizes, 0.0035, 0.0055 and 0.0075 inch (.09, .14, and .19 mm). Both experiments were designed to be "integral" power-to-melt tests, the fuel pin fabrication and operating parameters simulating FFTF/LMFBR design conditions.

Results from the final combined analysis, and normalization of data, at beginning-of-life conditions (60 to 90 MWd/MTM) to a single set of fuel and operating conditions show a definite dependence of Q'_m on fabricated fuel-to-cladding gap size. The normalized Q'_m values varied from 18.3 to 14.8 kW/ft (600 to 490 W/cm), Figure 11. Apparent closure

of the hot gap occurred at fabricated diametral gaps of about 0.005 inch for this "fresh" fuel. The effect of having lower conductivity fill-gas mixture (18% Xe - 82% He instead of pure He) was a significant decrease in Q'_m, as expected. A reason for the scatter in data between the two tests at a diametral gap of 0.0055 inch was not found however several possibilities were identified.

The results of the higher burnup data show that by the time a burnup of about 3700 MWd/MTM is reached, Q'_m is at least 18.5 kW/ft in a prototypic (except in length) FFTF/LMFBR mixed-oxide fuel pin and is essentially independent of starting fuel-to-cladding gap size Figure 12. This represents, for the 0.0075 inch gap case, an improvement in Q'_m of about 20% relative to "fresh" fuel (60 to 90 MWd/MTM). This improvement comes about primarily by rapid closure of the fuel-to-cladding gap, due to the fuel moving outward by cracking and crack healing mechanisms. Improvement is also caused by additional fuel restructuring.

These later test results indicate that with a short conditioning period (3700 MWd/MTM or about 12 equivalent full power days) the thermal rating of an LMFBR can be increased by at least 20%. Further, restrictive limits on maximum fabricated fuel-to-cladding gap sizes can be relaxed, which could result in more viable fuel fabrication processes.

The data from these two experiments represent the best information to calibrate fuel pin thermal performance models to; the molten fuel extent represents a known isotherm. This allows, with the use of mathematical heat transfer models for the rest of the radial heat path, the calibration of the model with the most significant uncertainty

associated it, the fuel-to-cladding gap conductance model. Once this model is calibrated and using heat transfer formulations developed for the rest of the radial path a basic heat transfer model for the fuel-cladding system is established. This can be used as the basis for a thermal performance code for LMFBR fuel pins under many conditions. Later, using a larger data base, fuel behavior models, such as for fuel restructuring and fission gas release, can be combined with it to make a total predictive package.

An analysis of the heat transfer formulations used for the fuel-cladding radial heat path was made. The SIEX[5] thermal performance code was the starting point because of the past ability of it to make satisfactory predictions for LMFBR type fuel. Material property models were also developed. A proposed set of heat transfer models consistant with the apparent "state of the art" resulted. Particular emphasis was placed on the complex heat transfer system at the fuel-to-cladding gap. The conclusion of the analysis in this regard was the continued use of the gap conductance model proposed by Ross and Stoute[7] was entirely satisfactory.

Hot fuel-to-cladding gaps must be predicted as part of the modeling of gap conductance. Models characterizing these were developed based on the HEDL P-19 and P-20 data. A postirradiation residual fuel-to-cladding gap, the gap size observed at room temperature ("cold"), model was correlated to measurements made from transverse ceramography from the test pins. The model developed, Equation 40, is dependent on original gap size, local power, local burnup, reactor cycles and irradiation

history. It agrees well with the data, Figure 21. Other observations of fuel behavior led to the conclusion of using the radial integral of thermal expansion for the fuel, rather than a radial average value, in calculating the final fuel-to-cladding hot gap.

Using the set of proposed heat transfer formulations, material properties, and fuel-to-cladding gap closure models the three constants in the gap conductance model were calibrated using the experimental Q'_m data. These constants are basically corrections concerned with the effects of the "waviness" of the fuel and cladding surfaces. The two constants dealing with solid-to-solid contact could not be uniquely determined and thus one was set based laboratory results and model behavior; and the other calibrated. The resulting calibrated gap conductance model and radial heat transfer formulations appear to model the heat transfer system of the fuel pins well. This is evidenced for the "fresh" pins by the comparison shown in Figure 24 of Q'_m data and predictions (SIEX-M1). At higher fuel burnups (up to 10,900 MWd/MTM) the model predictions also agree well with the available data points and lower bound data, Figure 23. It is believed this model represents a refined predictive system for <u>in-reactor</u> fuel performance.

Surface roughness of the test fuel and cladding was not measured (it is recommended in the near future these measurements should be made from archive samples) thus direct comparison of the constants derived in laboratory work and from this work cannot be made. However, the calibrated constants from this work compare well with those found by Ross and Stoute[7] for zircaloy and UO_2 material pairs using typical values for roughness.

B Derivation of Integral Power-to-Melt Curves Based on HEDL P-19 and P-20 Test Results

The following summarizes the analysis of the HEDL P-19 and P-20 test with respect to the linear heat-rating-to-incipient fuel melting, Q'_m, which is also referred to as "power-to-melt." At all times as little as possible manipulation of the data is made to retain the advantage of an integral type test, run very near the conditions required in the fuel pin design of interest (FFTF driver type fuel pins). Some normalization of the data is necessary however, in order that data from the 0.250 inch (0.635 cm) OD pins can be applied to the 0.230 inch (0.584 cm) OD type fuel pins of direct interest, and so Q'_m data taken at different cladding temperatures can be used and compared. There is also the experimental need to verify similarity of behavior of the different fuels under different operating conditions.

B.1.a Summary of the HEDL P-19 test

The experiment HEDL P-19, was conducted in EBR-II to determine the effect of initial, cold, diametral fuel-to-cladding gap, from 0.0034 to 0.010 inches (0.086 to 0.254 mm), on the linear-heat-rating (Q'_m) required to cause incipient fuel melting in mixed-oxide (25% PuO_2 - 75% UO_2) fuel pins under very rapid LMFBR startup conditions. P-19 was a nineteen (encapsulated) pin subassembly, Figure 2, consisting of eight 0.230 inch OD pins, eight 0.250 inch OD pins and three preirradiated elements. All pins were backfilled with pure helium. The "fresh" pins were clad with 316 SS (20% CW) and were fabricated to RDT Standards for LMFBR fuel. Appendix A of Reference 4 summarizes detailed fabrication

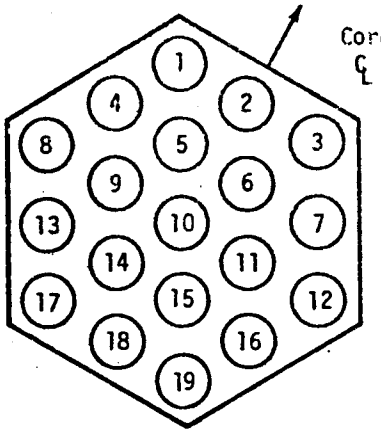

EBR-II GRID
POSITION 2B1

CAPSULE IDENTIFICATION NUMBER	SUBASSEMBLY LOCATION NUMBER	FUEL PIN DIAMETER, IN.	NOMINAL FUEL-CLADDING DIAMETRAL GAP, IN.	NOMINAL PELLET DIAMETER, IN.
P-19-8	1	0.230	0.010	0.190
PNL-2-16	2	0.238	PREIRRAD.	0.212**
P-19-20	3	0.230	0.010	0.190
P-19-35	4	0.230	0.0072†	0.193
P-19-13	5	0.230	0.008	0.192
P-19-2	6	0.230	0.008	0.192
P-19-5	7	0.230	0.006	0.194
P-19-3R	8	0.250	0.010	0.208
P-19-6	9	0.230	0.004	0.196
PNL-1-11	10	0.250	PREIRRAD.	0.212**
P-19-33	11	0.230	0.0049†	0.195
P-19-24R	12	0.250	0.010	0.208
P-19-26R	13	0.250	0.006	0.212
P-19-25R	14	0.250	0.008	0.210
P-19-30	15	0.250	0.0070†	0.211
P-19-7R	16	0.250	0.006	0.212
P-19-27R	17	0.250	0.004	0.214
PNL-2-18	18	0.238	PREIRRAD.	0.212**
P-19-28	19	0.250	0.0034†	0.215

**INITIAL

† AS-SINTERED

HEDL 7506-117.15

Figure 2. Fuel Pins Used in HEDL P-19 Test Assembly

data for the P-19 test pins, Table I shows data of direct interest to this analysis.

The P-19 test was conducted to simulate a fast startup to steady state power. After a one hour hold period, power was then increased rapidly an additional 15 percent. This level was held ten minutes, and the reactor was then scrammed (see Figure 3) to quench the fuel structure.

The P-19 experiment (X108) was irradiated in row 2, position 2B1 in the EBR-II. The subassembly loading is shown in Figure 2. The positions immediately adjacent to the test were occupied by driver fuel assemblies[67].

After irradiation, the P-19 pins were removed from EBR-II and neutron radiographed. This confirmed partial fuel melting in a number of pins. All 0.230 inch OD pins with fuel-to-cladding gaps equal to or less than 0.0055 inch had no fuel melting. The remaining 0.230 inch OD pins and all the 0.250 inch OD pins experienced partial melting. The capsules were then returned to HEDL where detailed destructive examination was conducted.

Transverse ceramographic sections were used to obtain measurements of fuel restructuring zone radii and residual fuel-to-cladding gap. They were also used to obtain the radial extent of melting at the peak power locations of those pins experiencing partial fuel melting. However, power-to-melt, Q'_m, data calculated from these sections were considered less accurate because of the uncertain influence of relocated molten fuel on local power. While this relocation must be relatively small, no more than 4 percent, it is believed to have contributed to

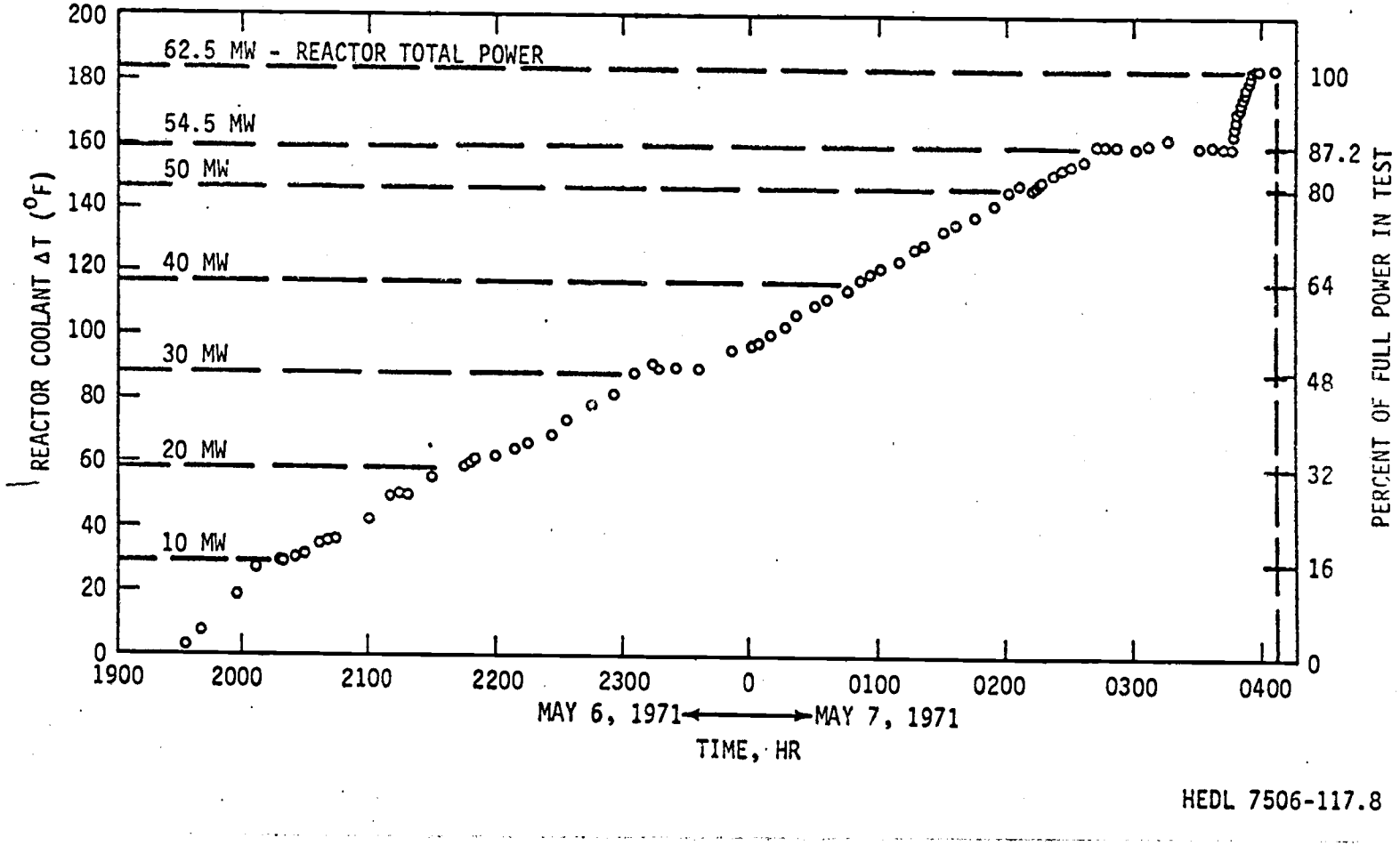

Figure 3. Power History During HEDL P-19 Test

TABLE I

SUMMARY OF FABRICATION PARAMETERS FOR EACH P-19 PIN

Capsule Ident. Number	Avg. Fuel Dia. (in.)	Avg. Pellet Density (% TD)	Average Cladding Dimensions (in.)		Fuel Column Length (in.)	Average Fuel-Cladding Gap (in.)
			ID	OD		
P-19-2	0.1922±0.0002	90.75	0.2000±0.0001	0.2304±0.0001	13.4286	0.0078±0.0003
P-19-3R	0.2078	92.40	0.2178	0.2503	13.4595	0.0100
P-19-5	0.1943	90.75	0.2000	0.2304	13.4842	0.0057
P-19-6	0.1962	90.75	0.2001	0.2304	13.4253	0.0039
P-19-7R	0.2117	92.40	0.2179	0.2504	13.4740	0.0062
P-19-8	0.1903	90.75	0.1999	0.2303	13.4970	0.0096
P-19-13	0.1922	90.75	0.2000	0.2303	13.4011	0.0078
P-19-20	0.1903	90.75	0.2000	0.2302	13.5327	0.0097
P-19-24R	0.2078	92.40	0.2178	0.2502	13.4547	0.0100
P-19-25R	0.2098	92.40	0.2178	0.2501	13.4565	0.0080
P-19-26R	0.2117	92.40	0.2177	0.2501	13.4791	0.0060
P-19-27R	0.2137	92.40	0.2177	0.2502	13.5511	0.0040
P-19-28(a)	0.2147	92.40	0.2181	0.2502	13.4857	0.0034
P-19-30(a)	0.2108	92.40	0.2179	0.2401	13.4678	0.0070
P-19-33(a)	0.1943	90.75	0.1992	0.2300	13.5845	0.0049
P-19-35(a)	0.1920	90.75	0.1992	0.2300	13.5701	0.0072
PNL-1-11	0.2120±0.0005	89.45	0.2180±0.0002	0.2498±0.0001	13.4060	0.0060±0.0007
PNL-2-16	0.2120±0.006	90.57	0.2181	0.2380±0.0003	13.4680	0.0061±0.0008
PNL-2-18	0.2122±0.003	90.05	0.2181	0.2375±0.005	13.4680	0.0059±0.0005

(a) Pellet surfaces in the as-sintered condition. All other pins contained ground pellets.

the moderate scatter found in the Q'_m values calculated from these data.

It was judged that the axial extents of melting, as determined from longitudinal ceramographic sections, offered the best data for determining Q'_m since these sections experienced the least variation due to molten fuel relocation. Local generated power and temperatures are highest near the axial midplane and decrease toward each end of the fuel column, as will be discussed later. These longitudinal sections also allowed direct evaluation of whether a once molten fuel plug was present and should represent incipient melting positions.

B.1.b Summary of HEDL P-20 Test

The primary purpose of the P-20 test was to determine the effect of burnup, up to 1.1 At.% (about 10,900 MWd/MTM) on power-to-melt, Q'_m, over a range of fuel-to-cladding gaps of interest to LMFBR's. Table II summarizes the experiment variables and general fabrication parameters. Table III summarizes specific pin data.

The pins with 0.0035, 0.0055, or 0.0075 inch (0.099, 0.14 or 0.19 mm) fuel-to-cladding diametral gaps constitute the main portion of the test since these span the present allowable range in FFTF driver and LMFBR fuel pins. These pins were backfilled with pure helium to permit a direct comparison of the results with the HEDL P-19 results. Several pins with 0.0075 inch fuel-to-cladding gaps were included that were back-filled with 82% He-18% Xe to assess the effect of "tag" gas on thermal performance. (FFTF driver and LMFBR fuel pins will be filled, "tagged" with a 90% He-10% (Xe+Kr) mixture with predetermined ratios of

TABLE II

SCOPE OF HEDL P-20 THERMAL PERFORMANCE TEST

General Parameters

Cladding

316 20% CW stainless steel

0.230" OD x 0.015" wall thickness

Fuel

75% UO_2 x 25% PuO_2

Preslugged (High pressure) same as P-19

O/M - 1.96

Pellet density ∿ 91.% (similar to P-19, 0.230 inch OD pins)

He bonded to cladding

13.5" fuel column length

Subassembly

19 encapsulated pins

Shroud tubes

Main Variables

Fuel burnup, three increments to 10,900 MWd/MTM (1.1 At.%)

Fuel to cladding diametral gap (0.0035" to 0.0096" Phase I & II) (0.0035", 0.0055" and 0.0075" Phase III)

Secondary Variables

Fill gas, pins with 18.% Xe Tag

Fuel fabricated structure, pins with low pressure preslugged fuel

HEDL P-19 fuel batch

Mixed fuel-to-cladding gaps in the same pin

One high burnup PNL-2 pin (304 SS cladding 0.250" OD x 0.016" wall)

TABLE III

SUMMARY OF FABRICATED PARAMETERS FOR EACH P-20 PIN

Pin Ident.	Phase [1] I + II	Phase [1] +III	Nominal Diametral Fuel-To-Clad Gap, mils	Plenum Fill Gas [2]	Fuel Batch [3]	Average Fuel Pellet Density, % TD	Fuel Column Length, Inches
P-20-1	X		7.6	He	FE116.1	90.7	13.44
P-20-2R	X	X	7.6	He	FE116.1	91.0	13.57
P-20-3	X	X	7.6	He	FE116.1	90.9	13.44
P-20-4	X	X	7.6	He	FE116.1	90.6	13.46
P-20-5		X	7.6	He	FE116.1	90.8	13.47
P-20-7		X	7.6	He	FE116.1	91.1	13.44
P-20-8		X	7.6	He	FE116.1	90.6	13.50
P-20-9	X		7.4	Xe+He	FE116.1	91.2	13.42
P-20-10	X	X	7.6	Xe+He	FE116.1	91.2	13.56
P-20-11	X	X	7.5	Xe+He	FE116.1	91.1	13.43
P-20-12		X	7.5	Xe+He	FE116.1	91.3	13,76
P-20-13		X	7.4	Xe+He	FE116.1	91.1	13.58
P-20-15		X	7.7	He	FE117.2	91.4	13.40
P-20-18	X		M 5.5 [4]	He	FE116.1	91.4	13.61
P-20-19	X	X	M 5.4	He	FE116.1	91.3	13.61
P-20-20	X	X	M 5.6	He	FE116.1	91.3	13.59
P-20-21		X	M 5.5	He	FE116.1	91.2	13.48
P-20-22		X	M 5.6	He	FE116.1	91.4	13.43
P-20-24	X		5.6	He	FE116.1	90.8	13.45
P-20-25R	X	X	5.6	He	FE116.1	91.2	13.59
P-20-26	X	X	5.5	He	FE116.1	91.1	13.43
P-20-27	X	X	5.6	He	FE116.1	91.0	13.48
P-20-28		X	5.5	He	FE116.1	91.2	13.48
P-20-29		X	5.6	He	FE116.1	91.3	13.45
P-20-30		X	5.5	He	FE116.1	91.0	13.55
P-20-32	X		3.6	He	FE116.1	90.6	13.42
P-20-33	X	X	3.6	He	FE116.1	90.6	13.52
P-20-34R	X	X	3.5	He	FE116.1	91.1	13.60
P-20-35	X	X	3.5	He	FE116.1	90.7	13.45
P-20-36		X	3.6	He	FE116.1	90.6	13.48
P-20-37		X	3.5	He	FE116.1	90.6	13.50
P-20-39		X	7.6	He	FE117.2	91.5	13.59
P-20/19-1R		X	9.6	He	FE100.1	90.8	13.40
P-20/19-14		X	3.8	He	FE100.1	90.8	13.62
P-20/19-21		X	7.6	He	FE100.1	90.8	13.49
P-20/19-23	X		3.8	He	FE100.1	90.8	13.40
P-20/19-34		X	7.2	He	FE100.1	90.8	13.58
P-20/PNL-2-5		X	6	He	MEE-13	91.7	13.59

[1] Phase I, Subassembly #X169A; Phase II, Subassembly #X169; Phase III, Subassembly #X169B.

[2] He 100% Helium, Xe + He -18.3% Xe +81.7 Helium.

[3] FE100.1 P-19 Fuel, High Pressure preslugged; FE 116.1 P-20 Fuel, High Pressure Preslugged; FE117.2 P-20 Fuel, Low Pressure Preslugged; MEE-13 PNL-2 Fuel, Low Pressure Press.

[4] M 5.5 - Mixed gap pin; Mixed gap sizes over four inches length near axial midplane with 5.5 mil gap fuel in remainder of fuel column.

certain Xe and Kr isotopes for a given subassembly to allow identifying "leakers" in the event of a cladding breach.) In addition, pins were included with fuel columns made up of different diameter pellets (mixed gap) to evaluate axial "smoothing" of Q'_m, and with fuel fabricated by low pressure preslugging[68], see Section D.6, to determine the impact on Q'_m of varying the type of porosity. Other pins in the test were unirradiated spares from the HEDL P-19 test to provide the internal calibration of the HEDL P-20 test to the P-19 test. Also a pin from the PNL-2[59] subassembly was included to help assess Q'_m at high burnup.

Detailed fabrication descriptions on those pins whose data are used in the analysis described in this report are given in Appendix C Reference 4. These pins were essentially the same design as the 0.230 inch OD pins used in the P-19 experiment. However, different fuel fabrication lots were used. The mixed gap P-20 pins and the PNL 2-5 pin are not discussed in the following analyses because analyses on these are still preliminary.

The P-20 test was conducted in three phases. The purpose of Phases I and II was to accumulate fuel burnup under steady-state conditions, see Figure 4. The peak fuel pin linear power in these phases was about 13.75 kW/ft or approximately 78 percent of the peak linear power during Phase III. This power was intended to be about 87 percent of the peak power during Phase III similar to the one hour hold level in the P-19 test. However, the peak power obtained in Phase III, Figure 4, was slightly higher than predicted. Since complete fuel restructuring occurred this will not significantly affect the Q'_m results. After Phases I

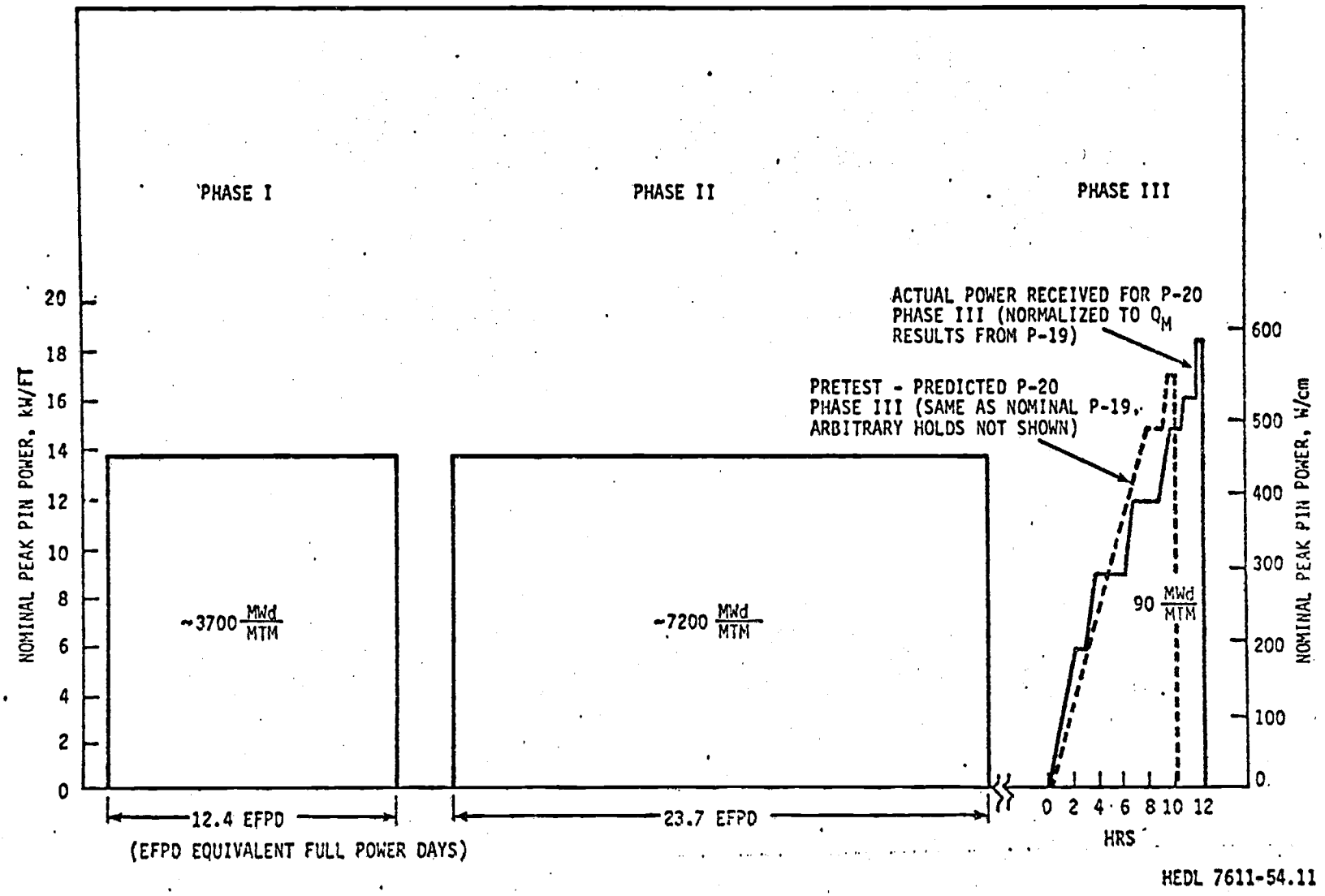

Figure 4. Peak Power History for a Nominal HEDL P-20 Pin

and II some pins were removed and unirradiated pins added so that three different burnup levels were achieved, (see Table IV). Phase III was then conducted using several pins from each of the three burnup levels, plus six "fresh" pins and one PNL-2 fuel pin (burnup of 65,000 MWd/MTM).

The Phase III portion of the test was scheduled to be conducted with the same power-time history as in the P-19 test, Figure 3. Actual power history for the test is shown in Figure 5. Several of the hold times were longer than in the P-19 test because of reactor operating requirements. However, these were judged to be of no consequence to the test results because they occurred at fairly low powers. The core loading for EBR-II for this phase was adjusted to obtain at least the same pin power levels as the P-19 test. A special core loading[70] was necessary since the reactor radial reflector had been changed from depleted uranium to stainless steel, causing lower flux levels in the center of the reactor at the same reactor power level. As will be shown later, burnups and Q'_m data indicate that the powers in the P-20 test were actually higher than the P-19 test.

After Phase III irradiation was completed, the pins were neutron radiographed and shipped as rapidly as possible to Los Alamos Scientific Laboratory (LASL) for nondestructive examination. Destructive examination followed at both HEDL and LASL. Table V summarizes neutron and betatron radiograph data. Later ceramography confirmed these observations.

TABLE IV

SUMMARY OF P-20 IRRADIATION CONDITIONS

	EBR-II		Equivalent Full Power Days	Approximate Accumulated Burnup MWd/MTM	Reactor Full Power Cycles
	Run No.	Test Position			
Phase I	61A	3F2	12.4	3700	2.
Phase II	59B	3F2	23.7	7200	6.
Phase I + II	---	---	36.1	10,900	8.
Phase III	62E	1N1	0.26	90	1.

TABLE V

FUEL MELTING RESULTS FOR THE PHASE III HEDL P-20 TEST PINS

Pre-irradiated Burnup, MWd/MTM	Total Pins	Pure He Pin Fill Gas					18% Xe-82% He Pin Fill Gas	Comments
		3.5*	5.5*	7.5*	Mixed	Other	7.5*	
0	7	--	1	2**	1	2***	1	All pins had fuel melting
3700	5	1	1	1	1	--	1	Only the 3.5 mil gap pin had fuel melting
7200	3	1	1	1	--	--	--	No fuel melting
10900	3	1	1	1	--	--	--	No fuel melting
65000	1	--	--	--	--	1	--	PNL-2-5 (0.250 in. O.D., 6 mil gap) had fuel melting

*As built, nominal fuel-to-cladding diametral gap size, mils

**One pin contained low pressure preslugged fuel

***P-19 spare pins, 7.2 and 7.6 mil gaps

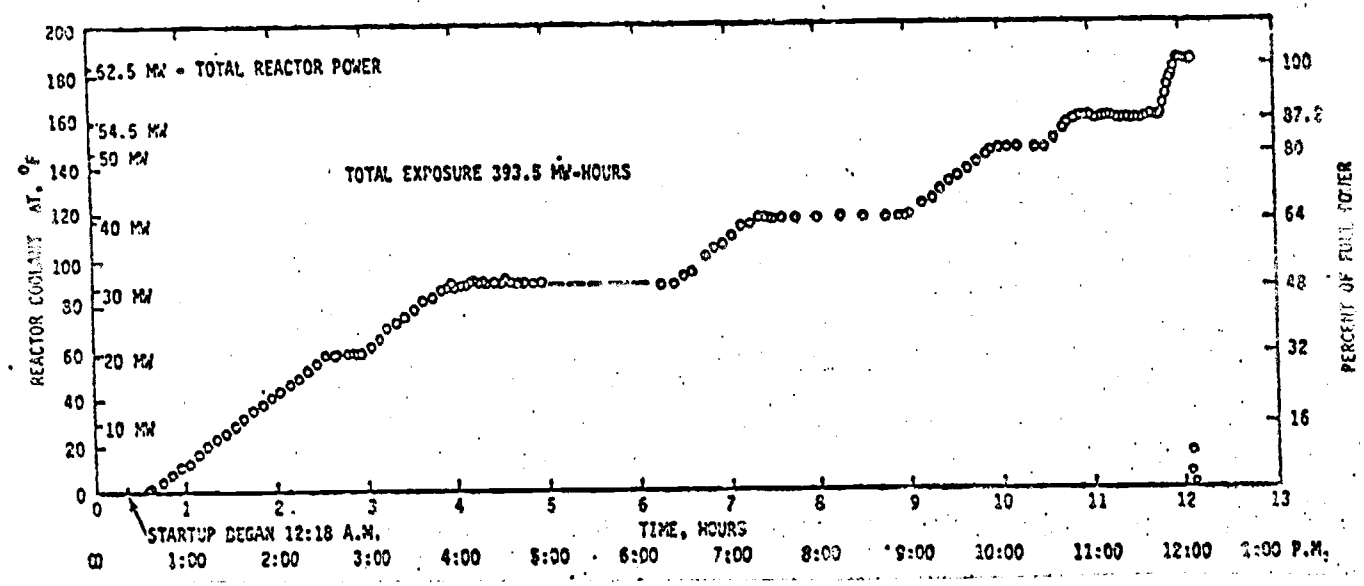

Figure 5. Power-Time History for HEDL P-20 Phase III.

Using neutron radiography, betatron radiography, ceramography and autoradiography, the axial extents of fuel melting were determined by the same methods used in the analysis of the P-19 test.

B.2 Ceramographic Data From HEDL P-19 and P-20

The longitudinal ceramography sections, used to identify the axial extents of melting, were located based on the appearance of the central voids observed on the neutron radiographs and betatron radiographs, see Appendix A. Longitudinal ceramography sections were then cut from the pins at those locations. The sections were mounted in plastic and ground to the longitudinal centerline of the pin. Reimpregnation minimized fuel "fall out" and "pull out". Photomacrographs, α and β-γ autoradiographs and 75x photomosaics in the polished and etched condition were prepared for each section.

From this ceramography the axial extents of melting were accurately located. Figure 6 and 7 show examples from P-20 of the data used to find the axial extents of melting, Reference 4 includes examples of additional pins. Appendix A describes the fuel characteristics used to locate the axial extent of fuel melting. The positions of the axial extents of fuel melting (which correspond to the location for incipient fuel melting) were found on the neutron radiographs, and measurements from the bottom of the fuel column to this location were made. These positions are summarized in Table VI and VII.

An estimate of the central void and columnar grain radii are needed near the axial extents of melting but in fuel where no melting occurred for normalizing the Q'_m data. If a transverse ceramography section

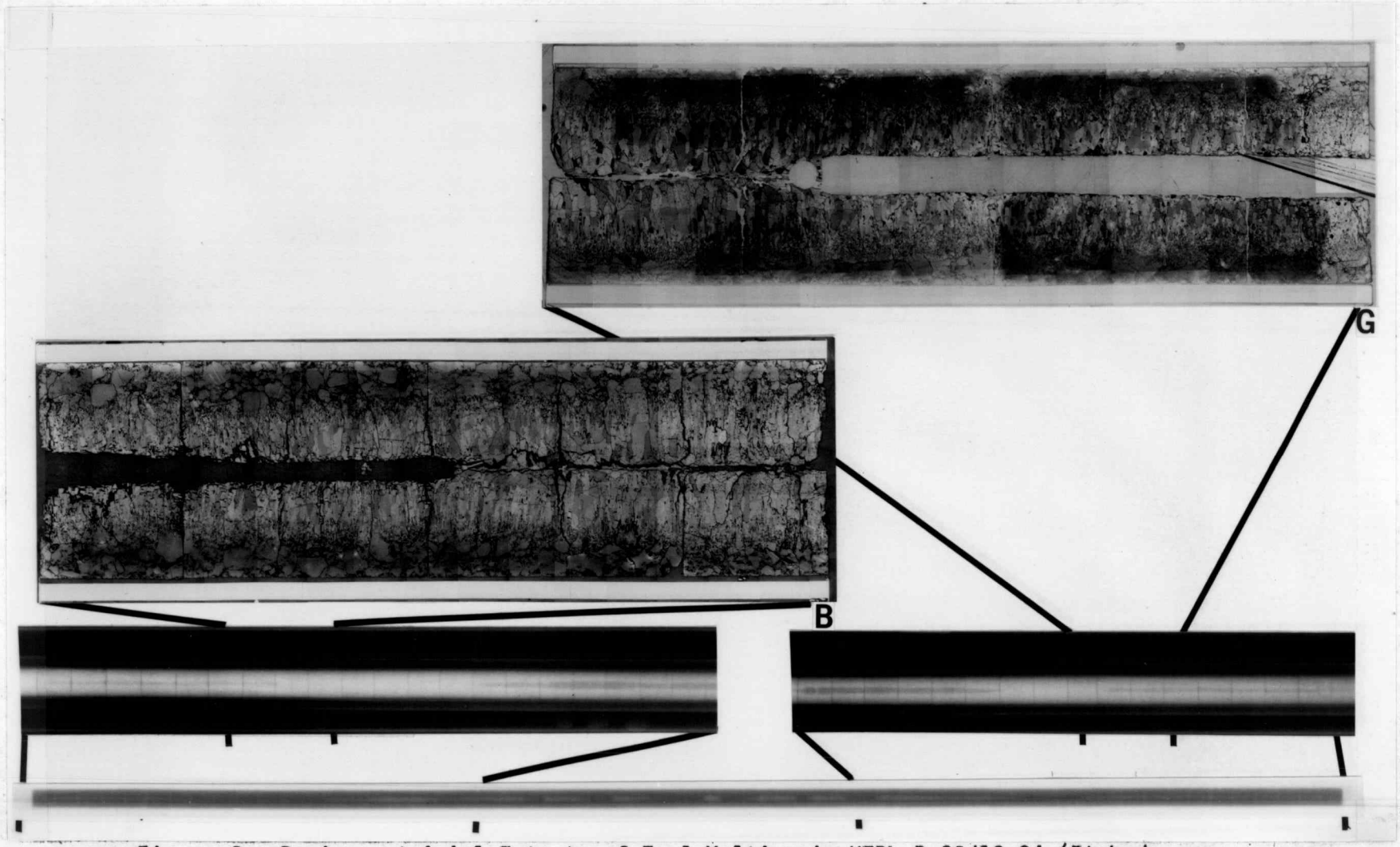

Figure 6. Regions at Axial Extents of Fuel Melting in HEDL P-20/19-34 (Etched Longitudinal Ceramography, Betatron Radiography, Neutron Radiography with Arrows Locating Positions of Axial Extents of Melting.)

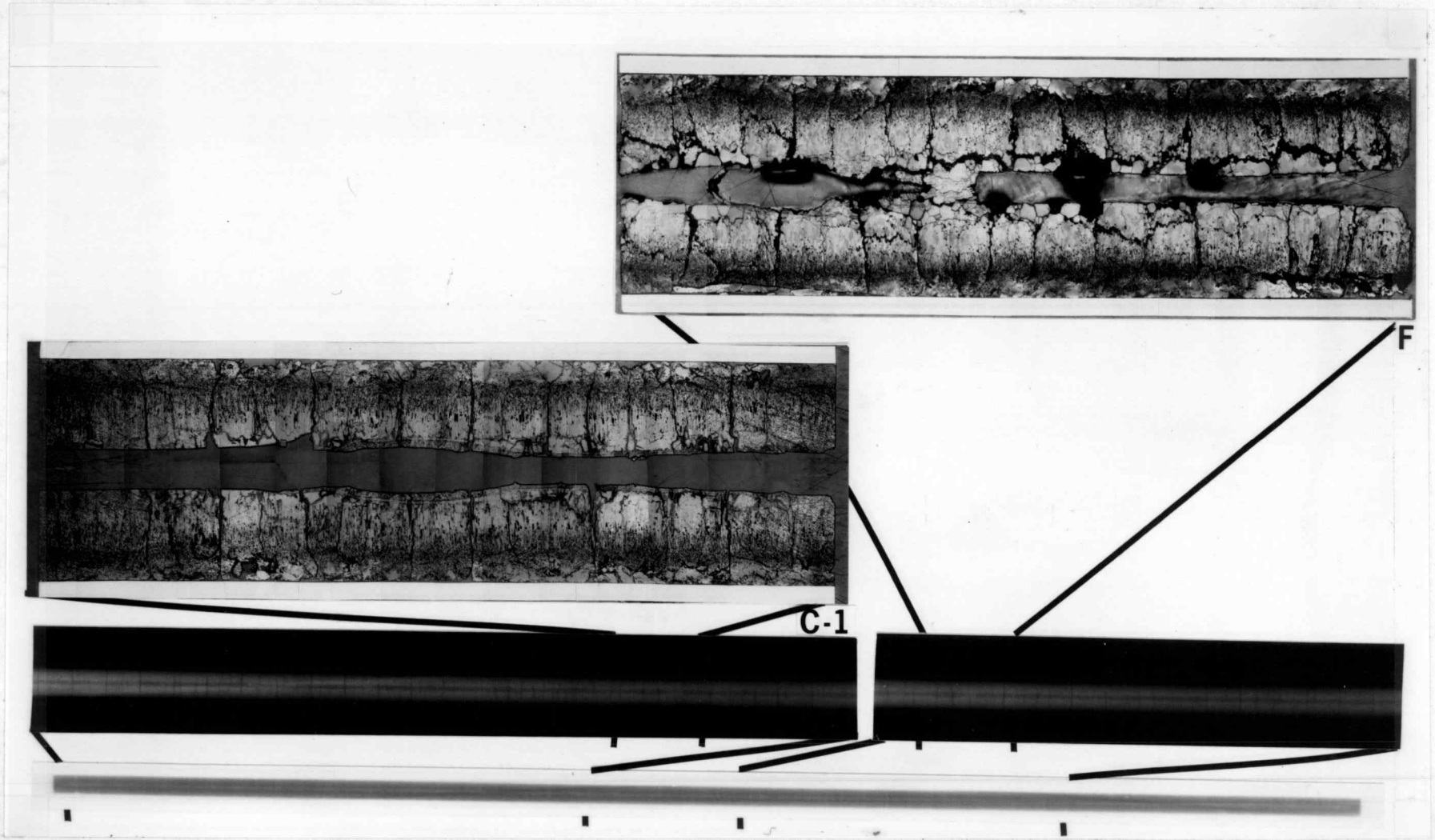

Figure 7. Regions at Axial Extents of Fuel Melting in P-20-33 (Etched Longitudinal Ceramography, Betatron Radiography, and Neutron Radiography with Arrows Locating Positions of Axial Extents of Melting.)

TABLE VI

PEAK PIN POWERS AND AXIAL EXTENTS OF MELTING FOR HEDL P-19 PINS

Pin Identity	Peak Pin Power kW/ft	Bottom Axial Extent of Melting			Top Axial Extent of Melting		
		Location[1]	Local Power[2] kW/ft	Coolant Temp Deg. F	Location[1]	Local Power[2] kW/ft	Coolant Temp. Deg. F.
P-19-2	16.6	2.84	15.8	726.	9.78	15.4	799.
3R	19.5	0.35	16.0	704.	12.32	15.7	843.
5	17.1	---	---	---	---	---	---
6	17.1	---	---	---	---	---	---
7R	20.3	1.61	18.0	718.	11.27	17.3	838.
8	16.4	2.49	15.5	723.	10.48	14.8	805.
13	16.6	3.33	16.1	732.	9.41	15.7	796.
20	16.5	3.87	16.0	737.	10.64	14.8	807.
24R	19.7	0.59	16.1	705.	12.60	15.1	848.
25R	20.1	0.83	16.8	709.	12.01	16.1	846.
26R	20.4	1.84	18.4	720.	10.68	18.2	833.
27R	20.4	2.33	18.8	727.	10.18	18.5	828.
28	20.7	2.35	18.9	727.	10.70	18.0	835.
30	20.0	1.11	17.2	712.	11.35	17.1	838.
33	16.8	---	---	---	---	---	---
35	16.5	3.26	16.0	731.	8.84	16.0	790.

(1) Distance from bottom of fuel column in inches.

(2) Powers corrected for once molten fuel plugs if present in ceramography.

TABLE VII

PEAK PIN POWERS AND AXIAL EXTENTS OF MELTING FOR PHASE III HEDL P-20 PINS

Pin Identity	Preconditioning Phase	Peak Phase III Pin Power kW/ft[1]	Bottom Axial Extent of Melting			Top Axial Extent of Melting		
			Location[2]	Local Power[4] kW/ft	Coolant Temp Deg. F	Location[2]	Local Power[4] kW/ft	Coolant Temp Deg. F
P-20-2R	I	18.1	---	---	---	---	---	---
4	I & II	17.9	---	---	---	---	---	---
7	NONE	18.0	0.70	15.4	713.	11.50	15.1	934.
8	II	17.7	---	---	---	---	---	---
10	I	17.9	---	---	---	---	---	---
13	NONE	18.0	0.10[3]	14.9	703.	13.30[3]	13.9	966.
25R	I	18.3	---	---	---	---	---	---
27	I & II	18.1	---	---	---	---	---	---
29	II	18.2	---	---	---	---	---	---
30	NONE	18.4	1.35	16.5	725.	10.92	15.9	929.
33	I	18.6	4.98	18.4	802.	7.51	18.6	859.
35	I & II	18.4	---	---	---	---	---	---
37	II	18.5	---	---	---	---	---	---
39	NONE	18.0	1.73	16.5	731.	10.06	16.3	907.
P-20/19-21	NONE	17.9	1.22	15.9	724.	11.58	15.2	937.
P-20/19-34	NONE	18.0	1.60	16.0	731.	10.87	16.2	923.

(1) Powers normalized to P-19 powers as described in Appendix B.

(2) Distance from bottom of fuel column in inches.

(3) "Axial extents of melting" for this Xenon tagged pin extended into the two dimensional heat transfer region at each end of the fuel column. Thus the fuel can be considered to have melted through the top and bottom of the fuel column.

(4) Powers corrected for once molten fuel plug if present in ceramography.

(which allows the most accurate measurement of radial regions) was not available, the longitudinal sections used for measurement of axial extents of melting, or sibling pin data were used. Table VIII summarizes these estimates. When measurements from the longitudinal sections are used, as was the case most of the time, a slightly underestimated normalized Q'_m may result because the restructured zones are typically underestimated due to 1) the regions forming at the thermal center and not necessarily at the geometric center to which they were ground, and 2) there being some uncertainty that these long (up to 1 inch) sections are uniformly ground to the exact center of pin.

Because of the short comings of using the data on radial extents of melting from the transverse ceramography sections taken near the axial midplane of the fuel columns, these data are not considered directly. The problems with using these include:

1) not knowing the amount of fuel present at the section location when the maximum extent of melting occurred (because of molten fuel relocation).

2) not being able to assess accurately the behavior of the fuel restructuring because of the amount of radial melting that occurred.

These data, however, should make a good check of trends and magnitude of the Q'_m data. Measurements of central channel sizes, melt radii, columnar grain region radii and fuel-to-cladding gap taken from transverse ceramography from the P-19 and P-20 pins is described in Tables IX and X.

TABLE VIII

ESTIMATES OF RESTRUCTURING AT AXIAL EXTENTS OF MELTING

Pin Identity	Top Axial Extent of Melting			Bottom Axial Extent of Melting		
	Radius Central Void, Inches	Radius Columnar Grain, Inches	Calculated[2] Columnar Grain Region Density, %TD	Radius Central Void, Inches	Radius Columnar Grain Inches	Calculated[2] Columnar Grain Region Density, %TD
P-19-2	.014	.061	96.4	.015	.060	98.0
3R	.016	.073	96.9	.016	.073	97.2
7R	.015	.068	97.4	.015	.061	98.6
8	.017	.063	98.0	.016	.062	98.0
13	.014	.061	98.0	.015	.060	98.0
20	.017	.062	97.3	.016	.062	97.4
24R	.008	.067	93.1	.008	.067	92.9
25R	.018	.071	98.5	.009	.068	93.6
26R	.017	.066	98.2	.015	.060	98.6
27R	.014	.057	98.4	.012	.060	96.1
28	.008	.058	94.5	.009	.057	94.5
30	.015	.065	97.9	.013	.065	96.0
35	.016	.064	96.6	.015	.067	96.0
P-20-7	.015	.065	96.9	.015[1]	.064	96.9
13	.015	.071	98.0	.015	.070	98.0
30	.018	.065	98.5	.018[1]	.060	98.5
33	.012	.072	93.5	.019	.074	96.5
39	.016	.068	97.1	.015[1]	.064	98.2
P-20/19-21	.012	.065	93.9	.015	.068	96.0
P-20/19-34	.017	.065	96.1	.014	.061	97.8

(1) The central void at the bottom section was obliterated by molten fuel relocation. In this case the central void size from the top of the pin was used, see Appendix A.

(2) Based on densification of columnar grain needed to form central void. Densities were limited to no higher than 98.5% TD based on observations of grain region.

TABLE IX

MEASUREMENTS FROM TRANSVERSE CERAMOGRAPHY FROM HEDL P-19

Pin Identity		Location[1], Inches	Fabricated Diametral Fuel-to-Clad Gap, Mils	Pellet Density % TD	Measured Postirradiation Values: Central Void Radius, Inches	Molten Region Radius, Inches	Columnar Grain Region Radius, Inches	Diametral Fuel-to-Clad Gap, Mils
P-19-2	B	6.1	7.9	90.4	.025	.037	.071	6.6
	D	7.5	7.7	90.9	.023	.031	.068	5.6
P-19-5	B	6.1	5.7	90.7	.018	0.0	.066	4.0
	D	7.3	5.8	91.6	.019	0.0	.065	5.9
	F	8.0	5.7	91.2	.017	0.0	.061	4.0
	G	8.5	5.8	91.1	.018	0.0	.063	4.8
P-19-6	B	6.1	3.8	90.7	.014	0.0	.062	2.8
	C	7.0	3.5	90.9	.014	0.0	.059	2.7
	D	7.4	3.9	91.4	.015	0.0	.060	3.6
	E	7.9	4.0	90.7	.015	0.0	.062	2.9
	F	8.4	3.9	91.0	.015	0.0	.055	2.8
	G	8.9	3.7	90.3	.013	0.0	.055	3.3
P-19-8	B	6.1	9.8	90.6	.018	.038	.073	8.2
P-19-24R	B	6.1	10.0	92.1	.007	.045	.083	4.2
P-19-25R	B	6.1	8.0	92.4	.039	.048	.083	4.9
	D	7.3	8.0	92.5	.031	.035	.080	4.1
P-19-26R	B	6.1	6.1	92.6	.025	.028	.075	4.0
	D	7.4	6.1	92.1	.027	.047	.079	3.7
	E	7.8	6.1	92.9	.030	.036	.076	4.1
	F	8.2	6.1	92.8	.005	.030	.073	3.6
P-19-27R	B	6.1	4.1	92.2	.013	.040	.073	2.7
	D	7.3	4.0	92.8	.029	.033	.074	3.3
	E	8.0	4.1	92.0	.020	.027	.073	2.8
	F	8.2	4.1	92.7	0.0	.036	.073	2.5
	G	8.6	4.0	92.6	.022	.029	.070	3.7
P-19-28	B	6.1	3.3	92.2	0.0	.034	.071	3.4
	D	7.3	3.4	92.0	0.0	.038	.073	2.6
	E	8.0	3.3	92.7	.027	.036	.073	2.5
	F	8.2	3.6	93.0	.022	.028	.071	2.8
	G	8.6	3.4	92.6	.009	.034	.073	2.0
P-19-30	B	6.1	7.1	92.5	.039	.052	.079	3.0
	C	6.9	7.2	92.3	.037	.049	.081	3.0
	D	7.6	7.1	92.5	.007	.051	.082	2.9
P-19-33	C	6.1	5.1	90.8	.017	0.0	.064	3.4
	D	6.9	5.0	91.2	.017	0.0	.063	5.0
	E	7.6	5.0	90.8	.016	0.0	.065	5.4
	F	8.2	5.0	90.6	.017	0.0	.063	4.5
	G	8.7	5.0	90.7	.014	0.0	.059	4.4
P-19-35	B	6.1	7.3	90.8	.023	.030	.069	4.9
	D	7.6	7.2	89.9	0.0	.031	.069	6.5
	E	8.2	7.1	90.7	.008	.032	.069	5.9

[1] Inches from bottom of fuel column

TABLE X

MEASUREMENTS FROM TRANSVERSE CERAMOGRAPHY FROM HEDL P-20 PHASE III

Pin Identity		Location[1], Inches	Fabricated Diametral Fuel-to-Clad Gap, Mils	Pellet Density % TD	Measured Post Irradiation Values			
					Central Void Radius, Inches	Molten Region Radius, Inches	Columnar Grain Region Radius, Inches	Diametral Fuel-to-Clad Gap, Mils
P-20-7	D	6.5	7.6	90.9	.010	.047	.080	5.4
-13	E	6.4	7.6	91.6	0.0	.053	.083	6.9
-30	E	6.6	7.3	91.1	0.0	.034	.073	4.4
-39	D	6.6	7.7	91.3	.020	.041	.076	4.7
P-20/P-19-21	D	6.2	7.6	90.9	.017	.041	.073	5.0
P-20/P-19-34	E	6.7	5.6	91.2	.024	.041	.077	2.1
P-20-2R	D	1.5	7.5	91.1	.026	0.0	.078	1.8
	G	6.2	7.5	91.3	.027	0.0	.081	1.3
	L	11.9	7.7	91.5	.023	0.0	.075	1.6
P-20-4	D	1.5	7.6	91.0	.025	0.0	.074	1.1
	G	6.2	7.6	91.2	.029	0.0	.080	.7
	L	11.9	7.6	90.4	.028	0.0	.079	.9
P-20-8	D	1.5	7.7	91.5	.026	0.0	.078	1.3
	G	6.2	7.7	90.5	.029	0.0	.083	1.7
	L	12.0	7.6	90.6	.027	0.0	.079	1.1
P-20-10	D	1.5	7.7	91.5	.025	0.0	.084	1.8
	G	6.2	7.6	91.4	.027	0.0		1.4
	L	12.0	7.7	91.0	.027	0.0	.081	2.2
P-20-25R	D	1.5	5.6	91.3	.022	0.0	.075	2.4
	G	6.2	5.6	91.1	.023	0.0	.079	1.9
	L	12.0	5.6	91.1	.022	0.0	.077	2.1
P-20-27	D	1.5	5.7	90.9	.022	0.0	.072	1.5
	G	6.2	5.6	91.0	.026	0.0	.078	1.9
	L	12.0	5.8	91.1	.026	0.0	.075	2.4
P-20-29	D	1.5	5.7	91.3	.023	0.0	.074	1.7
	G	6.2	5.6	91.4	.026	0.0	.078	1.3
	L	12.0	5.6	91.2	.023	0.0	.076	1.8
P-20-33	B	1.5	3.5	91.2	.018	0.0	.068	2.2
	D	6.0	3.5	90.1	.020	0.0	.078	2.1
	H	11.9	3.8	90.4	.019	0.0	.073	2.7
P-20-35	D	1.5	3.6	90.1	.016	0.0	.070	2.3
	G	6.2	3.5	90.5	.020	0.0	.077	3.2
	L	12.0	3.5	90.8	.020	0.0	.073	1.5
P-20-37	D	1.6	3.4	90.2	.017	0.0	.069	1.7
	G	6.2	3.4	90.7	.019	0.0	.074	1.1
	L	12.0	3.5	90.5	.021	0.0	.073	1.0

[1] Inches from bottom of fuel column

B.3 Operating Conditions

The fuel operating conditions pertaining to the temperatures obtained in the fuel pins at the locations of axial melting must be characterized as well as possible. The uncertainty in operating conditions reflects directly in uncertainty in the derived Q'_m.

B.3.a Pin Power

Peak pin powers in the HEDL P-19 experiment are based on a detailed study[67] made by Argonne National Laboratory, ANL. Previous preliminary studies with P-19 used these powers reduced by a factor of 0.94 as suggested in the conclusions of this study due to possible bias in the thermal balance made on the EBR-II coolant system. For the present analysis the factor of 0.91 was chosen to use because of more recent detailed analyses[71] made of the problem; these included data for the specific reactor run the experiment was in.

As described in Appendix B, the HEDL P-20 peak pin powers were derived based on the analysis of the results of the spare P-19 pins used in P-20 and compared to the behavior of similar pins in P-19. Thus the change in power, an increase of 9 percent, needed to cause the observed melting in sibling pins in the P-20 was found and this factor applied to all the P-20 pins. Pin to pin variation were based on relative fission rates calculated by ANL.

Appendix B reviews the method used to find the axial power distributions for the HEDL P-19 pins and the HEDL P-20 pins in Phase III. From the axial power profiles and the peak power of each pin the local

power at each axial extent of melting was found, Tables VI and VII. The values were corrected upward slightly, based on the increased volume of fuel, if a once molten fuel plug was present in the central void at the location of the axial extent of melting.

The power at the upper extent of melting in the P-20-33 pin, the only preirradiated pin with fuel melting, was not adjusted for the fuel plug observed. The power at the axial extents of melting, with no plug correction, are one percent less than peak pin power; the axial power/temperature gradiant is very flat in this region. Adjusting the power upward for the fuel plug would raise this local power here above the peak power of the pin, but the peak power location must have had incipient melting prior to this location (if the power needed to cause melting was greater than the peak power no melting would have occurred in this pin). The assumption not to correct for the plug is conservative and is consistant with the lower axial extent of melting. It is believed this plug may have been deposited by some axial transport mechanism other than that observed in the fresh fuel. The central void above this upper extent is narrower than that of the sibling pin examined after Phase I exposure but shows no signs of melting. This perhaps indicates some fuel vapor transport mechanism is acting in this region where temperatures are almost at the melting point over a substantial distance.

Figures 8 and 9 show the data from HEDL P-19 and P-20 axial extents of melting. The P-20 values for the Xenon tagged pin are not for the axial extents of melting since this pin melted end-to-end. Thus Q'_m for this pin must be less than the powers at the ends of the fuel column and points corresponding to these form an "upper bound" of Q'_m. Only one

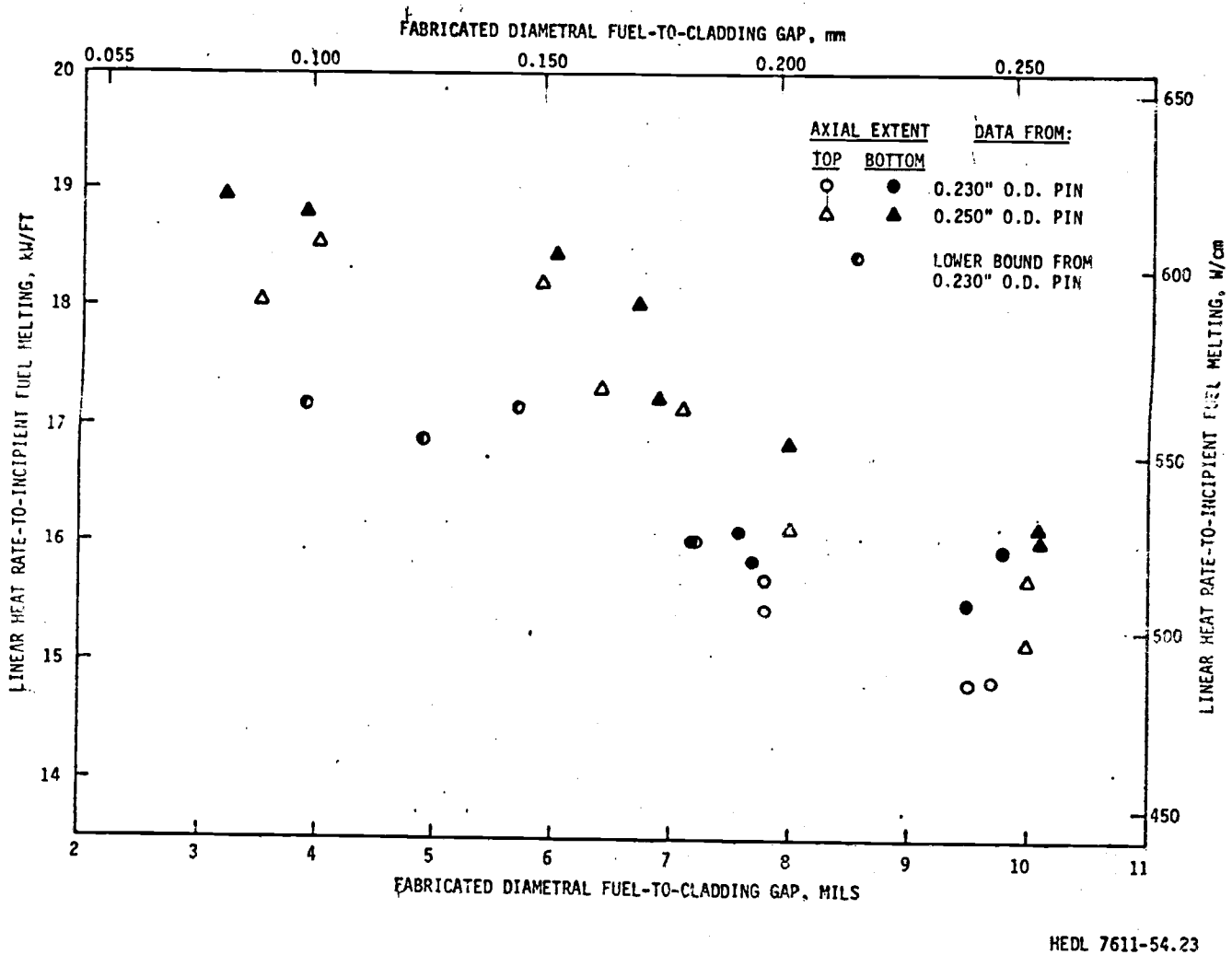

Figure 8. Q'_m Data Derived from Axial Extents of Melting in HEDL P-19 Pins

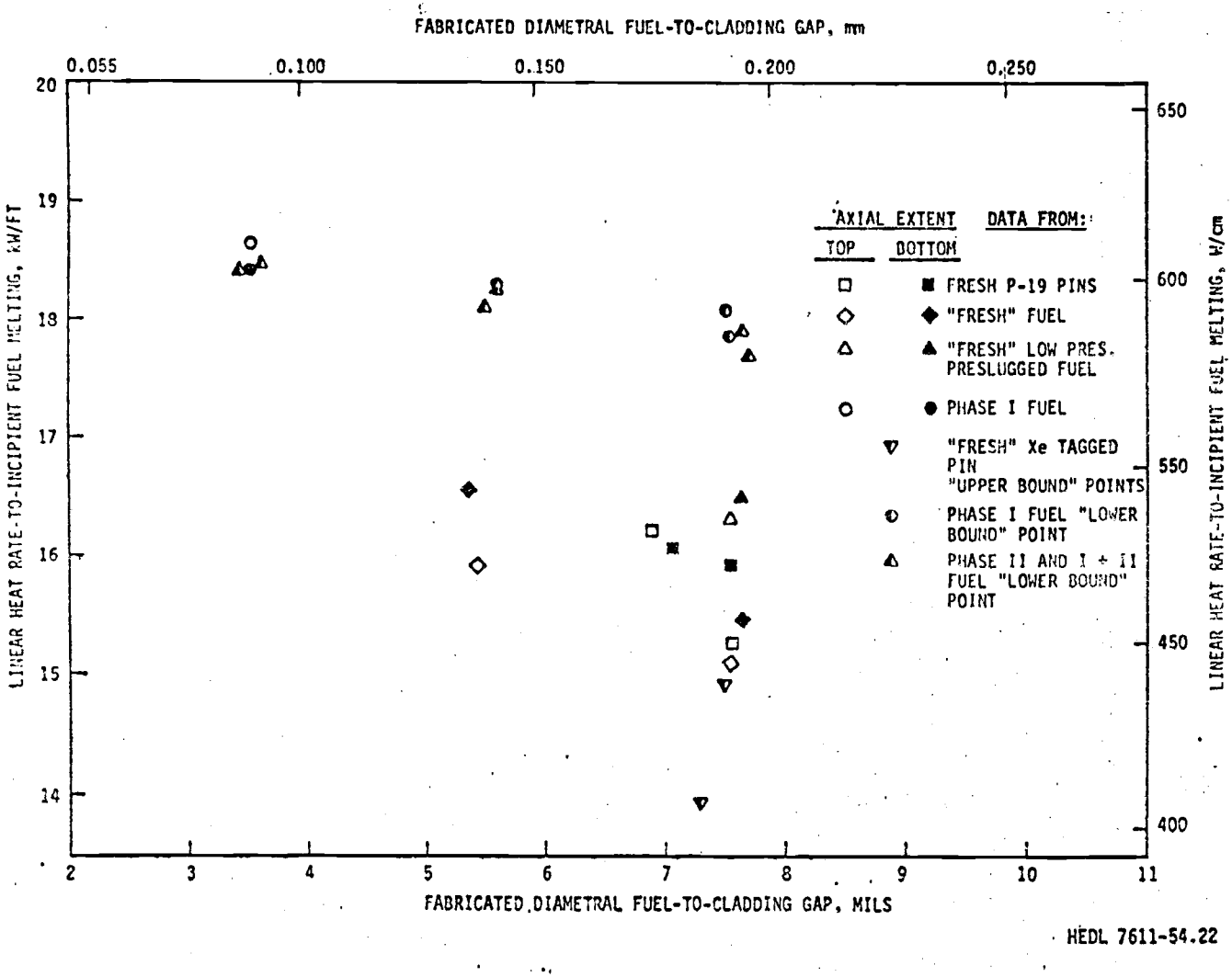

Figure 9. Q'_m Data Derived from Axial Extents of Melting in HEDL P-20 Pins

P-20 pin with burnup prior to Phase III melted. Also shown on Figure 9 are the maximum powers reached by fuel pins that experienced no melting. Transverse ceramography performed at the peak power region of these pins showed no signs of fuel melting. Thus these peak power values establish a "lower bound" of Q'_m for these pins (i.e., Q'_m is greater than these peak power values). Similarly, "lower bound" points are shown in Figure 8 for the P-19 fuel pins that did not melt.

B.3.b Coolant Temperatures

The flow rate of coolant in the P-19 subassembly was based on ANL calculations. These in turn were based on a pretest flow test made on the assembly, reactor conditions and the thermal hydraulics code EBRFLOW. The calculated flow rate of the sodium coolant (after correction for the 0.91 factor) was calculated to be 1340 pounds of sodium per hour at 800°F. Tests of the type of assembly used for P-19 and P-20, with shroud tubes, have shown that there is an equal split of coolant to each pin. Thus no mixing or bias need be accounted for.

The flow rate in the P-20 assembly was calculated based on pretest flow measurements on the assembly and on the measured reactor core coolant pressure drop during irradiation. This calculation yielded a flow rate of 768 pounds of sodium per hour at 800°F.

Tables VI and VII show the calculated coolant temperature at each axial extent of melting location based on the previously described pin power, coolant flow rate and axial power profile. Section C.1 discusses the calculation of coolant ΔT.

B.4 Normalization of Q'_m Data

The normalization of Q'_m data to a single set of parameters (based on FFTF):

- Cladding ID temperature, 1060°F (570°C)
- Plenum temperature, 1060°F
- Pellet density, 90.4% TD
- Cladding and fuel geometry, 0.230 inch OD cladding,

is necessary for direct use of the data in design reactor applications. To accomplish the normalization a modified version of SIEX-M1, see Section F, was used. Consideration of those mechanisms of the heat transfer models which could be left constant and those that should be adjusted had to be made. For the majority of the data, the normalization was minimal since the tests were designed to be as near the selected FFTF conditions as possible. The normalization of the data from the 0.250 inch OD fuel pins to the smaller, 0.230 inch OD size represents the greatest adjustment needed.

Figure 10 indicates the normalization method used. Basic steps followed were:

1) the fuel-to-cladding gap conductance, H, was adjusted in the SIEX-M1 code thermal simulation at the location of the melting exent with all other variables (i.e. local power, central void size, pellet density, local cladding temperature, measured restructuring, etc.) held constant, using measured and fabrication data, until incipient melting was calculated. The constant B discussed in Section C.4.b was used to adjust the gap conductance.

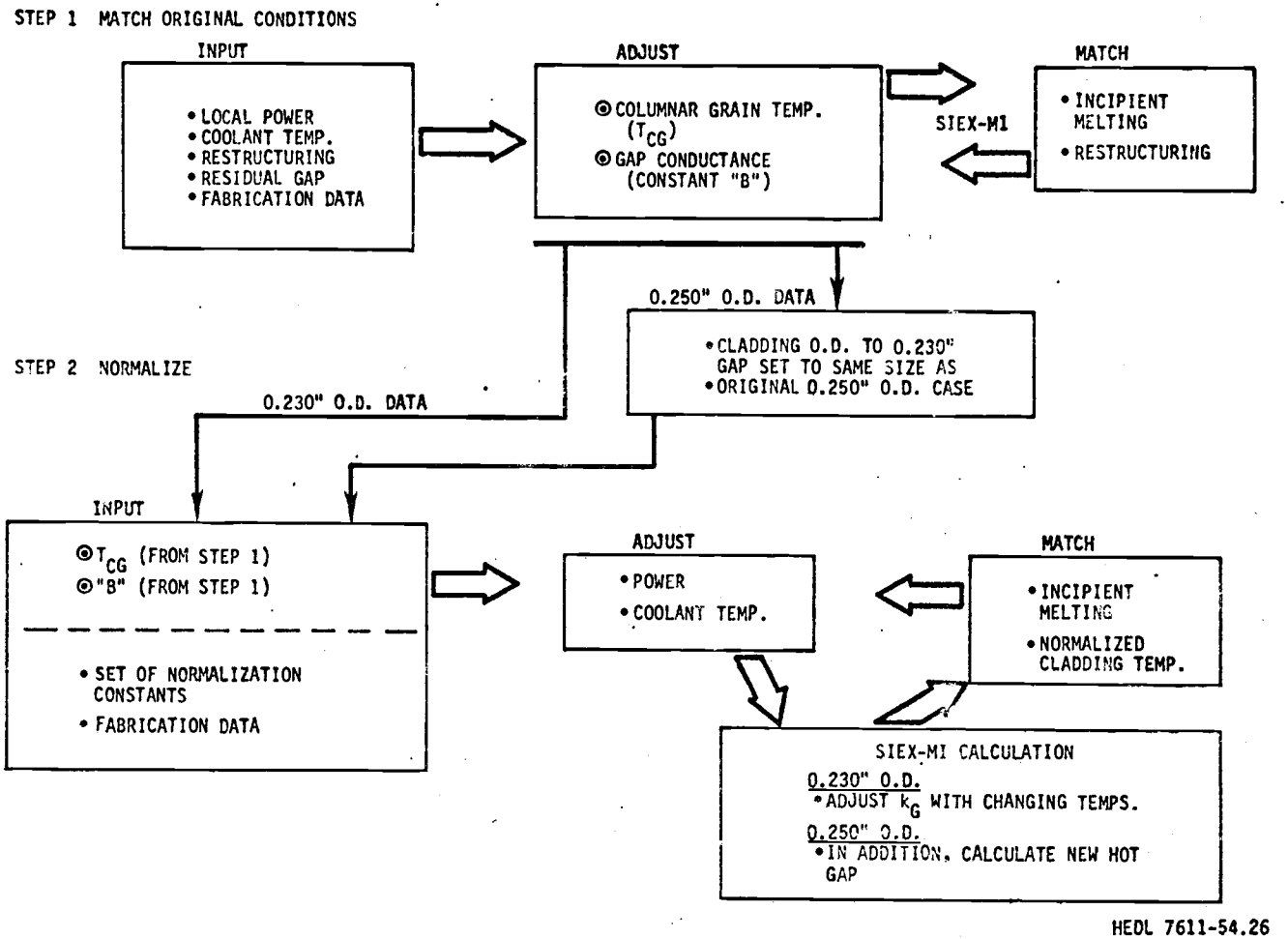

Figure 10. Normalization of Q'_m Values.

2) new values were entered for pellet density, cladding ID temperature, and plenum temperature. Also for the 0.250 inch fuel pins the fuel and cladding sizes were adjusted.

3) the local linear power was then adjusted until incipient melting (Q'_m normalized) was again calculated.

For the 0.230 inch OD fuel pin data the only adjustment made by the code to the gap conductance was for the effect of temperature on the local gas thermal conductivity and the gas pressure in the fuel-to-cladding gap. For the data from 0.250 inch OD pins that were in P-19, SIEX-M1 was used to recalculate a new hot gap, when normalizing to the 0.230 inch sizes, as well as adjusting for temperature changes effecting gap conductance. In addition, for all normalizations a constant amount of Ar and N_2 gas absorbed during fuel fabrication was assumed released.

The constant B, from Equation 18, was assumed the adjustable parameter in the heat transfer system in step 1) above, since it is the constant used for both open and closed hot gap calculations. Once this value was set by matching the data in each case no further adjustment was made to it. Thus any effects due to differences in the fuel and cladding surfaces between the different fabrication batches and lots is ignored, no data was taken to characterize them. This should be a very small effect because of the consistancy of fabrication methods.

Figures 11 and 12 show the normalized data for the two experiments.

B.5 Discussion of Behavior of Q'_m

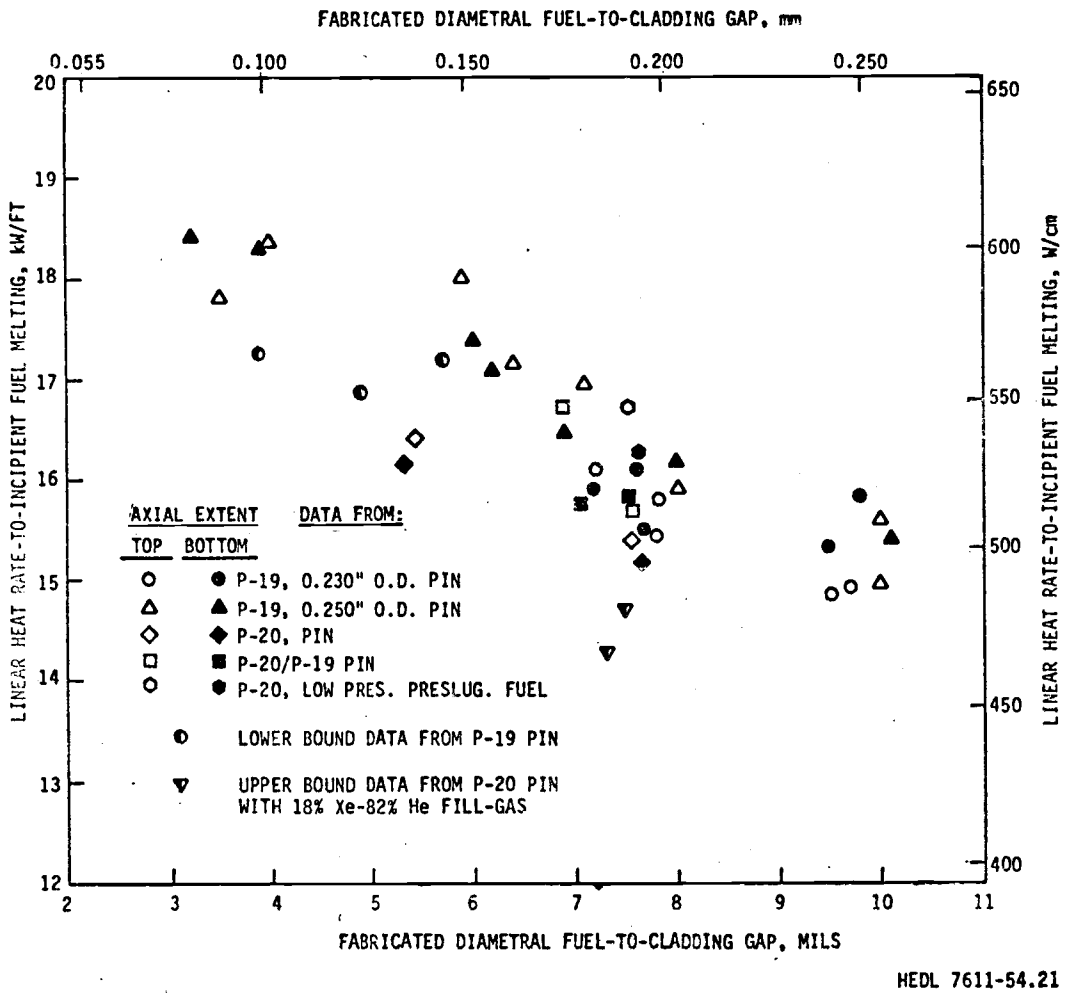

Figure 11. Normalized Q'_m Values for "Fresh" Fuel.

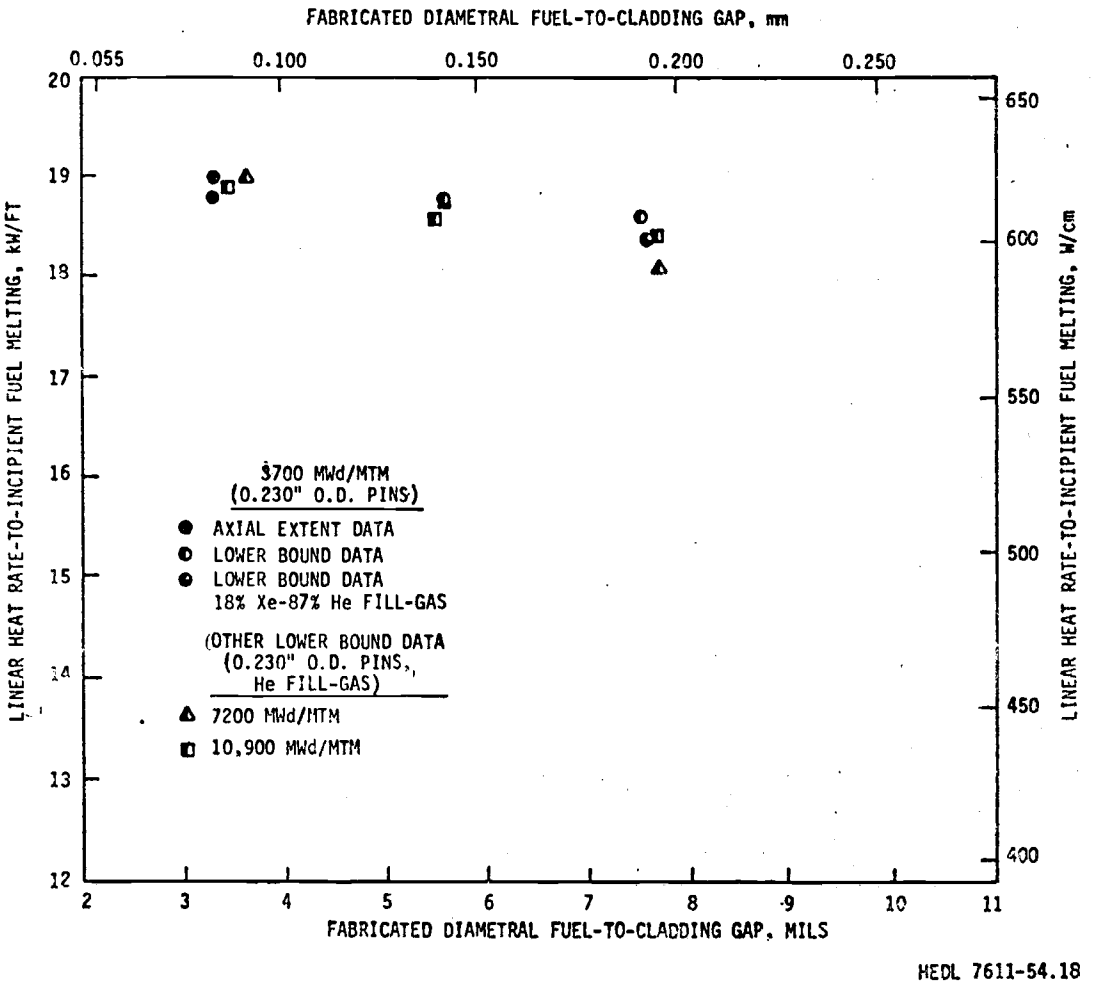

Figure 12. Normalized Q'_m Values for Fuel with Significant Burnup.

B.5.a Normalized Q'_m Values in "Fresh" Fuel

Figure 11 summarizes the normalized data for the "fresh" (60 to 90 MWd/MTM) pins from the HEDL P-19 and P-20 experiments. The agreement between the two sets of data is good except for the 0.0055 inch fuel-to-cladding diametral gap pin from the P-20 test. The trend observed is for Q'_m, to increase with decreasing fabricated fuel-to-cladding gap size up to a certain gap size (about 0.0045 inch) and then to level off to a constant value. This is interpreted, as will be noted in the calibration of SIEX-M1 later, as the heat being transferred at first only through the gas in the gap, then the fuel and cladding surfaces contacting and resulting in a transition region, and finally a constant transfer system established consisting of both solid-to-solid contact and conductivity through the gas. The final constant value at small gap sizes is the result of the fuel yielding, thus no further increase in interface pressure, before enough stress is built-up to plastically strain the cladding. This assumption is based on measured profilometry of the cladding OD's where no plastic yielding of the cladding was found in any of the test pins.

The reason for the lower result from the P-20 pin with the 0.0055 inch fuel-to-cladding diametral gap is not clear. It may be significant that this gap size is right where the fuel and cladding are expected come in contact during operation, thus making it the most sensitive to differences in surface roughness and "waviness" of the fuel and cladding. It is also noted that the rest of the Q'_m data at this gap size and smaller are from normalized data from the 0.250 inch OD pins. However

the "lower bound" points taken from the P-19 unmolten 0.230 inch OD pins at this gap size substantiate the 0.250 inch OD normalized points. Detailed reviews of the methods used to normalize the 0.250 inch OD data were made before selecting the method finally incorporated into the version of SIEX-M1 used in this study. The percent difference of these P-20 points from the P-19 data points could also be explained by them being considered extremes in the uncertainty in calculating the powers at the locations of melting.

Note that the low pressure preslugged fuel appears to have a slightly higher Q'_m than the high pressure preslugged fuel. This is consistant with the Phase I and II results in Appendix C. However, differences noted in the nonhelium sorbed gas content between the two batches, see Appendix C, may be causing differences in fuel conductivity or in the gas conductivity in the fuel-to-cladding gap.

B.5.b Normalized Q'_m in Fuel with up to 10,900 MWd/MTM Burnup

Figure 12 shows the normalized results from the pins with the three levels of higher burnup from the HEDL P-20 test. The improvement in normalized Q'_m for the 18% Xenon tagged pin is more than 25% in going from the upper bound of the "fresh" pin Q'_m, Figure 11, to the lower bound of the Phase I pin irradiated to 3700 MWd/MTM.

Only one P-20 preirradiated pin experienced fuel melting, the 0.0035 inch diametral gap pin from Phase I. The axial extents of melting, as noted previously, were located at positions which operated at power levels within one percent of the peak power of the pin. Thus, the peak power region was very close to incipient melting. From the data in

Figure 12, including the lower bound for Q'_m calculated from the peak power sections of the unmelted preirradiated pins, we conclude that the effect of initial fabricated fuel-to-cladding gap size on the power-to-melt is no longer a dominant variable after a small amount of irradiation. The apparent reason for this occurrence is described in Section B.5.c.

Application of these results to FFTF/LMFBR fuel performance prediction shows the data's significant implications. Viable fuel pin fabrication processes require diametral gap larger than 0.005 inch, and to date it has been necessary to allow for the reduction in Q'_m, in the thermal design of fast reactor fuel pins, as well as to employ centerless grinding of the fuel pellets to control pellet OD's to tight tolerances. The test results now indicate that after a short conditioning period (less than 3700 MWd/MTM), not only can thermal rating of the LMFBR be increased by at least 20%, but restrictive limits on maximum fabricated gap size can be relaxed.

B.5.c Proposed Fuel Behavior With Burnup Based on P-20 Phase I and II Results

A sibling of each preirradiated pin in Phase III was nondestructively and destructively examined. In addition to these sibling pins several other pins with different gap sizes and burnup levels of interest were also examined typically the pins were:

- Neutron and betatron radiographed
- Precision gamma scanned

- Punctured for recovery of fission gas
- Sectioned for burnup analysis and ceramography

A review of the ceramography and fission gas release data results obtained are described in Appendix C. The following discusses Phase I and II results as they pertain to Q'_m.

The conclusions from Phases I and II that pertain to Q'_m are as follows:

1) "Cold" fuel-to-cladding diametral gap rapidly closes to about 0.001 to 0.0025 inch early in life, at a burnup of less than 3700 MWd/MTM. After that, the gap continues to close at a slower rate.

2) The columnar grain region apparently forms early before the fuel-to-cladding gaps close to the 0.001 to 0.0025 inch (0.03 to 0.064 mm) range found at the end of Phase I. It thus reflects a marked dependence on the fabricated gap size. Additional columnar restructuring does not occur beyond Phase I burnup. Measurements from sections of the preirradiated pins included in Phase III indicate, even with the overpower received, that increases in columnar grain region size do not occur. It is likely that the temperatures at the terminus of columnar grains never exceed the BOL temperatures due to the pronounced gap closure.

3) Measurements of the equiaxed grain growth region, show little original fuel-to-cladding gap dependence, indicating that this region is principally formed after the majority of gap closure has occurred. Thus the data imply peak fuel temperatures occurring early in life, followed by decreasing fuel temperatures because of rapid fuel-to-

cladding gap closure with proportionally more closure for larger gaps. By 3700 MWd/MTM burnup, the gap sizes are closing more slowly with time, and they appear to have reached a fairly uniform 0.0010 to 0.0025 inch (0.025 to 0.063 mm) diametral gap.

This interpretation explains the significant improvement in power-to-melt, beyond that normally expected from additional fuel restructuring, with just the Phase I preirradiation over the "fresh" fuel. This would also explain the lack of, or reversal of fabricated gap dependence of Q'_m after a small amount of burnup, 3700 MWd/MTM.

It would indicate why the fuel pin having a 0.0035 inch diametral gap and irradiated in Phase I later melted in Phase III while larger gap pins with the same preirradiation burnup did not. This pin had the smallest initial gap and highest fuel smeared density[1] of the group of Phase I pins in Phase III. It had the least columnar grain formation (note sibling data Appendix C) and central void formation. Therefore, this fuel pin ran at higher fuel temperatures than the other pins once the fuel-to-cladding gaps were closed to about the same size. As clarification, consider the following sequence. During Phase I, all the fuel-to-cladding gaps closed to about the same size and (for the same pin power) the temperature drops across the gaps became about the same. The temperature drop across the fuel, then controlling the relative fuel centerline temperatures, was greater for the pin with the least restructuring. This follows from the increased thermal conductivity of the

[1] Fuel smeared density: Weight of fuel divided by the corresponding volume within cladding ID, (Fuel weight over length L)/$(\frac{[\text{Clad ID}]^2}{2} \times \pi \times L)$.

higher density columnar grain region and, in particular, from the larger central voids (i.e., shorter radial heat flow paths) in the fuel pins with more restructuring.

The higher temperatures in the P-20 preirradiated fuel pins with smaller initial gaps is further enhanced by:

1) Slightly higher specific power of the pin because of higher fuel smeared density[2].

2) Movement of fuel-to-cladding gap voidage to the central void. This mechanism, described in Reference 26 and Section C.5.b, would have the effect of increasing central void size more for large gap pins, thus further dropping the centerline temperature of the fuel with the larger gap.

It is believed that these hypotheses account to some extent for the small gap pin irradiated in Phase I to have experienced fuel melting during Phase III while the larger gap pins, including the one tagged with 18% Xenon, did not. However, the primary reason appears to be that fuel restructuring occurs prior to the rapid fuel-to-cladding gap closure, which brings all the gap sizes to about the same values.

---

[2]P-20 fuel pellets were all about the same density so a decrease in fuel-to-cladding gap size in the same size cladding tube results in a higher fuel pin smeared density and more fuel per location.

At higher burnups, 7200 MWd/MTM (Phase II) and 10,900 MWd/MTM (Phases I and II), the 0.0035 inch diametral gap pins did not melt, nor did any pins of the other gap sizes. This is believed due to further small improvements in thermal performance most likely caused by additional fuel-to-cladding gap closure, and improved heat transfer between the contacting fuel and cladding surfaces (caused by creep of the contacting surface roughness asperities or buildup of solid fission products in the voids between the contacting roughness asperities).

B.6 Q'_m Results from Radial Extents of Melting

Figure 13 shows the normalized Q'_m values derived from radial extents of melting measured near the fuel column midplanes of "fresh" pins, Tables IX and X. The radial extent data were normalized in a fashion similar to that used for the axial extents. Since there is no way to directly calculate the columnar grain density at the location of the radial melting extents (the central void observed is actually a molten fuel shrinkage cavity), the average of values found near the axial extents of melting were used. None of the powers used to derive Q'_m values were corrected for molten fuel plugs that were most likely present during part of the irradiation.

In general, the trends and magnitudes for Q'_m calculated from the radial data are in good agreement (see Figure 11) with those derived from axial extent data. Note the higher Q'_m result, compared to the results from the axial extent analysis, for the P-20 pin with a 0.0055

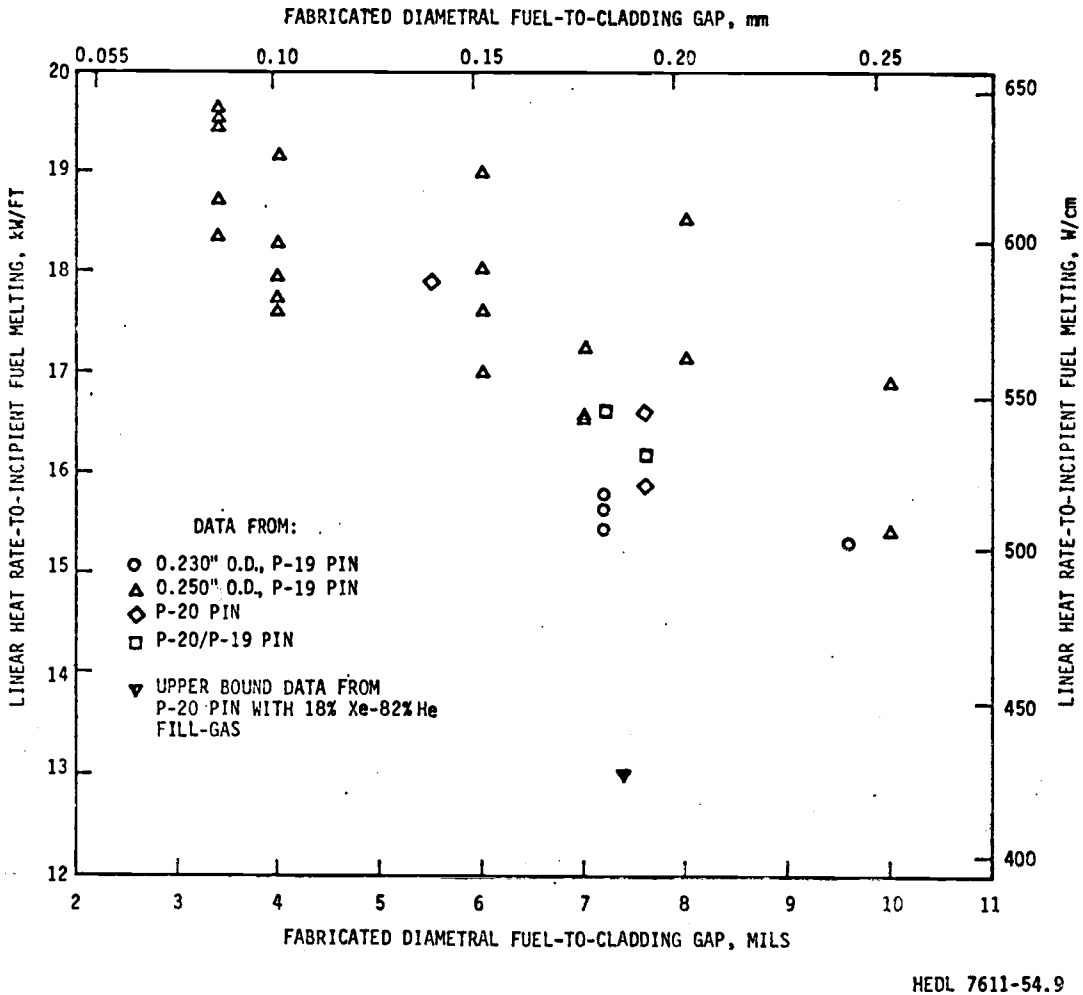

Figure 13. Normalized Q'_m Values Calculated from Radial Extents of Melting in "Fresh" Pins.

inch gap. Other assumptions for fuel restructuring and local power, due to changes caused by molten fuel plugs, can change the results from these sections significantly. Thus no further analysis was made using these data.

No plot of Q'_m values from radial extents from higher burnup pins is made since it follows that they would be the same as Figure 12; only one pin actually melted and this was in effect at incipient melting.

B.7 Expected Uncertainty in Q'_m Derived from Axial Extent Data

A good estimate of the uncertainty involved in the derivation of Q'_m from the axial extents of melting can be made from the uncertainty in calculating the local power at these points. The uncertainty in the location of the melt extent and coolant temperature at these positions is minor compared to the power uncertainty.

As noted in Reference 67 the uncertainty in calculating pin powers in P-19, to which all data was normalized, was about 10%. However a 6% uncertainty, which was noted to be directional, included in this estimate was for determining the actual EBR-II reactor power level. More recent analyses[71] of this "uncertainty" have shown it to be a real bias in the system and powers in this report were corrected downward for it, see Section B.3.a.

It is estimated, combining the uncertainty in the calculation of absolute peak pin power with the uncertainty in locating and calculating local powers at the axial extents of melting, that the absolute uncertainty in the Q'_m values derived is on the order of ± 6%. In addition to this uncertainty there is an uncertainty in measured fabricated dia-

metral gap size on the order of ± 0.0003 inch (± 0.008 mm). A detailed error analysis for the Q'_m results will follow in the future as part of additional design application.

C Radial Heat Transfer Path in Fuel

Because of the long length of the fuel columns in question (13.5 inches or 34.3 cm) compared to the radii (about .1 inches or .25 cm) and the fact that the axial power/temperature profiles have no abrupt discontinuities, it is assumed that all heat is transferred from the fuel pins in the radial direction. The exception to this, which will not be considered in this study, is at the ends of the fuel column. Here there is axial heat transfer also, but the effects of this are only seen back into the fuel column about a distance of two fuel radii. All axial extents of melting considered in this study are at least twice this distance from the ends of the fuel column, unless specifically noted.

The extrapolation of the effect of fuel-to-cladding gap size on Q'_m beyond the actual test conditions, and the calibration of a fuel thermal performance code are very dependent on the heat transfer models and assumptions used. The following summarizes the models used in this study for the radial heat transfer path from the sodium coolant to the fuel center.

C.1 Sodium Coolant Temperatures at an Axial Position

The temperature of the sodium coolant, T_I, at any axial location, x_i, along the pin is based on the reactor inlet temperature, T_{In}, (which is 700°F or 371°C for the test pins) and the integration of the heat deposited in the coolant flow channel from the pin up to the point of interest.

$$(1) \qquad T_I = T_{In} + \frac{\int_0^{x_i} Q'\,dy}{M_F \cdot C_p}$$

where M_F = Mass flow rate

C_p = Specific heat of sodium

Q' = Linear heat rate or linear power

Each P-19 and P-20 fuel pin had an individual flow tube, thus no coolant mixing need be considered. The mass flow rate, M_F, for these pins was calculated from the measured pressure drop across the reactor core at the time of the test and results of flow tests made on each subassembly prior to irradiation. The shape of the axial power profile was derived from measured burnup values taken along several fuel columns as has already been discussed.

C.2 Sodium-to-Cladding Temperature Drop

The temperature drop due to the fluid boundary layer formed next to the tube wall in flowing sodium is relatively small and can be characterized for thermal conductance purposes by a film coefficient, H_F, from an equation similar to that noted by Bird et al[37] and credited to Martinelle[80]:

$$H_F = \frac{k_{Na}}{D_e} Nu = \frac{k_{Na}}{D_e} [7.0 + 0.025 (Re\ Pr)^{0.8}]$$

where: k_{Na} = Thermal conductivity of sodium

D_e = Coolant equivalent diameter

Nu = Nusselt number

Re = Reynolds number

Pr = Prandtle number

A typical value for an LMFBR pin is about 25,000 BTU/Ft^2-Hr°F (14. W/cm^2 - °C).

For a normal LMFBR pin this temperature drop would be the only one between the coolant and the cladding OD. However, the test pins were encapsulated using an outer stainless steel tube bonded to the fuel pin cladding with stagnant NaK, see appendices A and C of Reference 4. Thus additional thermal resistance is present. Using the thermal conductivity of the two capsule materials and the thicknesses of each, an equivalent film coefficient (H_{eq}) applied to the cladding OD was calculated to simplify analysis. This coefficient included the effects of the actual film and the capsule materials. Coefficients of 4770 Btu/ft^2 - °F - hr (2.7 W/cm^2 - °C) for the pins with 0.230 inch (0.58 cm) OD cladding and 4860 Btu/ft^2 - °F - hr (2.8 W/cm^2 - °C) for the pins with 0.250 inch (0.64 cm) OD cladding were calculated. The difference being caused by a narrower Nak region for the larger pins. Thus the temperature drop between the coolant and pin cladding wall, ΔT_{Fl}, is calculated using H_{eq} and the equation

$$\Delta T_{Fl} = \frac{Q_i'}{H_{eq} \pi r_{C,OD}} \quad . \tag{2}$$

C.3 Cladding Temperature Drop

The thermal conductivity of the 316 stainless steel wall of the cladding tube is taken from standard sources similar to those in Reference 6. A nominal value for cladding conductivity, k_C, is 11.4 Btu/ft-hr-°F (0.1972 w/cm-°C). The temperature drop, ΔT_C, across the cladding wall is then simply

$$(3) \qquad \Delta T_C = \frac{Q'_i \, (r_{C,OD} - r_C)}{k_C^{II} \, r_C}$$

where

r_C = radius of the cladding ID

C.4 Heat Transfer Across the Fuel-to-Cladding Gap

Calculation of the heat transfer across the fuel-to-cladding gap is based primarily on expressions suggested by Ross and Stout (Reference 7), past work by Dutt[5], and results of literature reviews and analyses made by the author. The modified Ross and Stout models are briefly described in the documentation[5] of the SIEX computer code. While work in this and related areas has been progressing for many years, specific applicable data for verifying conclusively theoretical models proposed for the complex heat transfer mechanisms involved is limited. This is true for out-of-reactor values but especially true for information from fast reactors (where data is almost nonexistant).

Heat transfer through the fuel-to-cladding gap is assumed separated into four parallel mechanisms. These are:

1. Conductivity through the gas gap (indicated by subscript G)
2. Conductivity through the solid-to-solid contact (subscript S)
3. Radiant heat transfer (subscript r)
4. Convective heat transfer (this is found to be negligible, as noted by other authors) (subscript Con)

In the following sections thermal conductance values for each of the mechanisms are developed and these summed together for the total "gap conductance," H.

(4) $$H = H_S + H_G + H_r + H_{Con}$$

This follows directly from the total heat rate being being equal to

(5) $$q = q_R + q_S + q_G + q_{Con}$$

and the imperical Fourier relation or Newton's "law" of cooling governing heat transfer which state

(6) $$q = kA \frac{(T_F - T_C)}{X} = HA (T_F - T_C)$$

where

q = heat flow rate

A = surface area

T_F - T_C = temperature across the material

X = thickness of the material

H = unit thermal conductance or "gap conductance"

k = thermal conductivity of the material

Since $A(T_F - T_C)$ is constant for each mechanism, substitution of Equation 6 into 5 results in 4.

C.4.a Solid-to-Solid Heat Transfer, H_S

A literature review of solid-to-solid heat transfer mechanisms was made to verify the model proposed by Ross and Stoute, which is presently used in the SIEX code. Consideration was given to models proposed by Dean (Reference 8), Rapier, et. al. (Reference 9), Cetinkale and Fishenden (Reference 10), and Mikic et. al (Reference 11). In addition,

recent survey reviews made by Jacobs and Todreas (Reference 12), and Lanning and Hann (Reference 13) comparing current models in use to results of out-of-reactor in-vacuum gap conductance results were considered. Some general observations can be made from this literature review are: 1) as noted by Lanning and Hann[13], all models for the mechanism can be reduced to the general form

$$H_S = Fk_m\left(\frac{P}{h}\right)^N \tag{7}$$

where P = apparent interface pressure

h = Myer's hardness of softer material (which is assumed directly related to yield strength of the material).

F = a function that is dependent on surface roughness and "waviness" (see Figure 14)

N = exponent (which may be pressure dependent)

k_m = harmonic mean $\left(\frac{2k_1k_2}{k_1+k_2}\right)$ of the thermal conductivity of the surfaces.

However, there is considerable difference in the dependence of the "theoretical" parameters F and N. 2) While several proposed models can be considered "theoretically" better than the Ross and Stoute model they also include the need for data which is not readily available for fast reactor fuel pins. Specific examples of these are the need for: (1) a "transition pressure" at which the softer surface changes its behavior at contacting microscopic points from elastic to plastic, and (2) the slope of the roughness asperities. Data needed for several of these

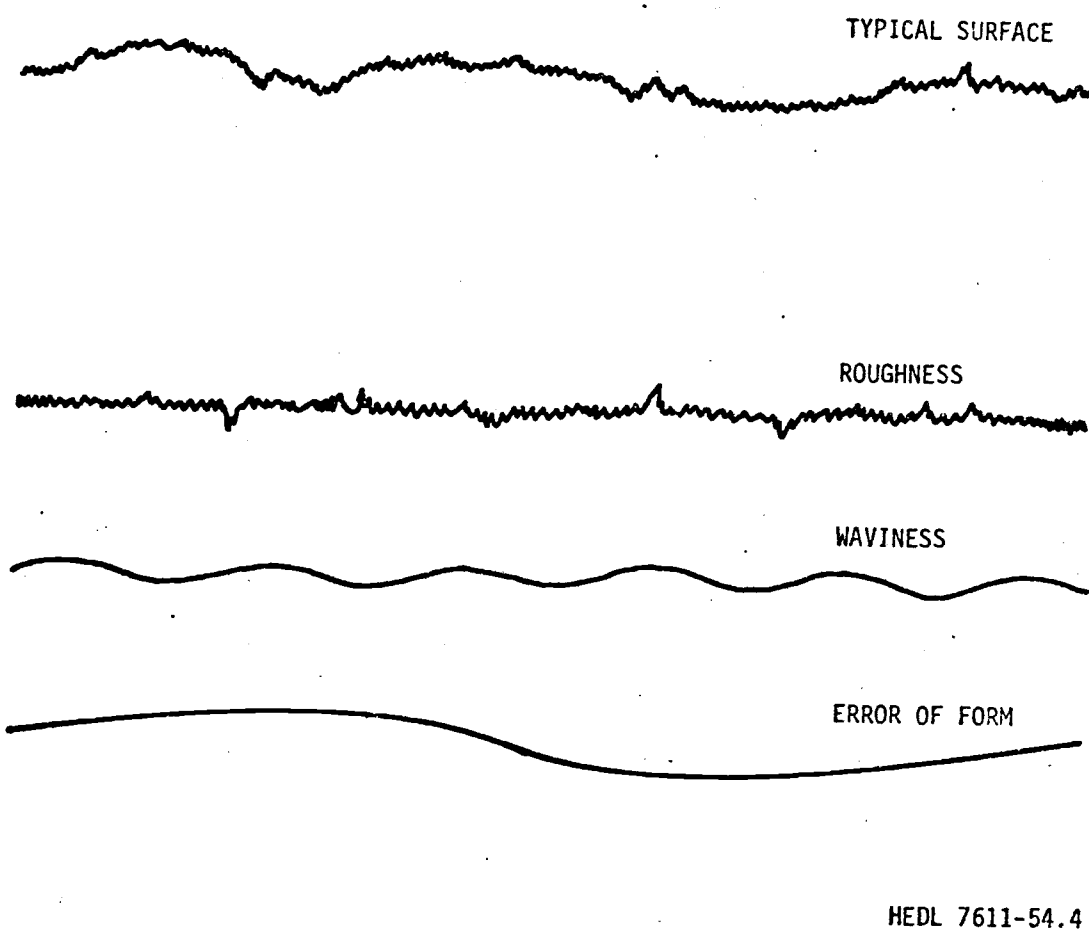

Figure 14. Surface Texture (Vertical Axis Exaggerated).

models is even lacking from what few data studies have been made, thus making confirmation, compared to out-of-reactor results, difficult.

(3) The data base to check or calibrate to is very limited. There are apparently only four significant studies which have generated data, References 7, 8, 9 and 14, sufficient for model development and these were all out of reactor. Only one in-reactor study was found; it was by Campbell and Haies[15] and confirmed in principle existing model validity, however, it was of necessity of limited scope. All of these studies were run under considerably different test conditions.

It should be noted, similar to what Jacobs and Todreas pointed out, the thermal behavior of the contact surfaces which are very dependent on the behavior of the contacting roughness asperities of "a-spots," may be significantly affected by in-reactor operation where there is power cycling, high temperatures and a neutron flux. The response of a metal-ceramic fuel interface under these conditions because of variation in pressure, solid fission product build-up, and possible creep mechanisms is not completely understood at this time. This is true even at the relatively low fuel burnup (less than 10 Mwd/KgM) conditions used in the present study.

The Ross and Stoute model for solid-to-solid heat transfer is fairly simple compared to several of the models reviewed, and the required data for its evaluation are reasonably available or can be made available. A correlated version of this model has been used for the

past three years in the SIEX thermal performance code at the Hanford Development Engineering Laboratory, HEDL, with good success in predicting thermal performance and fuel behavior for in-reactor fuel tests.[4, 81] It is the conclusion of this review that there is no advantage at this time to incorporating a different, more complex, model into the SIEX code. The model should be changed when a clearly defined advantage is demonstrated for both out-of-reactor and in-reactor predictions. The uncertainties at this time appear to overshadow the selection of another model as being "better" for application to the present study.

It should be noted that the Mikic model as proposed by Jacobs and Todreas appears to be the most promising as a future model. It does a better job of predicting the low pressure (100 psi) out-of-reactor data than the Ross and Stoute model, which underpredicts conductances. This is mainly because of the Miki-Jacobs model using a "transition pressure" at which point the exponent N is changed from 0.5 to 1. The out-of-reactor value of this transition pressure is postulated to be approaching 1000 Psi for metal-ceramic interface. For in-reactor values they note this may be too high; however there is no data available to confirm this.

The following summarizes the derivation of the model suggested by Ross and Stoute. It is included for completeness and so the assumptions made are apparent. The correlation of the constant A_2 in the final model form will be derived from experimental results analyzed previously in this report.

C.4.a.1 Model of Surface Contact

When two surfaces are brought together only a small portion of the apparent geometric area of contact is actually in contact. Microscopic roughness is present on all surfaces, Figure 14, and the contact surfaces touch only on the points of asparities (Figure 15). These points of contact are sometimes referred to as "a-spots"[16] (in a particular nomenclaure, "a" refers to the average size of a contact point or spot, πa^2, this definition of "a" is not used in this work to avoid confusion) and the thermal resistance through this area, when a lower thermal conductivity substance occupies the noncontacting areas, is often referred to as "constriction" resistance. Thus, even when the two surfaces are in contact under pressure two modes of heat transfer are acting:

1. Solid-to-solid through the a-spots
2. Conductance, convection and radiant heat transfer through the substance occupying the area between the contact spots.

The solid-to-solid model will be reviewed here, it is assumed the conductance, convection and radiant heat transfer in the non-contacting regions can be characterized by the models described in later sections.

C.4.a.2 Area of Real Contact

If two plane surfaces contact under a pressure P, and the a-spots are assumed circular and of equal size, the force balance on the surface is

(8) Force on the apparent interface = Total force on asperities

or $P \cdot A = h\alpha^2 n A \pi$

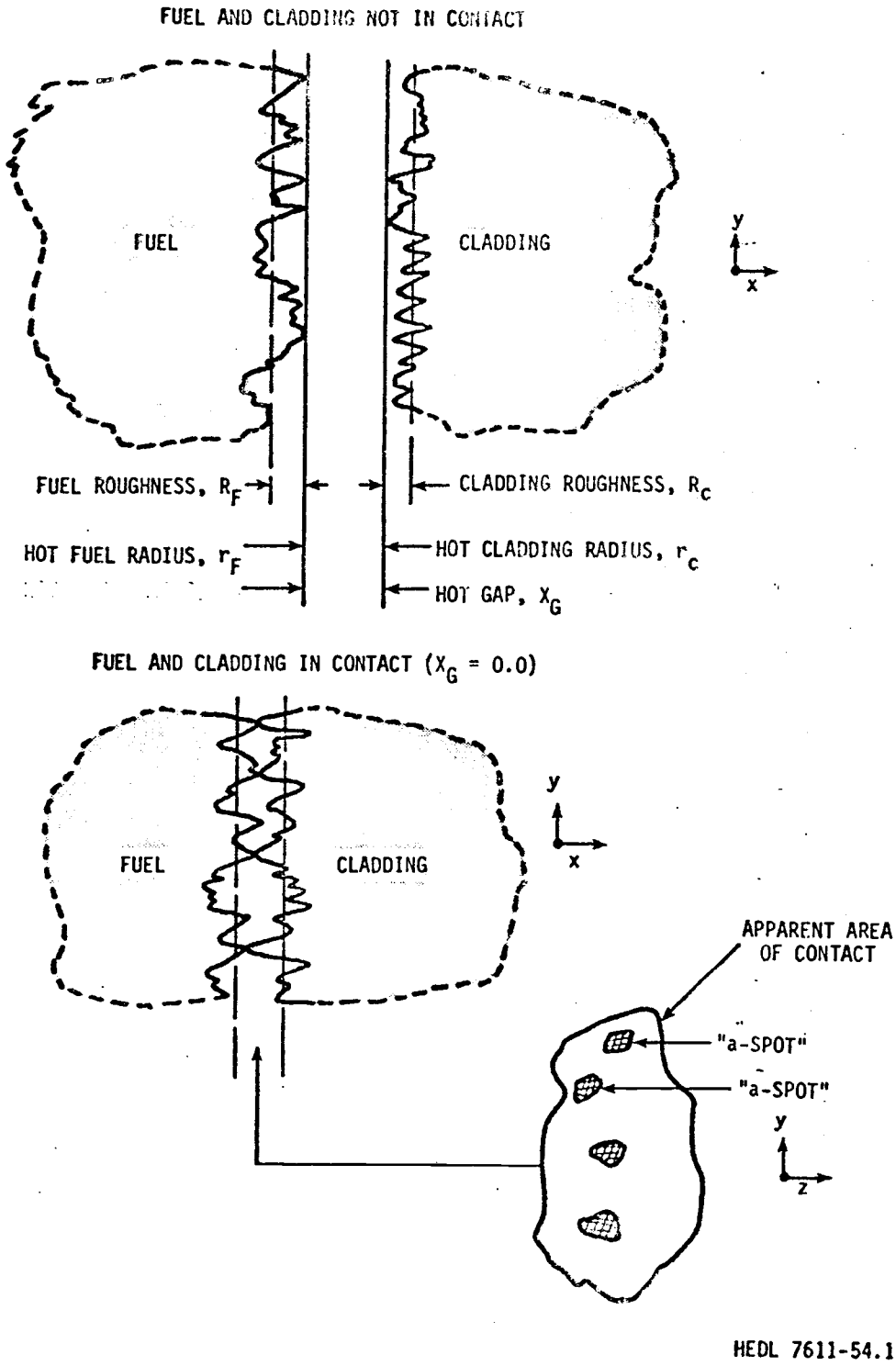

Figure 15. Surface Roughness Model Definitions.

where

α = radius of the contact spots, cm

n = number of contact spots per unit area

A = Area of apparent contact between surfaces, cm^2

h = Myer's hardness, Dynes/cm^2

P = Pressure, Dynes/cm^2 (apparent)

This follows from the fact that the radii of curvature of the contact spots are so small that they are plastically deformed by very low loads. Thus, the pressure on each spot will be equal to the Myer's[3] hardness of the softer material when all the contact spots are plastically deforming.

Holm[16] found experimentally the mean force on each contact spot only attains values equivalent to between 0.5 and 0.7 x ($h\Pi\alpha^2$). Moore[17] found in studies made with cylindrical indentors that the identity of the asperities were retained though complete plastic deformation would be expected. This is consistent with Holm's result and indicates force applied to the surfaces in contact may be transmitted by the contacting asperities to the bulk material between them. Equation 8 is then written

(9) $$P = 0.6h\Pi n\alpha^2$$

based on Holm's results. From this it is seen that actual contact area at normal pressures is very small because P is much smaller than h.

---

[3]The indentation resistance of a material expressed in force per unit area. In this case it is equal to $h = L_r/r^2$ where r is the radius of the mouth of an indentation formed by pressing an infinitely hard ball of radius r_i into the material with a load L_r. This should be proportional to the yield stress.

C.4.a.3 Constriction

Assuming only conduction through the touching contact spots of the interface the thermal resistance (R_a) to the steady state heat transfer through a circular area, radius α, into a semi-infinite material with thermal conductivity, k, was determined by Carslaw and Jaeger[18] to be $R_a = \frac{1}{4k\alpha}$.

For two semi-infinite materials in contact an an area $\pi\alpha^2$ the thermal resistances are in series and addition gives:

(10) $$R_a = \frac{1}{4k_F\alpha} + \frac{1}{4k_c\alpha}$$

So the thermal conductance through the a-spots per unit area is given approximately (since they are not actually infinite) by:

(11) $$\frac{n}{R_a} = H_s = 4\alpha n \frac{k_F k_C}{k_F + k_C}$$

Now if we let $k_m = \frac{2k_F k_C}{k_F + k_C}$ (the harmonic mean of the conductivities) the approximate thermal conductance for this apparent contact surface is thus:

(12) $$H_S = 2\alpha n k_m$$

C.4.a.4 Heat Transfer Through Solid-to-Solid Contacts

Combining Equations 9 and 12 we find the solid conductance can be written

(13) $$H_S = \left(\frac{2}{.6} \frac{\alpha P}{h\pi\alpha^2}\right) k_m = 1.06 \frac{k_m P}{\alpha h}$$

Further, Holm[10] has found when the a-spots are of unequal size the resistance should be increased by approximatly ten percent. Thus,

$$H_S \approx \frac{k_m P}{\alpha h}$$

The replacement of α by a function dependent on surface roughness is the next step. Ross and Stoute present results from several investigators which indicate that α is essentially constant at moderate to high pressures. Assuming this, measurements of Ascoli and Germagnoli[19] were used to obtain the empirical equation

$$\alpha = A_1 \bar{R}^{1/2} \text{ where } \bar{R} = \left(\frac{R_1^2 + R_2^2}{2}\right)^{1/2}$$

R_2, R_1 - Arithmetic mean of the roughness heights of respective surfaces, cm

A_1 = an empirical constant, $cm^{1/2}$

thus, the final expression for constrictive heat transfer through the a-spots is

$$H_S = \frac{k_m P}{A_1 \bar{R}^{1/2} h} \tag{14}$$

For work with SIEX the denominator of Equation 14 is further simplified. It is assumed the Myer's hardness, h, of the softer material, in this case the cladding, is linearly proportional to the yield strength, y_c, of the material as noted in the analyses made for FMODEL[23]. In addition because no direct measurement of roughness was made for the

test data used in this study constant values of roughness are assumed and $\bar{R}^{(1/2)}$ can then be considered combined with A_1 to form a constant, A_2. The resulting equation is

$$(15) \qquad H_S = \frac{k_m P}{A_1 \bar{R}^{1/2} h} = \frac{A_2 k_m P}{y_c}$$

The last assumption, of constant A_2 including $\bar{R}^{1/2}$, is the only logical choice at this time. Neither in the P-19 and P-20 tests nor present commercially produced fast reactor fuel have been characterized for surface roughness. However almost all the test fuel was fabricated similar to commercial fuel, since these were both integral tests, thus they should reflect as nearly as possible the actual commercial fuel response. The only test fuel not fabricated in this manner were fuel pellets sintered to size and used in four P-19 fuel pins (Table I), the other fuel pellets were centerless ground to size. Review of the performance of these fuel pins showed no difference between their response and the rest of the P-19 fuel pins. There remains however, a slight possibility as noted in section B.5.a that a difference in surface roughness between the P-19 and P-20 test fuels may be the reason for the lower Q'_m result when compared to P-19, of the "fresh" P-20 pin with a 0.0055 inch diametral gap. For this and reasons noted later it is recommended that in the future archive samples of the test pins be characterized for surface roughness and condition.

C.4.b Heat Transfer Through Gas, H_G

The heat transfer through either open gaps or regions between the touching asperities of the a-spots is now considered. The conductivity through a gas gap assuming perfect energy transfer at the walls and ignoring roughness would be calculated from Equation 6 as:

(16) $$H_G = \frac{k_G}{X_G}$$

k_G = thermal conductivity of the gas mixture

X_G = distance between the fuel and cladding surfaces, taken from the furthest extreme of one surface mean roughness to the other.

At the small fuel-to-cladding gap distances (less than 0.005 inch or 0.13 mm) of interest here, consideration must be made for the incomplete exchange of energy of the gas molecules at each wall. This is done, as suggested by Kennard[20], using a calculated "jump distance" which equals the temperature drop caused by this effect at a wall, divided by the temperature gradient in the main portion of the gap. This, in affect, is the distance added to X_G in order that an effective gap size produces the correct total temperature drop with gas conductivity k_G. Equation 16 then becomes[4]

---

[4] To be strictly correct, this expression for an open gap should be for two concentric cylinders which results in the equation $$H_G = \frac{k_G}{r_F\left(\ln\frac{r_c}{r_F} + \frac{g_F}{r_F} + \frac{g_c}{r_c}\right)}$$ where $r_F < r_c$ and $r_c - r_F = X_G$. However, the error introduced by using this plate form is extremely small (< .5%) because $r_c \approx r_F$ and will be ignored to simplify the expression.

$$(17) \qquad H_G = \frac{k_G}{X_G + g_F + g_C}$$

where g_F, g_C = the jump distance at each wall of the gap.

Section D.1 describes the method selected to be used in this study to calculate $g_F + g_C$ based on a detailed review made by the author of available data from the literature.

Finally, consideration of the effect of the surface roughness must be made. When in contact it is estimated that only about 10 percent of the apparent interface of contacting surfaces is involved with the a-spot contact. The remainder of the surface is involved with the lower conductivity regions occupied by the plenum gases. When in contact X_G = 0., see Figure 15, and the distance, d_{CF}, between the effective surfaces is taken equal to be:

$$(18) \qquad d_{CF} = C_1(R_F + R_C) = Be^{D \cdot P}$$

R_F, R_C = the respective roughness of the surfaces

C_1 = empirical constant

P = the interface pressure

The constants B and D are fitting parameters that will be correlated later in this report based on the experimental data. They are to some extent dependent on the waviness, Figure 14, of the surface roughness. Again roughness has been removed from the expression since it was not measured for the data being analyzed and are assumed constant.

The final expression for conductance through the gas gap is:

(19) $$H_G = \frac{k_G}{C_1(R_F + R_C) + X_G + (g_F + g_C)}$$

$$= \frac{k_G}{(Be^{D \cdot P}) + X_G + (g_F + g_C)}$$

C.4.c Thermal Conductance by Radiant Heat Transfer, H_r

The rate of heat exchanged between two surfaces by thermal radiation can be expressed as

(20) $$q_r = A_F F_{F-C}(W_{bF} - W_{bC})$$

where

A_F = Area per unit length of the fuel surface, cm^2

F_{F-C} = Exchange coefficient between the surfaces

$W_{bF} = \sigma T_F^4$, $W_{bC} = \sigma T_C^4$ } the Stefan-Boltzmann law for black bodies with radiation into a gas, W/cm^2

$\sigma = 5.67 \times 10^{-12} \frac{W}{cm^2}$ $-(°K)^4$, Stefan-Boltzmann constant

T_F, T_C = Surface temperatures of the fuel and cladding I.D., °C.

From a standard development in Chapman[21] we find our case:

$$F_{F-C} = \frac{1}{\frac{1}{\varepsilon_F} + \frac{A_F}{A_C}\left(\frac{1}{\varepsilon_C} - 1\right)}$$

where

A_C = Area per unit length of the cladding surface

ε_F, ε_C = emissivity of the fuel and cladding surfaces.

Now since the H_r at the surface of the cladding is defined by (see Equation 6):

$$H_r = \frac{q_r}{A_C(T_F - T_C)}$$

we have

(21)
$$H_r = \frac{A_F \ \sigma(T_F^4 - T_C^4)}{A_C\left(\frac{1}{\varepsilon_F} + \frac{A_F}{A_C}\left(\frac{1}{\varepsilon_C} - 1.\right)\right)(T_F - T_C)}$$

$$= \frac{r_F \ \sigma(T_F 2 - T_C 2)(T_F - T_C)}{r_C\left(\frac{1}{\varepsilon_F} + \frac{r_F}{r_C}\left(\frac{1}{\varepsilon_C} - 1\right)\right)}$$

since $A_F = 2r_F\Pi(1)$, $A_C = 2r_C\Pi(1)$

C.4.d Heat Transfer Due to Convection, H_{Con}

The effect of heat transport due to free convection in the fuel-to-cladding gap is negligible. This is because of the very small distance involved, less than 0.005 inches (0.013 cm). Dean[8] notes for air at 500°F between plates that differ in temperature by 100°F a distance of 0.4 inch (1.02 cm) is needed for incipient convection. A check of the magnitude of velocities that could be expected in the gap, based on an equation derived in Bird et al[22], also confirms this conclusion (velocities of less than 0.01 in/sec were calculated). Thus,

(22)
$$H_{Con} = 0$$

C.4.e Total Fuel-to-Cladding Gap Conductance

Based on the equations 4, 15, 19, 21 and 22 the final equation for thermal conductance across the fuel-to-cladding gap is:

$$(23)\quad H = \frac{A_2 k_m P}{y_c} + \frac{k_G}{X_G + (g_F + g_C) + Be^{P \cdot D}} + \frac{r_F \sigma (T_F^2 - T_C^2)(T_F - T_C)}{r_C \left[\frac{1}{\varepsilon_F} + \frac{r_F}{r_C}\left(\frac{1}{\varepsilon_C} - 1\right)\right]}$$

or

$$= \frac{k_m P}{A_1 R^{1/2} h} + \frac{k_G}{C_1(R_F + R_C) + X_G + (g_F + g_C)} + \frac{r_F \sigma (T_F^2 - T_C^2)(T_F - T_C)}{r_C \left[\frac{1}{\varepsilon_F} + \frac{r_F}{r_C}\left(\frac{1}{\varepsilon_C} - 1.\right)\right]}$$

C.5 Heat Transfer in the Fuel

Heat transfer in the fuel is characterized using the steady state heat conduction equation to derive temperatures at any radius in the fuel. Thermal conductivity of the fuel material, as will be discussed under material properties, is assumed dependent on temperature and porosity remaining in the fuel material. Any consideration of fuel temperatures must account for the phenomona of fuel restructuring which changes both the geometry and density of the fuel over a portion of the radius. So while this is actually a material behavior mechanism it is discussed in section.

C.5.a Fuel Temperature

The heat transfer in the fuel is based on the method of calculating fuel temperatures described by Merkx and Fox[24] and was reviewed in the SIEX documentation. To find the temperature T at a radius r in the fuel the steady state heat conduction equation is used

$$\nabla\cdot(k\ \nabla\ T) = -\ q_v$$

where

$k = k(T,\rho)$ thermal conductivity of the fuel (temperature and density dependent)

q_v = volumetric heat generation rate

now in cylindrical coordinates ∇T is

$$\nabla T = \frac{\partial T}{\partial r}\ \bar{e}_r + \frac{1}{r}\ \frac{\partial T}{\partial \theta}\ \bar{e}_\theta + \frac{\partial T}{\partial Z}\ \bar{e}_Z$$

$$\nabla\cdot(k\ \nabla\ T) = \frac{1}{r}\ \frac{\partial(rk\ \frac{\partial T}{\partial r})}{\partial r} + \frac{1}{r}\ \frac{\partial(\frac{k}{r}\ \frac{\partial T}{\partial \theta})}{\partial \theta} + \frac{\partial(k\frac{\partial T}{\partial Z})}{\partial Z}$$

We assume one dimensional radial heat flow so

$$\frac{1}{r}\ \frac{\partial(rk(T)\ \frac{\partial T}{\partial r})}{\partial r} = -q_v$$

Rearranging for integration we obtain

$$d(rk(T)\ \frac{dT}{dr}) = -rq_v dr \qquad (24)$$

Let r_o and r_m be defined as in Figure 16, multiply Equation 24 by the arbitrary r and integrate from r_M to the radius r using the dummy variable β:

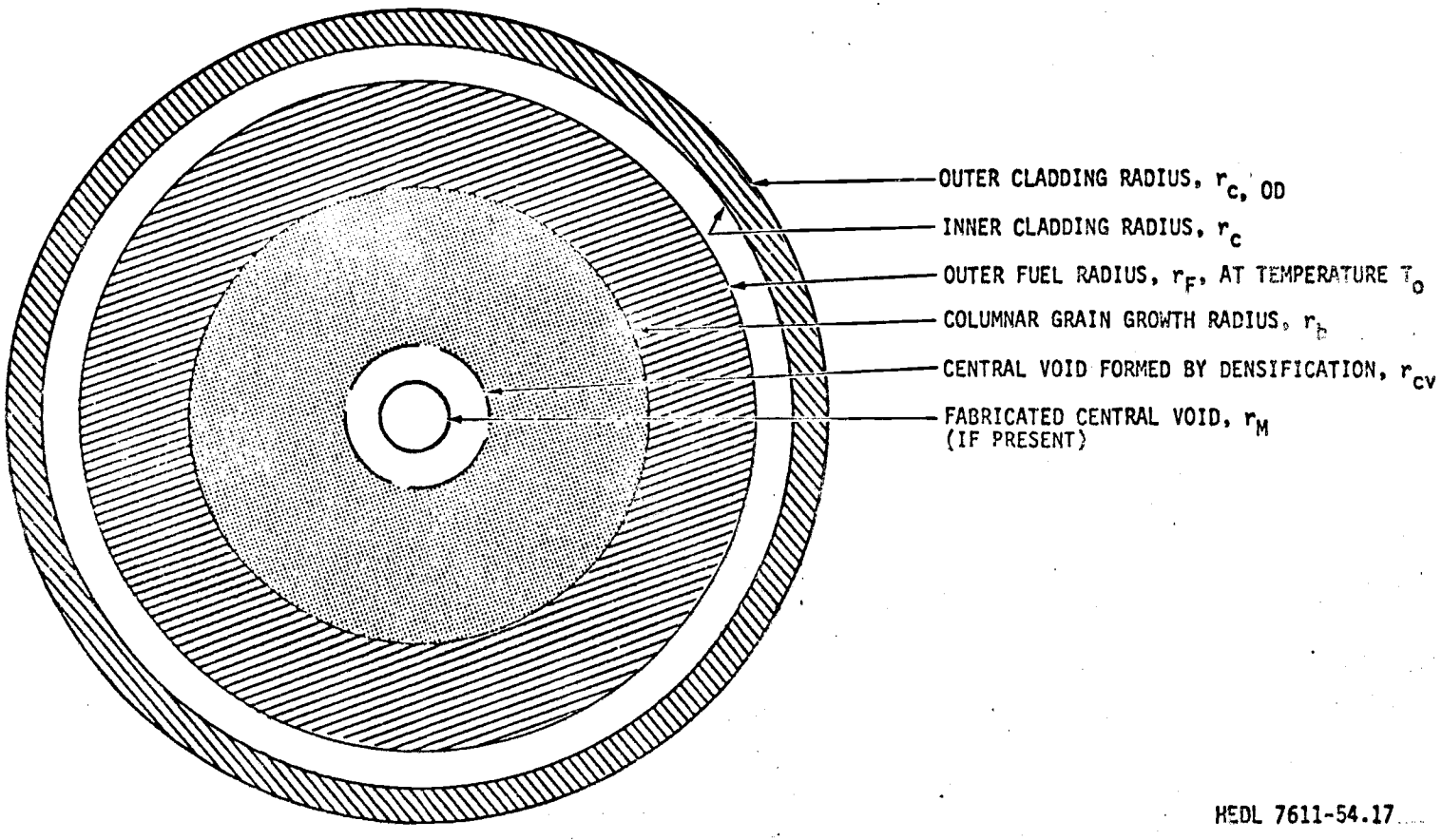

Figure 16. Fuel and Cladding Heat Transfer Geometry.

$$(25) \qquad rk(T)\frac{\partial T}{\partial r} = -\int_{r_M}^{r} \beta\, q_v(\beta)d\beta$$

Then dividing by r and integrating from r to r_F using new dummy variables ξ and γ we have:

$$\int_{T}^{T_o} k(\gamma)d\gamma = -\int_{r}^{r_F} \frac{1}{\xi} \int_{\xi_M}^{\xi} \beta q_v(\beta)d\beta d\xi$$

For a uniform density fuel in a fast flux, heat generation can be considered uniform across the radius (i.e. negligible self-shielding). Therefore we assume $q_v(\beta)$ is constant within an annular ring and thus can perform the integration of the last equation and obtain

$$(26) \qquad \int_{T}^{T_o} k d\gamma = -\frac{q_v}{2}\int_{r}^{r_F} \frac{1}{\xi}(\xi^2 - \xi_M^2)d\xi$$

$$= -\frac{q_v}{2}\left[\frac{r_F^2 - r^2}{2} - r_M^2 \ln (r_F/r)\right]$$

Introducing variables S_r and S_o to denote the integral of fuel conductivity at the radii r and r_F respectively, the Equation 26 can be written

$$(27) \quad [\int k(\gamma)d\gamma]_{T_r} - [\int k(\gamma)d\gamma]_{T_o} = S_r - S_o = \frac{q_v}{2}\left[\frac{r_F^2 - r^2}{2} - r_M \ln \left(\frac{r_F}{r}\right)\right]$$

This equation is used to calculate the fuel temperatures. The right side can be computed as a function of volumetric heat generation rate, q_V, the radius and surface temperature, T_o (to evaluate S_o). Once this is done a numerical method can be used to find the corresponding T_r associated with the value S_r found. The SIEX code uses a "table look-up" procedure to accomplish this, i.e., a table of $\int kdT$ (or S_r's) are cal-

culated for set 200°C intervals and the code then interpolates the value of T from the value of S_r, calculated by Equation 27 at radius r, using the table.

If fuel restructuring occurs (which in affect is a region of higher density fuel with a central void in it), as will be discussed in a following section, Equation 27 can be used to determine fuel temperatures in the sintered region by stubstituting (see Figure 16)

$S_o \rightarrow S_b = S(T_b)$ where T_b is the temperature above which fuel restructuring occurs

$$q_v \rightarrow q_{vb} = q_v \frac{r_b^2 - r_m^2}{(r_b^2 - r_c^2)}$$

Conservation of mass with the formation of higher density grain region and central void in the fuel.

$r_F \rightarrow r_b$

$r_M \rightarrow r_{cv}$

Thus Equation 27 is used up to the radius r_b and then the modified version is used in the restructured zone.

C.5.b Fuel Restructuring

A complete discussion of the heat transfer path in fast reactor fuel would not be complete without mention of fuel restructuring. The primary form, and the only one considered in this study, is the formation of columnar grains. During operation a radial temperature gradient is established across the fuel radius. Above a certain temperature isotherm porosity in the fuel migrates up the temperature gradient primarily in the form of lenticular voids. These sweeping voids form long "columnar" grains of higher density, at least 98% of theoretical

density, (T.D.). The voidage is deposited in the center of the fuel, Figure 17, forming a central void of significant size even at the low fuel burnups considered here. The porosity which is moved is primarily that left in the fuel during fabrication (fuel pellets are generally 90% T.D.), though generated fission gas can also be moved in this manner. The lenticular voids move by vapor transport mechanisms, see for example Nichols[25].

The effect of columnar grain growth is to lower fuel centerline temperature by:

1) A shortening of the heat path; assuming a constant mass balance across the radius, the material from the central void is considered moved and spread uniformly into the columnar grain region. Thus the volumetric heat rate is increased in the columnar grain zone.

2) Forming a higher density fuel zone which results in higher fuel thermal conductivity.

The effect on centerline temperature is significant (a typical decrease, for high power fuel originally of solid pellet configuration, would be 600°F) especially with respect to Q'_m. The columnar grain typically can extend to 70% of the fuel radius with a central void to 20% of it.

Secondary mechanisms by which additional voidage, in this instance from the fabricated fuel-to-cladding gap, is moved to the central void have also been postulated[26] by the author and co-scientists. These are needed to account for the majority of observed central void sizes

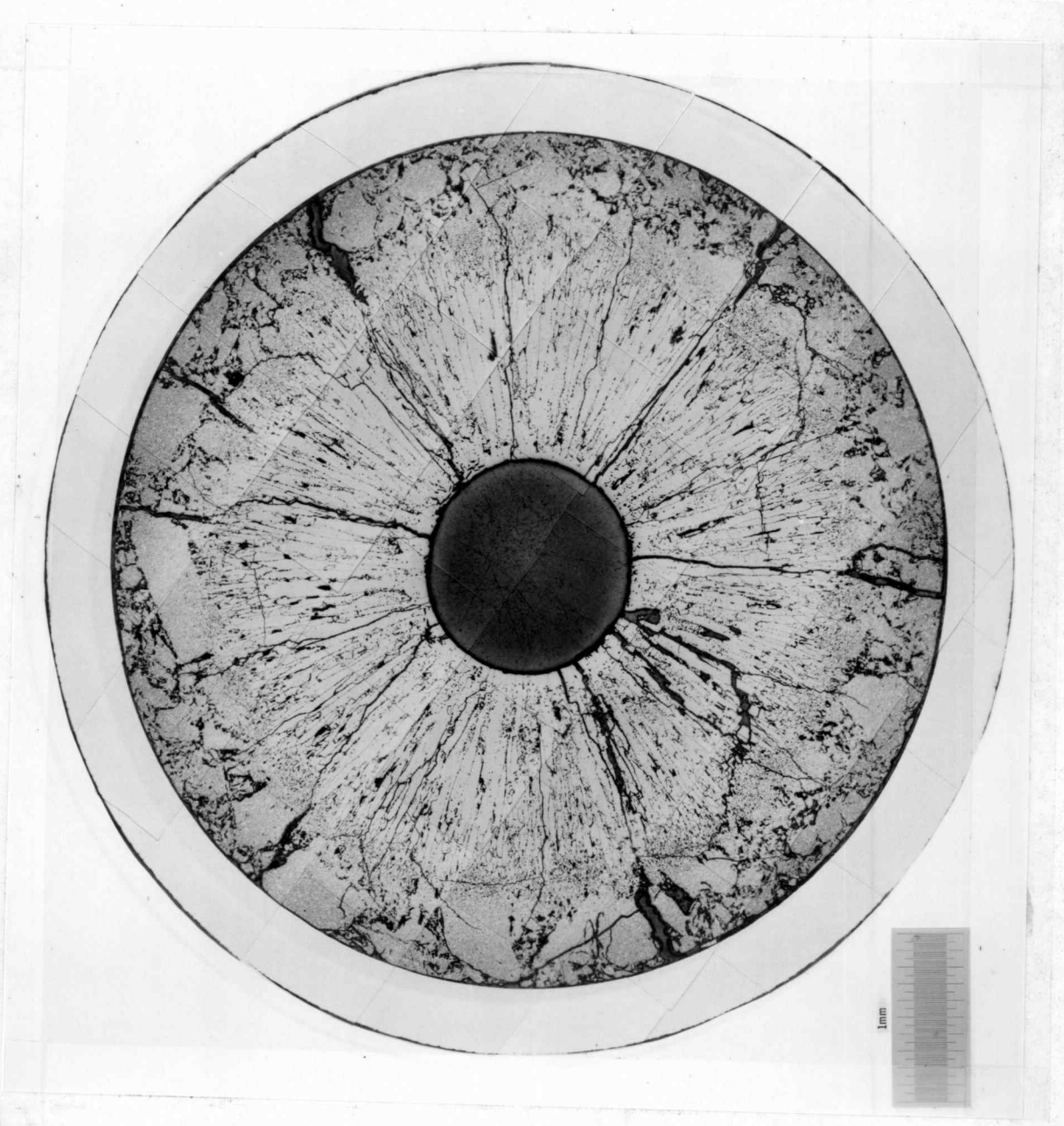

Figure 17. Example of Transverse Fuel Ceramography.

being larger than can be accounted for by a mass balance with the observed columnar grain size. This movement of porosity is caused by the fuel cracking during operation, the ratching outward of the cracked pieces, and the cracks being healed in the columnar grain region by the pore migration mechanism. Thus the OD of the fuel pellet is moved closer to the cladding and a portion of the original fuel-to-cladding gap is moved to the central void shortening the radius of the maximum heat path and decreasing the gap heat transfer coefficient.

D Review of Selected Material Properties

This section reviews those material properties that have direct effect on the heat transfer calculations described in Section C. Where detailed review was made a summary of the rationale used in the choice of the property will be made.

D.1 "Jump Distance" and Accommodation Coefficients for Fuel-to-Cladding Heat Transfer

In Section C.4.b the need for calculating temperature jump distances at each wall of the fuel-to-cladding gap were discussed briefly. The following summarizes a review made to define the best value of jump distance.

D.1.a Jump Distance

The accommodation coefficient was originally proposed by Knudsen[27] to account for observations he made of heat transfer across two surfaces in close proximity. He defined the accommodation coefficient "a", as the ratio between two temperature differences

$$a = \frac{\tau_2 - \tau_0}{\tau_1 - \tau_0}$$

here τ_0 denotes the temperature of the gas molecule impinging on the surface of a solid body at temperature τ_1, τ_2 then represents the temperature of the gas molecule after striking. "a" then represents the incomplete energy exchange between the molecule and the solid. The temperatures actually stand for the mean energies of the molecules.

Kennard[28] in his work defined a jump distance, g, as suggested by Poisson by the temperature drop divided by the temperature gradient in the bulk of the gas gap, Figure 18. Kennard obtained the following relationship between g and a:

$$g = \left(\frac{2 - a}{a}\right)\left(\frac{2}{1}\right)\left(\frac{k_G}{\mu C_V}\right)(\Omega)$$

or

$$g = \left(\frac{2 - a}{a}\right)\left(\frac{1}{1 + \gamma}\right)\left(\frac{k_G}{C_V P_G}\right)(2\pi RT)^{1/2}$$

where

C_p = Specific heat at constant pressure of the gas, cal/gm-°c

C_V = Specific heat at constant volume of the gas, cal/gm-°c

$\gamma = \frac{C_p}{C_V}$

k_G = Mean gas conductivity, W/cm - °c

μ = Absolute viscosity, gm/cm-sec

Ω = Mean free path of the gas molecules, cm

R = Mean gas constant, cal/gm - °c

T = Temperature of surface, °c

P_G = Pressure of the gas in the gap, $\frac{\text{dynes}}{\text{cm}^2}$

The total jump distance across a gap between the fuel and cladding, assuming that "a" is different at each surface, is:

$$g_1 + g_2 = \left[\frac{2 - a_1}{a_1} k_G \sqrt{T_1} + \frac{2 - a_2}{a_2} k_G \sqrt{T_2}\right]\left[\frac{\sqrt{2\pi R}}{(1 + \gamma)C_V P_G}\right]$$

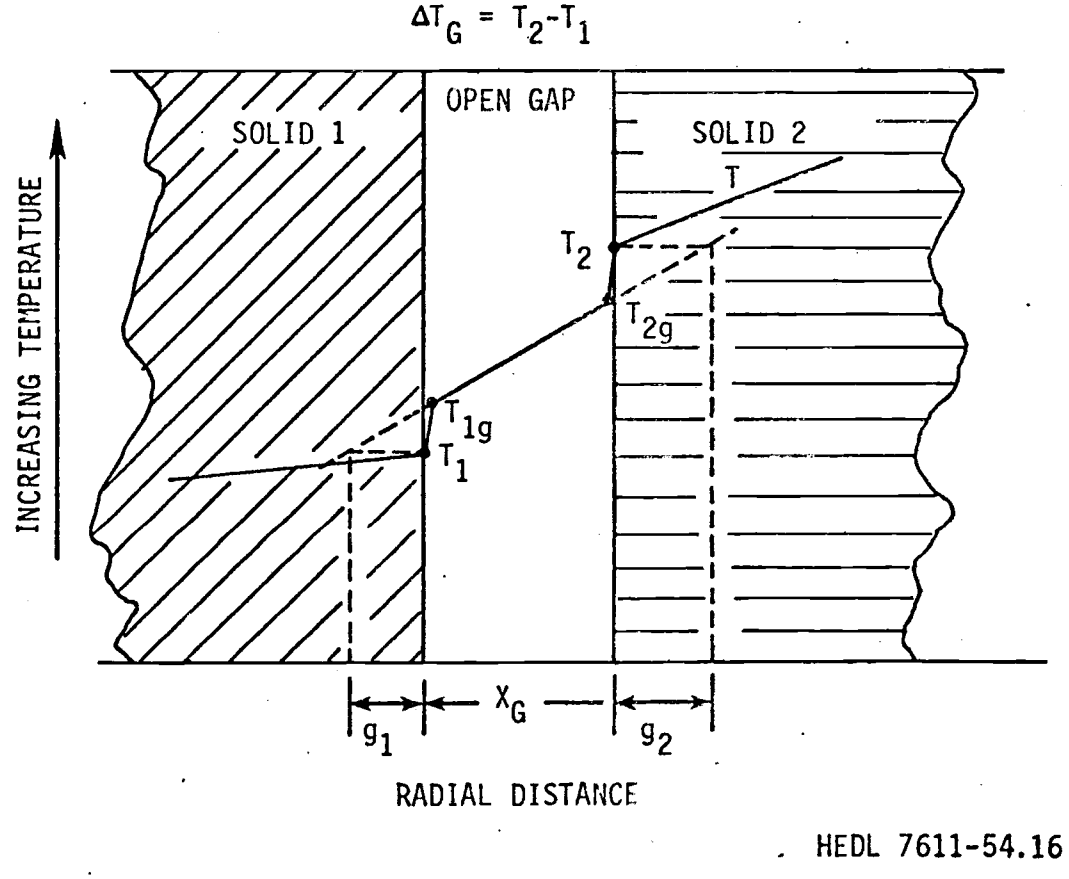

Figure 18. Example Showing Temperature Jump Distances at a Gap.

If we now assume that T_1 and T_2 can be replaced by an average temperature, $\bar{T}$, and k_1 and k_2 by an average gas conductivity, $\bar{k}$, calculated at $\bar{T}$, as was assumed in the past for SIEX[5], then:

$$g_1 + g_2 = \left[\frac{2 - a_1}{a_1} + \frac{2 - a_2}{a_2}\right]\left[\bar{k}\sqrt{\bar{T}}\right]\left[\frac{\sqrt{2\pi R}}{(1 + \gamma)C_V P_G}\right]$$

or

$$= 2\left[\frac{a_1 + a_2 - a_1 a_2}{a_1 a_2}\right]\left[\frac{\bar{k}\sqrt{\bar{T}2\pi R}}{(1 + \gamma)C_V}\right]$$

in terms of the harmonic mean of the accommodation coefficients, $\tilde{a}$, = $\frac{2a_1a_2}{(a_1 + a_2)}$

$$(28) \qquad g_1 + g_2 = 2\left[\frac{2}{\tilde{a}} - 1\right]\left[\frac{\bar{k}\sqrt{2\pi R\bar{T}}}{(1 + \gamma)C_V}\right] .$$

Equation 28 can be evaluated using the following known values:

$(1 + \gamma)\gamma = 2.659$ assuming a monotomic gas[5]

$\bar{W} = \sum_{i=1}^{n} f_i W_i$, the average atomic weight of the "n" gases in the fuel-to-cladding gap, gm/mole

f_i = mole fraction of each gas

W_i = atomic weight of each gas

$C_V = \dfrac{\sum_{j=1}^{n} f_{wj} \tilde{C}_{vj}}{\bar{W}}$, specific heat at a constant volume for the gas mixture in the gap based on Kennard[28].

[5]While some nitrogen (N_2) is present, the added complexity of adjusting does not appear warrented considering the accuracy of other variables.

$f_{wj} = \frac{f_j W_j}{\bar{W}}$, weight fraction of each gas

$\tilde{C}_{vj} = 2.988$, specific heat at a constant volume for each gas, $\frac{cal}{mole\text{-}°C}$

Thus

$$C_v = \frac{2.988 \sum_{i=1}^{n} \frac{f_i W_i}{\bar{W}}}{\bar{W}} = 2.988/\bar{W}$$

Similarly

$$R = 1.99/\bar{W}.$$

Thus combining we have:

$$(29)\quad \frac{2\sqrt{2\Pi R}}{(1+\gamma)C_v} = \frac{2\sqrt{(6.283)\left(\frac{1.99 \text{ cal/mole - °K}}{\bar{W} \text{ gm/mole}}\right)\left(4.186\times10^{7}\frac{erg}{cal}\right)}}{(2.659)\left(\frac{2.988 \text{ cal/mole - °K}}{\bar{W} \text{ gm/mole}}\right)\left(4.186\times10^{7}\frac{erg}{cal}\right)}$$

$$= 1.376\times10^{-4}\sqrt{\bar{W}}\left(\frac{gm\text{-°k}}{erg}\right)^{1/2}$$

Recalling 1 erg = 1 cm - dyne = 1 $\frac{gm - cm^2}{sec^2}$; assuming $\bar{k}$ is in W/cm - °K, noting that a Watt-second = 10^7 ergs and substituting Equation 29 into 28 gives:

$$g_1 + g_2 = \left[\frac{2}{\bar{a}} - 1\right]\left[\frac{(\bar{T}\bar{W})^{1/2}}{P}\right][1.376\times10^{-4}][10^7]$$

$$= \left[\frac{2 - \bar{a}}{\bar{a}}\right]\left[\frac{\bar{k}(\bar{T}\bar{W})^{1/2}}{P_G}\right][1376], \text{ cm}$$

D.1.b Accommodation Coefficient

Assuming the classical methods and only elastic collisions between gas and metal molecules Jeans[29] found:

$$(30) \qquad a = 1 - \left(\frac{M_G - M_W}{M_G + M_W}\right)^2 = \frac{4M_G M_W}{(M_G + M_W)^2}$$

where:

M_G = Atomic mass of the gas, gm/mole

M_W = Molecular mass of the wall, gm/mole

This, as noted by Jeans, does not give good agreement with the data in the case of small gaps. For this reason, the collision probability with other atoms, particularly oxygen, needs to be considered. Assuming a monotomic gas, the probability of collision of a gas atom with the plutonium (or uranium), and oxygen atoms can be approximated as being proportional to the cross-section of each and to the number present. As stated by Giuliani and Mustacchi[31], this cross-section can be estimated proportional to the 2/3 power of the atomic weight of each atom. This follows from the radius of an atom being proportional to the cube root of the atom's mass and the cross-section in turn being proportional to the square of the radius.

Thus, Equation 30 above for a molecular solid and monotomic gas (assuming the wall molecule composed of N_1 atoms of atomic mass M_1 plus N_2 atoms of mass M_2, etc.) is:

$$a = C_a \left[\sum_{i=1}^{m} \frac{4M_G M_i}{(M_G + M_i)^2} \quad \frac{N_i M_i^{2/3}}{\sum_{j=1}^{\ell} N_j M_j^{2/3}} \right]$$

where

C_a = constant of proportionality to be determined

M_G = the atomic mass of the gas

summing limits m = ℓ = the number of types of atoms in the wall molecule. So

$$(31)\quad a = C_a \left[\frac{4M_G}{\sum_{j=1}^{\ell} N_j M_j^{2/3}} \sum_{i=1}^{m} \frac{N_i M_i^{5/3}}{(M_G + M_i)} \right]$$

Giuliani and Mustacchi[31] performed experiments with Al-UC surfaces and assumed a UO_2 and Al_2O_3 surface existed. They found reasonably good agreement between the shape of the experimental and theoretical curves, a versus M_G, (C_a = 1) but observed as much as 30% discrepancy in absolute values. Values were slightly underpredicted up to a gas atomic mass of 6 and constantly over predicted for the remainder of atomic mass values up to 200. The over prediction was a fairly constant 30%. Based on this and another study with two Al surfaces they concluded the equation should be corrected by downward 30% (C_a = .7). They also found <u>no</u> detectable temperature dependence between 450° and 750°K.

Ullman et al[35] have measured "a" for Xe and He gas on surfaces of 316 stainless steel and UO_2. They measured a definite temperature dependence for their data between 500 and 1200°K. These data are not gobal values but were measured at a particular incident and reflection angles which was expected to be qualitatively applicable to global energy exchange. As seen in Table XI, using the middle of their temperature range and comparing it to the results of Equation 31 with C_a = 1, He is in agreement but for Xe the difference is on the order of that observed by Giulacani and Mastacchi. No attempt was made to clean the surfaces of the UO_2 or 316 SS used in this work.

TABLE XI

COMPARISON OF ACCOMMODATION COEFFICIENT VALUES

	Equation 31*, $C_a = 1$			Ref.10, 800°K	
	a_{Fuel}	a_{Clad}	$\bar{a}$	a_{Fuel}	a_{Clad}
He	.21	.25	.23	∿.21	∿.20(∿.20)**
Xe	.79	.84	.81	∿.61	∿.50(∿.61)
Kr	.71	.96	.82	--	--
N_2	.52	.89	.65	--	--
Ar	.57	.97	.72	--	--

*Assume cladding Fe and fuel UO_2

**Values in "( )" for $\Theta_i = 60°$, $\Theta_r = 30°$ all others $\Theta_i = \Theta_r = 45°$

Godesar et al[30] reviewed briefly the method used in COMETHE II and presented a graph of "a" versus gas atomic weight. While an explanation of the meaning of the material pairs of each curve is not given, they appear similar to the mean of values calculated by Equation 31.

Prior work with SIEX[5] was based on values of Godesar et al[30]. While the temperature dependence of "a" appears real based on Ullman et al[35] and work by Trilling[36] it is not believed enough data is available at this time to warrent adding the complexity to the models. Also as pointed out by Dushman[32] and Dean[8] the condition of the surfaces has a direct effect on "a", the rougher the surface the higher "a" becomes. Thus it appears the values from Equation 31, letting $C_a = 1$ when M_G is less 6 and $C_a = .75$ for masses greater than 6, should give sufficiently accurate values. This is true especially when the uncertainty of the surface conditions of the fuel and cladding in-reactor are considered. Table XII summarizes the values of "a" pertinent to

this study assuming walls respond similar to UO_2 and Fe.

TABLE XII

VALUES OF a TO BE USED IN STUDY

	a_{Fuel}	a_{Clad}	$\bar{a}$
He	.21	.25	.23
Xe	.59	.63	.61
Kr	.53	.72	.62
N_2	.39	.67	.49
Ar	.42	.73	.54

Finally, since the gas in the fuel-to-cladding gap is made up of a mixture of at least five gases, the accommodation coefficient of the mixture must be considered. We assume the expression used by Mikami et al[33] and W-ARD[31] to be valid:

$$(32) \qquad a_{mixture} = \frac{\sum_j f_j a_j/(\sqrt{W_j})}{\sum_j f_j/(\sqrt{W_j})}$$

a_j = Accommodation coefficient for each gas

W_j = Atomic weight of each gas

f_j = Concentration of this gas

Sums taken over the five gases present.

D.1.c Summary of Calculation of Jump Distance

For the analysis of P-19 and P-20 then we propose to use the corrected version of Equation 31, $C_a = 1$ when $M_G < 6$ and $C_a = .75\ M_G > 6$, to find the accommodation coefficient, a_{ij}, at each surface of the gap (i = 1, 2) and for each component of the plenum gas (j - 1 to 5). Then use

Equation 32 to find the accommodation coefficient, a_i, for the gas mixture at each surface of the gap. Finally to find the harmonic mean $\bar{a}$ ($\bar{a} = \frac{2a_1a_2}{(a_1 + a_2)}$) and use this result in Equation 28 to find the total jump distance $(g_1 + g_2)$ for the fuel-to-cladding gap, see Table XII.

D.2 The Thermal Conductivity of Gas in the Fuel-to-Cladding Gap

The thermal conductivity of the gas, k_G, present in the fuel-to-cladding gap is very important to the calculation of heat transfer through this region, as was previously noted in Section C. A significant amount of heat is transferred through the gas even when there is solid-to-solid contact between the fuel and cladding.

D.2.a Thermal Conductivity of the Pure Gases He, Xe, Kr, Ar and N_2

Two possible methods of representing individual gas values were considered. The first was calculation of values from theoretically based equations such as the Chapman-Enskog formula recommended by Bird et al[37]:

(33) $$k = 1.9891 \times 10^{-4} \frac{\sqrt{T/M}}{\sigma_L^2 \Omega_k}$$ monotomic

k = Gas thermal conductivity, $\frac{cal}{cm\text{-}sec\text{-}°K}$

T = Temperature of gas, °K

M = Molecular weight, gm

σ_L = Characteristic diameter (different from molecular diameter) from Lennard-Jones potential function, A

Ω_k = Collision integral, dependent on the dimensionless temperature $K \cdot T/\varepsilon$

where

K = Boltzman's Constant.

ε = Characteristic energy in interaction from Lennard-Jones potential function.

For gases which are not monotomic, thermal conductivity can be calculated from[37]:

(34) $$k = \left(C_p + \frac{5}{4}R\right) \mu$$

C_p = Heat capacity at constant pressure, $\frac{cal}{gm - °K}$

R = Gas constant, $\frac{cal}{gm - °K}$

(34a) μ = viscosity, $\frac{gm}{cm\ sec}$

$$= \frac{2.67 \times 10^{-5}(MT)^{1/2}}{\sigma_L^2 \Omega_k}$$

[while Equation 34a was derived from monotomic gases, it has been found in good agreement for polyatomic gases as well]

Predictions from these equations have been found to be in good agreement[37] with measured gas thermal conductivity data. Equations similar to this have been used directly by Horn and Panisko,[6] Lloyd, et al,[38] and Hann and Lanning[13] in their work in the area of gap conductance. The second method for handling conductivity is to develop an expression which is simply a mathematical fit of the available measured thermal conductivity data for these gases. This was done in the past in

the development of both SIEX[5] and FMODEL[39] computer codes. It was this later method which was chosen to be used to the present analysis and calibration effort. This method is consistant with the past formulation of the SIEX code, which will be used exclusively in this work, and it should lead to values of conductivity which are at least as accurate as values produced by the first method, as long as sufficient data is available.

Available references with conductivity data on the five gases in question were reviewed. It was decided to use the results of the "Thermophysical Properties Research Center Data Book[40]", as a primary source. These data have been reviewed in several reports. Reference 41, a National Bureau of Standards report, includes the results from the Data Book for He, Ar and N_2. Reference 42, a paper presented at Fourth Symposium on Thermophysical Properties, is a "capsule summary," by Liley, of the material presented in the Data Book on the thermal conductivity of 46 gases. The later data source was used in part in the past to derive the gas thermal conductivity expression used in the SIEX code.

The range of temperatures of interest to fuel-to-cladding gap conductance is 0.0 to 2500°C. Data from the above described source was used for He, Ar and N_2. However, Xe and Kr data from this source was only available to about 450°C. For this reason, additional sources of data were reviewed and used for Xe and Kr. These included work by Dymond,[43] Massey,[44] Saxena[45], and Collins and Menard[46]. These extended the data base for the two gases to at least 2100°C.

A quadratic expression of temperature was mathematically fit to the data. The resulting coefficients found are shown Table XIII.

All data was at atmospheric (14.7 psi) pressure. Gas pressure in fuel pins typically range up to 800 psi at end-of-life, 80,000 MWd/MTM. Figure 8.2-2 of Bird et al.,[37] which represents reduced thermal conductivity as a function of reduced pressure was used to evaluate the effect of pressure on gas conductivity in the ranges of interest. The conductivity correction for several extremes for individual gases were calculated and it was concluded no correction of the correlations for pressure was needed.

D.2.b Conductivity of Gas Mixture

The thermal conductivity of the mixture of five gases is needed to calculate the temperature drop through the open portion fuel-to-cladding gaps. Data on high temperature mixtures of He-Xe-Kr gases is scarce and apparently does not exist for all five gases combined.

Two forms of equations for calculating the gas conductivity of gas mixtures from individual gas conductivity values were considered. The first was proposed to Brokaw[47] as an empirical and simple method for calculating conductivity of gas mixtures:

$$k_M = \underline{b}\ k_{SM} + (1 - \underline{b})\ k_{RM} \tag{35}$$

where:

$$k_{SM} = \sum_{i=1}^{n} X_i k_i \quad \text{(simple mixing)}$$

$$k_{RM} = \frac{1}{\sum_{i=1}^{n} \frac{X_i}{K_i}} \quad \text{(reciprocal mixing)}$$

TABLE XIII

GAS CONDUCTIVITY COEFFICIENTS

$$k = \gamma_1 + \gamma_2 T + \gamma_3 T^2$$

$$k \rightarrow \frac{W}{cm - {}^\circ C}$$

$$T \rightarrow {}^\circ C$$

Coefficient	Helium (He)	Xenon (Xe)	Kripton (Kr)	Nitrogen (N_2)	Argon (Ar)
γ_1	1.43×10^{-3}	5.15×10^{-5}	9.05×10^{-5}	2.72×10^{-4}	1.83×10^{-4}
γ_2	3.17×10^{-6}	1.69×10^{-7}	2.47×10^{-7}	4.81×10^{-7}	3.58×10^{-7}
γ_3	-2.24×10^{-10}	-3.50×10^{-11}	-4.89×10^{-11}	$+9.68 \times 10^{-12}$	-2.32×10^{-11}

k = Thermal conductivity

X = Mole fraction

$\underline{b}$ = Dimensionless factor

Subscripts;

i = Components of mixture, 1 to 5 in this case

M = Mixture

Brokaw presented this equation primarily with binary gas mixture data. From analysis of these data, it was found $\underline{b}$ varied between 0.3 to 0.8, and increased with increasing fraction of the light constituent of the gas mixture (e.g., He). The agreement with the data were found to be good using $\underline{b}$ as a function of the light constituent. It was further stated that Equation 35 could be applied to multicomponent mixtures as long as the variation of $\underline{b}$ was known. However, it was noted little data was (and is) available, and as a rough approximation, $\underline{b}$ 0.5. This leads to the equation:

(36) $$k_M = 0.5\ (k_{SM} + k_{RM})$$

$$k_M = 0.5\ \left(\sum_{j=1}^{n} X_j k_h + \frac{1}{\sum_{i=1}^{n} \frac{X_i}{k_i}}\right).$$

This equation was also referenced in Massy's[44] review, and used in the past in SIEX. However, it appears to lead to significant errors when the light constituent is not 50 to 70 percent of the mixture. The comparisons of data to Equation 36 predictions sited by Brokaw[47] for some ternary mixtures fall in this favorable range of percentage of

light constituent and show good agreement. But as shown in Table XIV using data from Ubisch,[48] the errors from this form are significant. However, the errors show the same trend noted by Brokaw for binary gas mixtures.

A fit of Brokaw's correction curve for binary mixtures is:

$$\underline{b} = 0.45\, X_1^2 + 0.3X_1 + 0.32 \tag{37}$$

where:

X_1 = Mole fraction of Helium

When this expression is used for $\underline{b}$ with Equation 36 the agreement of predicted and measured values, as noted in Table XIV, is greatly improved.

The second equation form for calculating the conductivity of the gas mixture is a theoretically based one, recommended by Bird et al[37] for gases at low density, credited to Mason and Saxena:[49]

$$k_M = \sum_{i=1}^{n} \frac{X_i K_i}{\sum_{j=1}^{n} X_j \Phi_{ij}} \tag{38}$$

$$\Phi_{ij} = \frac{1}{\sqrt{8}} \left(1 + \frac{M_i}{M_j}\right)^{-1/2} \left[1 + \left(\frac{\mu_i}{\mu_j}\right)^{1/2} \left(\frac{\mu_j}{\mu_i}\right)^{1/4}\right]^2$$

(Terms are defined in previous Equations 33 and 34).

Viscosity, μ, can be calculated from Equation 34a . Values for σ_L and ε/K for each pure gas are given in Bird et al[37] and Hirschfelder

TABLE XIV

COMPARISON OF THERMAL CONDUCTIVITY OF GAS MIXTURES

Fraction in Gas Mixture				Measured[48]	Calculated Conductivity					
He	Xe	Kr	Ar	Conductivity W/cm-°C	Eq. 36, W/cm-°C	% Error	Eq. 35 & 37 W/cm-°C	% Error	Eq. 38, W/cm-°C	% Error
.2190	.6950	.0860	0.0	0.360×10^{-4}	0.470×10^{-4}	30.5	0.379×10^{-4}	5.3	0.381×10^{-4}	5.8
.8650	.0290	.1060	0.0	2.143	1.805	-15.8	2.108	-1.6	2.208	3.0
.4800	.4580	.0820	0.0	0.787	0.888	12.8	0.810	2.9	0.8.9	4.1
.8690	.1210	.0160	0.0	2.126	1.706	-19.8	2.053	-3.4	2.098	-1.3
.2450	.1620	.5930	0.0	0.477	0.560	17.4	0.466	-2.3	0.498	4.4
.5190	.1030	.3780	0.0	0.942	1.007	- 6.9	0.951	.95	1.015	7.7
.2480	.6330	.1190	0.0	0.409	0.518	26.7	0.420	2.7	0.425	3.9
.2270	.3790	.3940	0.0	0.417	0.509	22.1	0.418	.2	0.436	4.6
.2400	0.0	.7600	0.0	0.507	0.572	12.8	0.482	-4.9	0.522	3.0
.8800	0.0	.1200	0.0	2.306	1.911	-17.6	2.211	-4.1	2.317	.5
.2020	.7980	0.0	0.0	0.322	0.437	35.7	0.351	9.0	0.348	8.1
.4180	.5820	0.0	0.0	0.624	0.776	24.4	0.677	8.5	0.675	8.2
.7870	.2130	0.0	0.0	1.651	1.464	-11.6	1.693	2.2	1.710	3.2
.4900	0.0	.5100	0.0	0.942	0.981	4.1	0.912	-3.2	0.991	5.2
.2900	0.0	0.0	.7100	0.749	0.807	7.7	0.720	-3.0	0.781	4.3
.4590	0.0	0.0	.5410	1.088	1.092	.4	1.022	-6.1	1.109	1.9
.8940	0.0	0.0	.1060	2.470	2.470	-10.4	2.429	-1.7	2.482	.5

et al.[50] Also tabulated in these references is Ω_K as a function KT/ε. This table was mathematically fit to the function:

$$\Omega_k = 0.639 + \frac{1.086}{0.135 + (K\frac{T}{\varepsilon})^{.838}} + 0.000482\ (K\frac{T}{\varepsilon})$$

for inclusion in the SIEX prediction code.

Table XIV shows a comparison of applicable experimental results (at 520°C) from Ubisch[48] for some of the gases of interest to this study. Also shown are the calculated values from Equations 35, 36 with 37, and 38, using the data fits, Table XIII, of thermal conductivity previously described for the pure gases. As can be seen, the Brokaw equation with b defined by Equation 37 and the theoretically based Equation 38 are about comparable in agreement with the experimental data.

For the present analysis, it was decided to use the theoretical based Equation 38. More confidence can be implied to the theoretically based equation in extrapolating to the mixtures of the five gases of interest, where there is no actual data to verify the form of b for the Brokaw equation.

D.3 Cladding Yield Strength

The model for solid-to-solid heat conductance, in Section C.4.a requires the use of the yield strength of the softer wall material. This was substituted for Myer's hardness since the values should be proportional and yield values are more readily available. A review of the yield strength of the mixed-oxide fuel (about 100 ksi at 1000°F) and the 316 20% CW stainless steel cladding (about 70 ksi at 1000°F) shows

the cladding to be the softer material.

The yield strength data from Reference 51 was used to obtain the following expression for the 316 stainless steel cladding material:

$$y_C = 4.82 \times 10^9 - 1.08 \times 10^7 \, (T - 555°C), \frac{dynes}{cm^2}$$

D.4 Fuel and Cladding Surface Roughness

Surface roughness of the fuel and cladding is a value used in the basic fuel-to-cladding heat transfer equations found in Sections C.4.a and C.4.b. Because roughness, as previously noted, was not measured on the experimental fuel or cladding used in P-19 and P-20, and is not presently being measured on production fast reactor fuel pins, these were combined into a constant A_2 and B in Equations 15 and 19. However for future comparisons typical values of roughness found by other investigators will be suggested here.

Work by Jacob and Todreas[12] showed, summarizing all available data for unirradiated studies, the following ranges:

Cladding roughness, R_C, 3 to 465 μ inch.
(8×10^{-6} to 118×10^{-5} cm)

Oxide Fuel Roughness, R_F, 8 to 685 μ inch.
(20×10^{-6} to 174×10^{-5} cm)

For consistant comparison with past work at HEDL the following "typical" roughness values are assumed;

$$R_C = 3.30 \times 10^{-4} \text{ cm}$$

$R_F = 1.78 \times 10^{-4}$ cm

so $\bar{R} = 2.65 \times 10^{-4}$ cm, $(\bar{R}^{1/2} = .0163)$.

D.5 Emissivity of the Fuel and Cladding

Two sources[52][53] were reviewed for fuel emissivity values. These studies were made on UO_2 which should apply directly to the PuO_2 - UO_2 fuel of concern here. Emissivity, like the accommodation coefficients, is very dependent on surface conditions which have not been characterized in-reactor where fission products may accumulate. Because of this and an uncertainty that appears to exist in the temperature dependence; a single value, $\varepsilon_F = 0.80$, is used as the hemispherical total emissivity of the fuel. This value was taken from Belle's[52] compilation which was for a spectral wave length of 6500 angstroms and a temperature of about 1050°C (1900°F). This value is in the middle of the range of values, 0.7 to 0.9, found by Held and Wilder[53].

There is little data available on the oxidized surface of the stainless steel cladding. For the cladding surface we assume again a single value, $\varepsilon_c = 0.9$, for the total hemispherical emissivity based on data in Reference 54.

D.6 Fuel and Cladding Thermal Expansion

The size of the fuel-to-cladding gap during the test is critical to the mode of heat transfer in the gap. The differential thermal expansion of the fuel and cladding is one of two mechanisms considered to close this gap, and thus the assumptions made about the expressions used are very important.

For fuel thermal expansion we use the expression recommended by Bard et al[55] which is based on UO_2 data of Conway, Fincel and Hein[58].

$$\alpha_F = 6.8\times10^{-6} + (2.9\times10^{-9})T, \ (°C)^{-1}$$

No dependence on the oxygen-to-metal ratio, O/M, is considered here because of the uncertainty in its effect. Also no consideration is made of the volumetric increase that is observed (about 10%) when fuel melting occurs. It is believed any stress caused by the amounts of melting observed in the tests will be relieved by movement of the molten fuel axially in the central void, and will thus have no radial effect.

The thermal expansion of the 316 20% CW stainless steel cladding is based on the ASME Boiler and Pressure Vessel Code[57] and Braun[58] (temperatures from 150°C to 650°C):

$$\alpha_c = 16.55\times10^{-6} + (3.68\times10^{-9})T, \ (°C)^{-1} \ .$$

D.7 Thermal Conductivity of the PuO_2 - UO_2 Fuel

After review and evaluation of the thermal conductivity data and recommendations on the $.25PuO_2$ - $.75\ UO_2$ fuel it was decided to use an expression proposed by WARD[59]:

$$(39) \qquad k_F = D_I\left[\frac{1}{2.88 + 0.0252T_a} + (5.83\times10^{-13})T_a^{\,3}\right]$$

where

$$D_I = \begin{cases} 21.\rho - 10 - 10\rho^2 = \dfrac{2.1\rho - 1 - \rho^2}{.1}, & \text{when } .85 \le \rho \le .95 \\ \dfrac{3\rho - 1}{2} = 1.5\rho - 0.5, & \text{when } .95 \le \rho_f \le 1.0 \end{cases}$$

or

$$\frac{2 - 3P_f}{2} = 1. - 1.5P_f, \text{ when } 0.05 \leq P_f \leq 0.0$$

=

$$\frac{.1 - .1P_f - P_f^2}{.1} = 1. - P_f - 10P_f^2, \text{ when } 0.15 \leq P_f \leq 0.05$$

P_f = Fraction porosity

ρ = Fraction of theoretical density

T_a = Temperature, °K

k_F = Thermal conductivity, W/cm - °K

Data on thermal conductivity of PuO_2-UO_2 is very limited at this time. The data are all from unirradiated, unrestructured fuel and only one study includes data for temperatures above 1700°C (most fresh fuel in these tests had centerline temperatures above melting, 2760°C). The primary source for the review was the extensive survey made by Washington[60]. Other sources [59, 61, 62] including those used for SIEX in the past were also considered. Equation 39 has been used in past versions of SIEX and resulted in very reasonable models for fuel restructuring and gap behavior after code calibration.

A brief summary follows of the dependences of thermal conductivity, k_F, of the fuel to help clarify the difficulties involved in characterizing this property. Thermal conductivity of the ceramic fuel is dependent on:

1) Temperature

2) Porosity

   a) Concentration

b) Form

c) Gas composition within

3) Oxygen to metal ratio (O/M) in the fuel

4) Restraint

5) Pu content

The first two dependencies are primary. The third has a major effect out-of-reactor however in-reactor the effect is uncertain. The remaining two dependencies are secondary because of lack of effect or lack of data to quantify the effect.

The temperature dependence noted in Figure 19 for Equation 39 agrees well with the available data between 500 and 1700°C described by Washington[60]. Nearly all fuel conductivity expressions for PuO_2-UO_2 derived in the literature use the same temperature dependence form used in Equation 39, which accounts for the upturn observed in the UO_2 data at high temperatures. Since there is little direct information for PuO_2-UO_2 fuel above 1700°C there is a large uncertainty in the expressions above this point.

There are a number of different forms of equations being currently used to account for the affects of porosity on thermal conductivity. Equation 39 uses a reduced Maxwell equation (see "D_1" in Equation 39). A further assumption[63] is made in the equation that there is a greater effect of porosity when the pore volume greater than 5%, implying the pore morphology is not spherical. Below 5% this Equation 39 assumes the equivalent to a Eucken relationship for dilute concentrations of spherical pores. This is reasonable because in this study densities greater

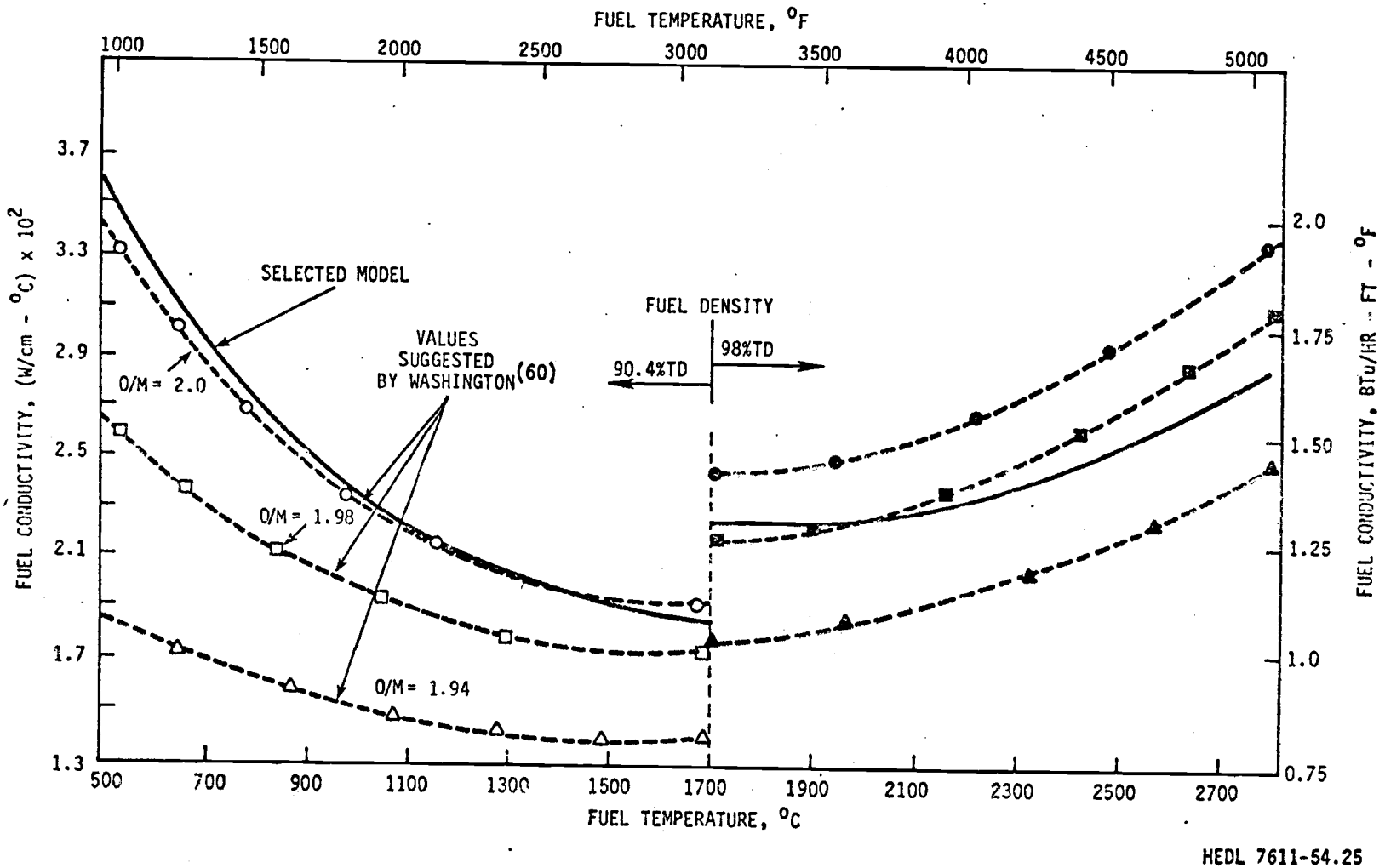

Figure 19. Thermal Conductivity of Mixed-Oxide Fuel.

than 95% are in columnar grain zones while those less than this are unrestructured fuel. Since the unrestructured fuel has nonspherical pores (except for one P-20 pin) because a high pressure preslugging fabrication method was used, this assumption appears to be valid.

It should be noted that the thermal conductivity of the columnar grain zone may indeed be higher than that directly calculated from the unrestructured fuel porosity form. This would follow because the region is made up of high density radial stringers with porosity, probably spherical, along the edges. This region bears little resemblence to the unrestructured pore/fuel system.

The effect of O/M ratio in the fuel on fuel conductivity (PuO_2-UO_2) has been found to be significant in out-of-reactor tests, see Figure 19. However in-reactor the O/M of the fuel varies across the radius from the fabricated values. The trend is for O/M to increase at the fuel OD and decrease toward the center. Because of the lack of an accepted O/M model and the lack of confirming in-reactor work the O/M variable will not be considered in this study. It should, however, be noted that Equation 39 was derived on the assumption of O/M being equal to 1.98 in the fabricated fuel.

Data from the study described in Appendix J of Reference 3, where fuel conductivity was derived from specimens from one fuel pellet from each fuel batch used in P-19, were not used in the present study. All the fuel (except for two pins) in P-19 and P-20 was fabricated by a high pressure preslugging technique[4] which results in interconnected porosity. The majority of the data used for Equation 39 was from fuel fabricated

with techniques that result in closed porosity. The results of the study[3] on P-19 fuel showed there was as much as 30% lower k_F for it compared to the closed porosity fuel. It was decided not to use this study, however, because:

1) It is believed that there was not a statistically significant number of values taken, considering the randomness of the preslugged fuel structure[4].

2) Studies by the author, using a Hybrid computer version of SINTER[24], showed a negative gap conductance was needed for some P-19 data to match the melting observed when using the measured k_F values. This would indicate too low a fuel conductivity.

3) An in-reactor Q'_m study made by Gibby and Lawerance[63], for the two types of fuel showing a similar difference (about 30%) in k_F, resulted in a calculated difference of only 3 to 6% in Q'_m. This appears to be in the uncertainty for normalizing the test data from the two batches of fuel.

Thus equation 39 was chosen to represent data from the literature and does not include the limited data on the two fuel pellets from P-19.

D.8 Fuel Melting Temperature

Review of the solidus melting temperature for 25% PuO_2-75% UO_2 lead to choosing the value 2760°C (5000°F). This is based on work by Aitken and Evans[64, 66] who used the same technique as Lyon and Baily[65] but with improved pyrometric equipment. No adjustment is assumed for burn-

up[60]. Also though there may be some O/M dependence it is not clear at this time what it is because of limited data.

E Review of Fuel Behavior Related to Gap Conductance

The basic concern of this report is the fuel-to-cladding heat transfer. However, for LMFBR fuel pins, a fully independent heat transfer code must include models for phenomena beyond basic material properties of Section D. These include:

- Fuel-to-cladding gap closure due to fuel cracking and swelling
- The release during irradiation of gases absorbed in the fuel during fabrication (H, N_2 and Ar)
- The release of fission gases (Xe and Kr)
- The restructuring of the fuel

It is beyond the scope of this study to develop detailed models necessary for these items because a data base much larger and more varied than that from the two tests of concern here, needs to be used. This has been done in the past at HEDL with the SIEX code[5] and is planned in the near future.

For development of the constants concern with gap conductance, which will be calibrated in Section F, only one of these models is used, that for the fuel-to-cladding gap closure. The remaining values needed on gas release and fuel restructuring were input directly based on measured data from the pins. This follows as the second step in the method, Figure 20, developed previously for calibration of SIEX and allows the most meaningful model development.

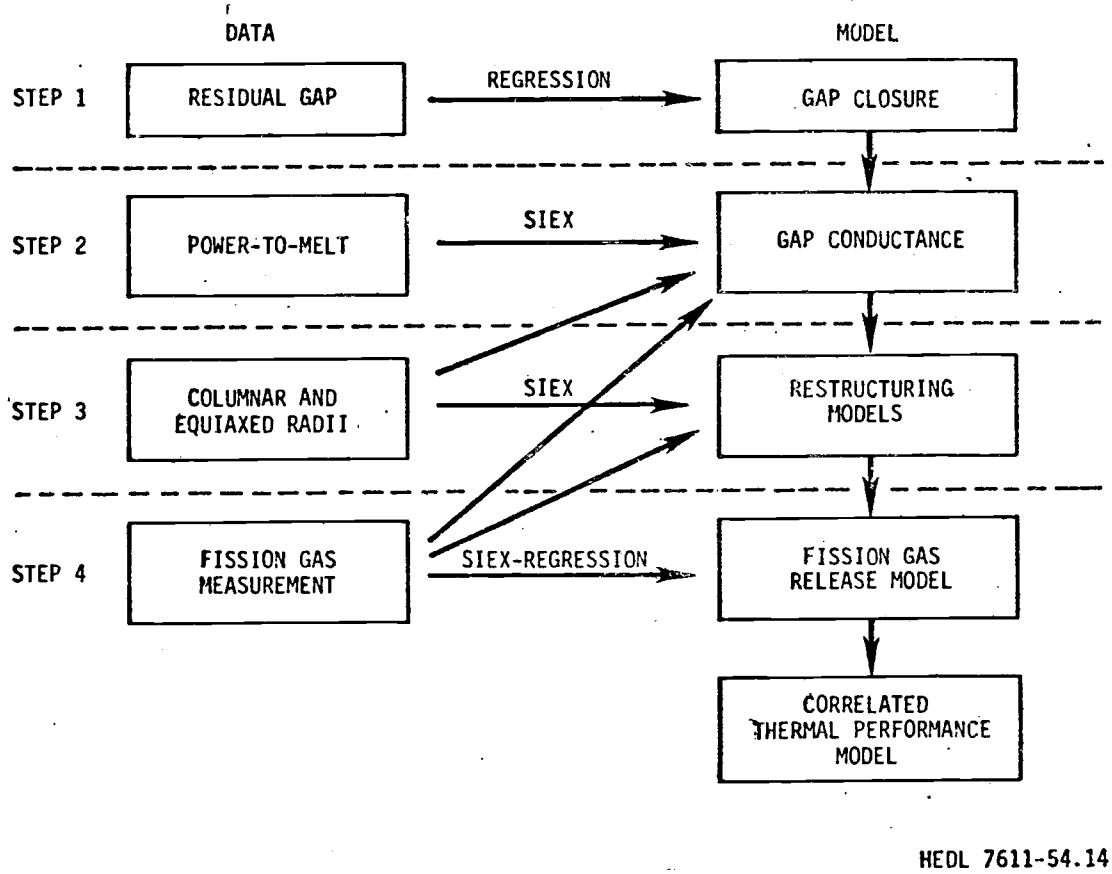

Figure 20. Data Interaction and Usage for SIEX Correlations.

In the following paragraphs some simplified models are suggested where possible, based on just the data from P-19 and P-20. Comments on trends and observations will be made on what models in the future should consider based on these two tests.

E.1 Residual Fuel-to-Cladding Gaps

Measurements of all residual fuel-to-cladding gaps, gaps observed at room temperature in transverse ceramography sections from the irradiated pins, were made in manner similar to that used in prior work[72] (see Tables IX and X, and Appendix C). It was judged for the purpose of calibrating gap conductance constants a model based only on P-19 and P-20 data should be used.

A series of computer plots of the gap closure data and, fabrication and operating parameters which could affect fuel-to-cladding gap closure were made. These parameters included:

- Local power
- Local fuel pellet density
- Local fuel burnup
- Local fuel-to-cladding gap size
- Local radius of melting
- Cladding ID size
- Irradiation history.

It is noted that the actual driving forces for closure of the fuel-to-cladding gap are probably fuel temperature, fuel temperature gradiant, fuel burnup (fission products) and power cycles. A method for direct

calculation of fuel temperatures and correlation of this data set of over 120 measurements (77 from pins from P-19 and P-20 Phase III, and 47 from sibling P-20 pins, Appendix C) is not available and would be complex. Hence, the development of a simplified model similar to the one used[72] in the past with the SIEX code. Here parameters related to the actual driving forces are considered (i.e. local pin power instead of fuel temperature).

Using the data plots as a guide and starting with the general SIEX gap closure equation used in the past, a series of correlations using the REEP[73] regression analysis computer code were made. Two equations were selected to represent the data. One for pins whose irradiation history included the 15% overpower, P-19 and Phase III of P-20, and the other for pins which operated only under steady state conditions, pins described in Appendix C. The final equation form for both was the same, only the fitting coefficients were changed:

$$(40)\quad G_p = G\{\, 1 - \tau[1 - \exp(-\Theta_3 \cdot N_c)] - [\Theta_4 - \tau][1 - \exp(-\Theta_5 \cdot Bu)]\} + Q_2' \Theta_6 / G$$

where: $\tau = \Theta_1 \cdot Q_1' \cdot (Q_1' - \Theta_2)$

Q_1' = Time average local linear heat rate, kW/ft (for "fresh" fuel $Q_1' = Q_2'$)

Q_2' = Maximum local linear heat rate, kW/ft

Bu = Local burnup, MWd/kgM

N_c = Number of full power cycles

G_p = Postirradiation diametral gap, mils

G = Fabricated diametral gap, mils

Θ's= Fitting coefficients, see Table XV for 15% overpower values.

Here τ is an estimate of thermal stress in the fuel. The first negative term in Equation 40 represents gap closure due to fuel cracking. The second negative term represents a thermal stress dependent swelling such as would be related to collection of fission gas in the fuel matrix. The final term, inversely dependent on original gap size, is to partially compensate for plastic strain of the fuel caused by differential thermal expansion of the fuel and cladding.

No consistant dependence could be identified with the variables of pellet density, cladding ID size, and melt extent. Figure 21 gives an indication of the "goodness of fit" of the model-equation derived for the overpower case. Included in Table XV is also the standard deviation of this model from the data. Considering the possible random variations in observed gap sizes because of random fuel cracking this is considered a very good representation of the data.

E.2 Fuel Thermal Expansion Model

In the past the thermal expansion (fraction of expansion $\Delta d/d$) of the fuel has been calculated in SIEX on a radial average basis. Thus

$$\frac{\Delta d}{d} = \frac{\int \Delta d/d \; r \; dr}{\int r \; dr} \quad .$$

Previous calibration efforts with SIEX using this method were never able to correlate both the measured residual fuel-to-cladding gap sizes from

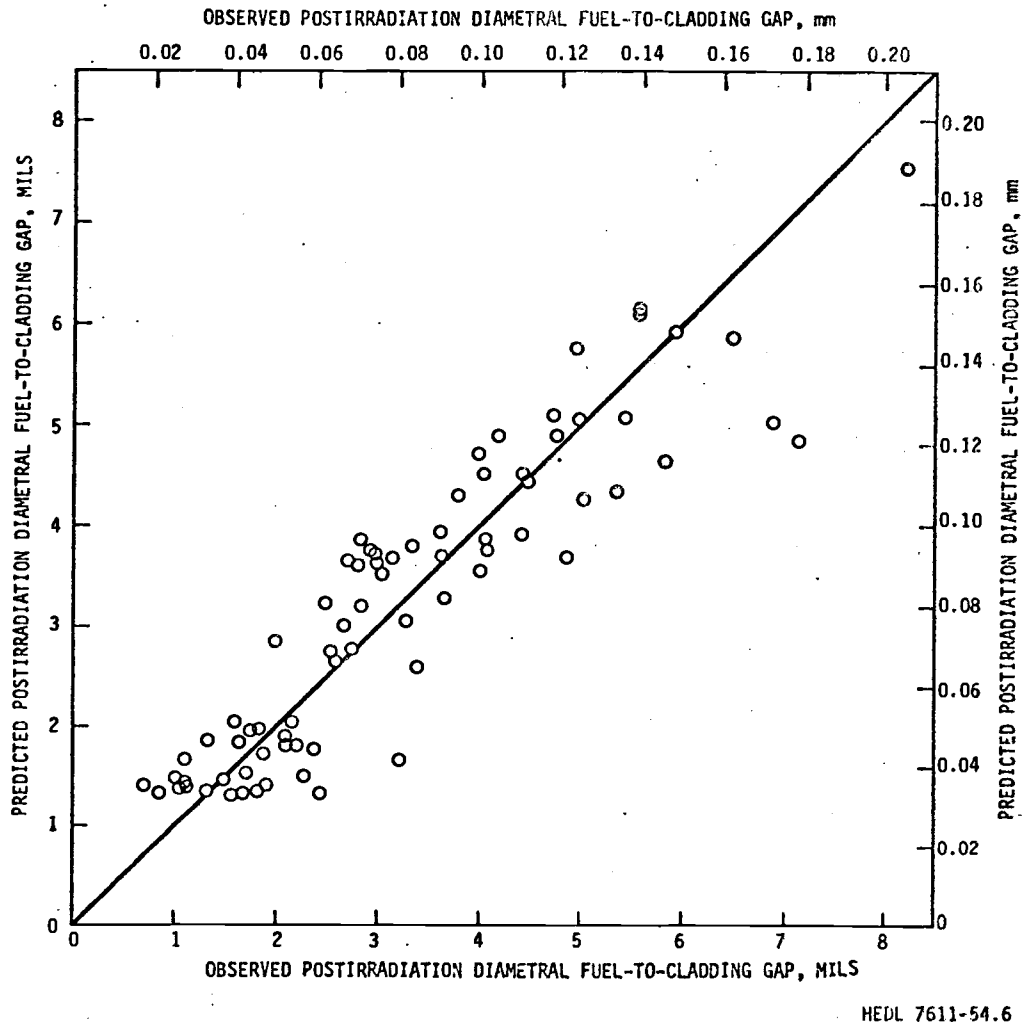

Figure 21. Residual Postirradiation Fuel-to-Cladding Gap Correlation.

TABLE XV

FITTING COEFFICIENTS FOR RESIDUAL FUEL-TO-CLADDING GAP MODEL
(FOR PINS THAT EXPERIENCED OVERPOWER CONDITIONS)

Number of Data Points	Standard Deviation	θ_1	θ_2	θ_3	θ_4	θ_5	θ_6
77	0.66	0.00672	12.5	0.919	0.890	7.11	0.239

the "fresh" fuel pins, and the apparent closure of the hot fuel-to-cladding gap in pins with fabricated diametral gap sizes less than 0.005 inch. This resulted in the inability to use the measured residual gap data for the "fresh" fuel pins.

Evidence of the fuel thermally expanding more than can be accounted for by this method for "fresh" fuel in P-19 and P-20, and the suggestions of G. L. Fox, of the Westinghouse Hanford Company, resulted in the adoption of a revised model. It is assumed here that the fuel has cracked and can expand radially similar to a bar. So:

(41) $\Delta d = \int \Delta d/d \, dr$

This results in the amount of thermal expansion (Δd) expected based on evidence of when the fuel is coming into contact with the cladding and allows the measured residual gap data to be used. It is noted this model is probably an over simplification of the complete mechanism (due to crack healing, etc.) however it appears reasonable to use for this study.

E.3 Fuel Absorbed Gas Release

For calibration of gap conductance the data from P-19 and P-20 on measured gas concentrations in the plenum were directly input. These were typically N_2 = 0.018 and Ar = 0.035 cc at STP for the fresh pins.

For other prediction purposes these low levels of N_2 and Ar gas are suggested, except when a gross concentration of either of the two are present in the fabricated fuel. There is suspicion that high concentrations of these gases, which have much lower thermal conductivity than

He, result in higher fuel temperatures. This would result from either the gas in the fuel matrix or in the fuel-to-cladding gap.

E.4 Fission Gas Release

Fission gas release from the fuel for calibration of the gap conductance model was based on the measured gas release found for each pin plenum during destructive examination. The P-19 data was discussed in Reference 3. The trend of the P-20 data is shown at the end of Appendix C.

A good fit to general data in the past has been made with fission gas release models[74] dependent on burnup and the sizes of fuel grain structure regions (i.e. columnar grain, equiaxed grain and unrestructured fuel). However, results of Appendix C indicate this would be reasonable only up to about 3000 MWd/MTM for fuel operating at high power. Beyond this the P-20 data shows an obvious switch in trend which is taken to indicate there is a strong instantaneous temperature dependence (note discussion in Appendix C on fuel temperatures with burnup). Based on this it is postulated that the gas release model should be dependent not only on fuel burnup and fuel grain region sizes but also instantaneous temperature.

E.5 Fuel Restructuring in the Columnar Grain Region

The columnar grain region size and apparent columnar density (based on a mass balance within the columnar grain region and the central void size) observed to form near the axial extents of melting were used to

analyze the data for the gap conductance work, see Sections B.2 and C.5.b. A simple columnar grain region model can use a columnar grain isotherm, T_{CG}, (above which the grains form) and a columnar grain density, ρ_{CG}. A value for T_{CG} based on P-19 and P-20 "fresh" fuel is:

(42) $T_{CG} = 2190°C$

At burnups above those of the "fresh" fuel (60 to 90 MWd/MTM) a model also dependent on temperature gradient (or local power) and perhaps other parameters is needed.

The apparent columnar grain density is dependent on several mechanisms as noted in Section C.5.b. Accounting only for densification of material present, past work with SIEX has used a constant value of ρ_{CG} of 98% TD. However some temperature gradiant dependence is apparent in the work with the "fresh" P-19 and P-20 data, with the small gap pins having an apparent lower columnar density than the larger gap pins. At higher burnups than the "fresh" fuel, observed central voids cannot be explained by just the movement of porosity from fabrication to the central void. A model[26] accounting for other mechanisms must be used and will be developed for SIEX in the future. The material in the grain region itself never appears, based on ceramography of the fuel, to densify beyond about 98.5% TD.

For comparing SIEX-M1 predictions to normalized data points, restructuring observed in the representative fuel ceramography was reproduced as nearly as possible by adjusting individual columnar grain temperatures, T_{CG}, and columnar grain densities. Thus no fuel restructuring modeling uncertainty is imposed on the comparisons.

F Calibration of the Gap Conductance Model

F.1 Summary of SIEX

The basic SIEX computer code has been used at HEDL for the past three years with very satisfactory results in predicting fuel performance[4]. SIEX is a code which calculates the thermal performance characteristics and dimensional changes (swelling and thermal expansion) of mixed-oxide fuel pins in a fast neutron environment. SIEX is comprised of a series of subroutines which model certain fast reactor fuels phenomena and is correlated to a significant amount of EBR-II irradiation test data. Program development and numerical techniques have been carried out in a way which provides a code with short running times and modular independence of models. This code has been shown to satisfy the need for a data analysis and design tool in the LMFBR program. The code is fully described in Reference 5 and is available through the Argonne National Computer Code Center.

The author was intimately involved in the calibration of this original code through collection of data (including measurement of fuel restructuring and residual fuel-to-cladding gaps, and derivation of preliminary Q'_m results from available P-19 data) and assisted in model definition and checkout. Since this time he has been actively involved in applying this code to LMFBR and FFTF fuel prediction studies.

The thermal performance formulations of the revised version, SIEX-M1, being used in this study have already been reviewed in Sections C, D and E. The changes from SIEX will be briefly noted in the following sections. The basic heat transfer expressions, Section C, are essentially unchanged from SIEX.

F.2 Revised Material Properties for SIEX-M1

Several material property expressions, discussed in Section D, were revised in going to the SIEX-M1 version of SIEX. In summary revised models were made for the calculation of:

- Accommodation coefficients and jump distance
- Thermal conductivity of the plenum gases Xe, Kr, N_2, Ar and He and their mixture.
- Fuel conductivity.

It is believed that the overall quality of the calculations have been improved significantly and are consistant with present data.

F.3 Revised Fuel Behavior Assumptions for SIEX-M1

The only models, discussed in Section E, used in the derivation of the gap conductance constants are the residual gap closure model and the fuel thermal expansion model. Both of these are revisions to prior SIEX models but are limited to the P-19 and P-20 data base.

F.4 Calibration Constants for Gap Conductants Model

The calibration of the fuel-to-cladding gap conductance model constants derived in Section C to the data discussed in Section B is the final step in developing the model. The measured Q'_m values from Section B are used directly, without normalization, in this portion of the analysis. Modified versions of SIEX-M1 were used to make these analyses.

The calibration of each of the three constants (see Equations 15 and 19) of the gap conductance model cannot be done independently with the test data developed in this study. For open gap cases only the constant B is applicable but once the fuel and cladding are in contact all three constants are used in the calculation. It is noted that as derived the constant B was only for the case of voids between contacting roughness however for application to a total gap conductance model it is being used as the correlating constant for all open gaps. Assuming a value of B can be correlated based on the open gap data at least one of the remaining two constants, A_2 or D, must be set based on judgement and past work by others.

F.4.a Gas Gap Constant "B"

When the fuel and cladding are not in contact the interface pressure is zero and the constant in Equation 18 becomes "B". The data from all the axial extents of melting were analyzed using a version of the SIEX-M1 code and the value of B needed to match the observed melting conditions was calculated. Table XVI summarizes these deduced values from the gap conductance model for the data. Figure 22 includes those data with calculated open hot gaps and the resulting values of B.

There is a significant amount of scatter in these values of B. However it must be remembered that all the experimental and fuel model uncertainty are now reflected in these values. No bias is observed for the different sized pins or between the P-20 and P-19 data. One way to

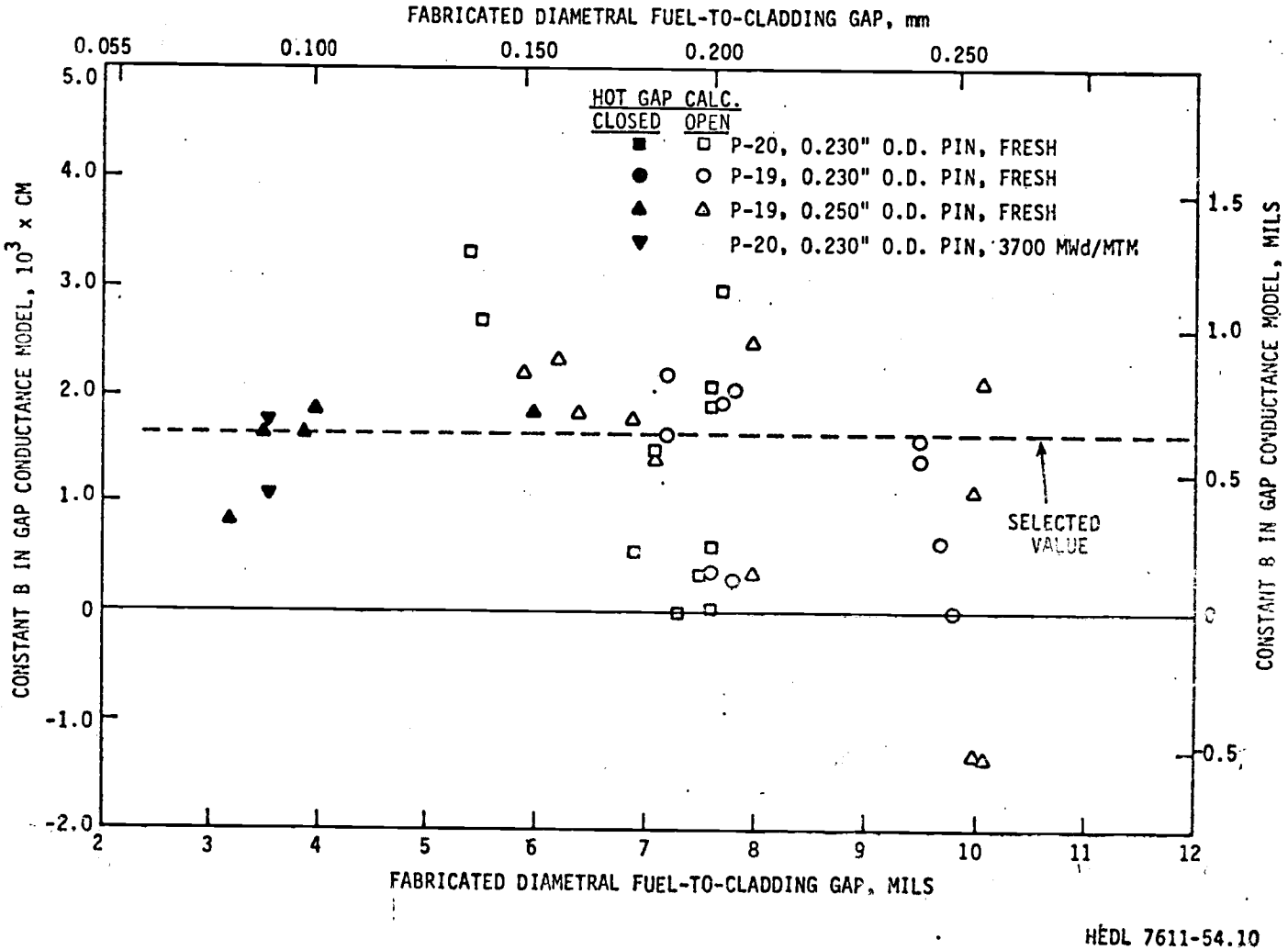

Figure 22. Calculated Values of Constant b from Test Data (Calculations for Closed Gap Data Assumed Constants A_2 = 100 and D = $-.2 \times 10^{-9}$).

TABLE XVI

CALCULATED VALUES OF GAP CONDUCTANCE PARAMETERS FOR DATA POINTS

Pin Section	Fabricated Diametral Gap, Mils	Hot Gap Radial, Mils	Gas Conductivity W/cm - °C	Jump Distance cm	Interface Pressure Dynes/cm²	H_G W/cm²-°C	H_S W/cm²-°C	H_R W/cm²-°C	Constant B cm
P-19-20 D	9.8	2.19	3.81×10^{-3}	7.78×10^{-4}	0.0	0.549	0.0	0.024	$.583\times10^{-3}$
None	9.7	1.87	3.65×10^{-3}	7.25×10^{-4}	0.0	0.644	0.0	0.021	$-.831\times10^{-4}$
P-19-8 D2	9.5	2.09	3.85×10^{-3}	7.92×10^{-4}	0.0	0.515	0.0	0.025	$.137\times10^{-2}$
A3	9.5	1.83	3.75×10^{-3}	7.57×10^{-4}	0.0	0.539	0.0	0.023	$.155\times10^{-2}$
P-19-13 D	7.8	1.33	3.64×10^{-3}	7.01×10^{-4}	0.0	0.844	0.0	0.019	$.239\times10^{-3}$
B	7.6	1.11	3.52×10^{-3}	6.65×10^{-4}	0.0	0.929	0.0	0.017	$.303\times10^{-3}$
P-19-2 E-2	7.8	1.32	3.79×10^{-3}	7.53×10^{-4}	0.0	0.623	0.0	0.023	$.198\times10^{-2}$
A-3	7.7	1.14	3.67×10^{-3}	7.13×10^{-4}	0.0	0.669	0.0	0.020	$.187\times10^{-2}$
P-19-35 F-1	7.2	0.98	3.66×10^{-3}	7.21×10^{-4}	0.0	0.762	0.0	0.021	$.158\times10^{-2}$
A-2	7.2	0.92	3.62×10^{-3}	7.09×10^{-4}	0.0	0.697	0.0	0.020	$.214\times10^{-2}$
P-19-3R C	10.0	1.88	3.79×10^{-3}	9.29×10^{-4}	0.0	0.562	0.0	0.025	$.106\times10^{-2}$
A	10.1	1.66	3.67×10^{-3}	8.14×10^{-4}	0.0	0.518	0.0	0.022	$.206\times10^{-2}$
P-19-24R C-3	10.0	2.26	3.64×10^{-3}	8.70×10^{-4}	0.0	0.696	0.0	0.021	$-.137\times10^{-2}$
A-2	10.1	1.87	3.41×10^{-3}	7.82×10^{-4}	0.0	0.826	0.0	0.016	$-.139\times10^{-2}$
P-19-25R E-1	8.0	1.05	3.74×10^{-3}	9.04×10^{-4}	0.0	0.625	0.0	0.024	$.243\times10^{-2}$
A-3	8.0	0.93	3.36×10^{-3}	7.60×10^{-4}	0.0	0.976	0.0	0.016	$.313\times10^{-3}$
P-19-30 E-2	7.1	0.59	3.57×10^{-3}	8.36×10^{-4}	0.0	0.965	0.0	0.019	$.135\times10^{-2}$
A-2	6.9	0.42	3.39×10^{-3}	7.72×10^{-4}	0.0	0.954	0.0	0.016	$.173\times10^{-2}$
P-19-7R D	6.4	0.36	3.62×10^{-3}	8.09×10^{-4}	0.0	1.027	0.0	0.019	$.179\times10^{-2}$
B	6.2	0.04	3.44×10^{-3}	7.47×10^{-4}	0.0	1.104	0.0	0.015	$.228\times10^{-2}$
P-19-26R G-2	5.9	0.01	3.58×10^{-3}	7.94×10^{-4}	0.0	1.222	0.0	0.018	$.212\times10^{-2}$
A-2	6.0	0.0	3.38×10^{-3}	7.25×10^{-4}	1.73×10^{8}	1.201	0.0	0.015	$.217\times10^{-2}$

TABLE XVI (Cont'd)

CALCULATED VALUES OF GAP CONDUCTANCE PARAMETERS FOR DATA POINTS

Pin Section		Fabricated Diametral Gap, Mils	Hot Gap Radial Mils	Gas Conductivity W/cm - °C	Jump Distance cm	Interface Pressure Dynes/cm^2	H_G W/cm^2-°C	H_S W/cm^2-°C	H_R W/cm^2-°C	Constant B cm
P-19-27R	H-1	4.0	0.0	3.41×10^{-3}	7.35×10^{-4}	5.77×10^{8}	1.420	0.728	0.015	$.187\times10^{-2}$
	A-2	3.9	0.0	3.25×10^{-3}	6.83×10^{-4}	6.53×10^{8}	1.525	0.747	0.013	$.166\times10^{-2}$
P-19-28	H-2	3.5	0.0	3.40×10^{-3}	7.26×10^{-4}	5.03×10^{8}	1.537	0.642	0.015	$.164\times10^{-2}$
	A-3	3.2	0.0	3.21×10^{-3}	6.61×10^{-4}	6.44×10^{8}	2.294	0.761	0.012	$.839\times10^{-3}$
P-20-7	H	7.5	1.39	3.90×10^{-3}	7.84×10^{-4}	0.0	0.636	0.0	0.027	$.183\times10^{-2}$
	A-1	7.5	1.13	3.69×10^{-3}	7.15×10^{-4}	0.0	0.568	0.0	0.022	$.292\times10^{-2}$
P-20-13	J	7.3	1.51	2.50×10^{-3}	1.07×10^{-3}	0.0	0.520	0.0	0.029	$-.909\times10^{-4}$
	A-1	7.5	1.17	2.29×10^{-3}	9.27×10^{-4}	0.0	0.545	0.0	0.022	$.297\times10^{-3}$
P-20-39	G	7.55	1.12	3.78×10^{-3}	8.92×10^{-4}	0.0	0.863	0.0	0.023	$.647\times10^{-3}$
	B	7.65	0.93	3.64×10^{-3}	8.37×10^{-4}	0.0	0.719	0.0	0.021	$.187\times10^{-2}$
P20/P19-34	G	6.95	0.93	3.83×10^{-3}	7.23×10^{-4}	0.0	0.849	0.0	0.024	$.144\times10^{-2}$
	B	7.05	0.86	3.60×10^{-3}	6.54×10^{-4}	0.0	0.760	0.0	0.019	$.188\times10^{-2}$
P20/P19-21	G	7.50	1.45	3.76×10^{-3}	7.14×10^{-4}	0.0	0.856	0.0	0.023	$-.412\times10^{-5}$
	B	7.45	0.98	3.61×10^{-3}	6.67×10^{-4}	0.0	0.697	0.0	0.020	$.203\times10^{-2}$
P-20-30	H	5.45	0.48	3.83×10^{-3}	7.27×10^{-4}	0.0	0.838	0.0	0.024	$.264\times10^{-2}$
	C-4	5.35	0.22	3.60×10^{-3}	6.54×10^{-4}	0.0	0.792	0.0	0.019	$.334\times10^{-2}$
P-20-33	F	3.55	0.0	1.90×10^{-3}	6.50×10^{-4}	5.51×10^{8}	1.146	0.665	0.018	$.113\times10^{-2}$
	C-1	3.55	0.0	1.89×10^{-3}	6.43×10^{-4}	5.96×10^{8}	0.848	0.658	0.018	$.179\times10^{-2}$

1 mil = mm

1 W/cm^2 - °C = 1762 BTU/ft^2-hr-°F

look at this plot is that the lower values of B are calculated when a smaller effective hot gap value is needed to explain the gap conductance required to match the data, see Equation 19.

A somewhat conservative, with respect to Q'_m, value of 1.65×10^{-3} cm was chosen for B. More weight was given to fitting the data near the closed hot gap values (except for the data from the "fresh" P-20 pin with the 0.0055 inch gap) and being conservative at larger gaps. There does appear to be a slight trend to the plot increasing with decreasing gap size, however the constant value, considering the uncertainties involved, was deemed sufficient for the characterization.

F.4.b Contact Constants A_2 and D from Closed Gap Data

Assuming the constant B to be now fixed the constants A_2 and D must be set based on the data from pins with calculated closed fuel-to-cladding gaps. The data from the P-19 and P-20 experiments does not allow the separation of these constants to be solved for uniquely. Laboratory experiments can overcome this by doing part of the tests in vacuum thus eliminating any heat transfer through the gas allowing a constant like A_2 to be calibrated. For this calibration work we chose to set the constant D equal to -0.2×10^{-9} cm^2/Dyne based on results of Ross and Stoute, past work by Dutt with SIEX and the physical meaning of the constant. It is expected since this constant seeks to model the decrease in "waviness" of the softer surface material under pressure that the effect would be less than that found for Zr - UO_2 pairs by Ross and Stoute. The yield point of the stainless steel (about 72 ksi at 950°F) is higher than that of zircaloy (about 10 ksi at 950°F).

The constant A_2 in the solid-to-solid heat conductance expression representing the inverse of the average radius of the a-spots, Equation 15, was then correlated based on the data with calculated closed hot gaps. The same version of SIEX-M1 was used and the agreement of the calculated constant B for these cases, to the value previously set, 1.65 x 10^{-3} cm, was itterated on while A_2 was adjusted until the best fit was obtained. The final value of A_2 resulting from this analysis was 100 cm^{-1} . Figure 22 gives an indication of the final agreement of calculated "B" values using A_2 = 100 cm^{-1} and D = -.02 x 10^{-9} cm^2/Dyne.

F.5 Discussion

Figure 23 shows the agreement of the temperature drops, across the fuel-to-cladding gaps, predicted by the calibrated model and those calculated directly from the test data. Predicted values are somewhat conservative but in general agree well with the observed calculated values. Figures 24 and 25 indicate the agreement of the normalized Q'_m data from Section B with the predictions using the calibrated gap conductance model is also, in general, very good. Note that the fuel restructuring was handled as described in Section E.5.

The trend of predicted lower Q'_m values with increasing burnup, Figure 25, for pins with small fabricated fuel-to-cladding gaps (0.0035 inch diametral), is not reflected by the limited data. While the disagreement of the predictions with what little data there is at this point, is well within the test uncertainties, this type behavior may be real, rather than the decreasing trend predicted. It could be caused by two burnup dependent phenomena not considered in this analysis, 1) the

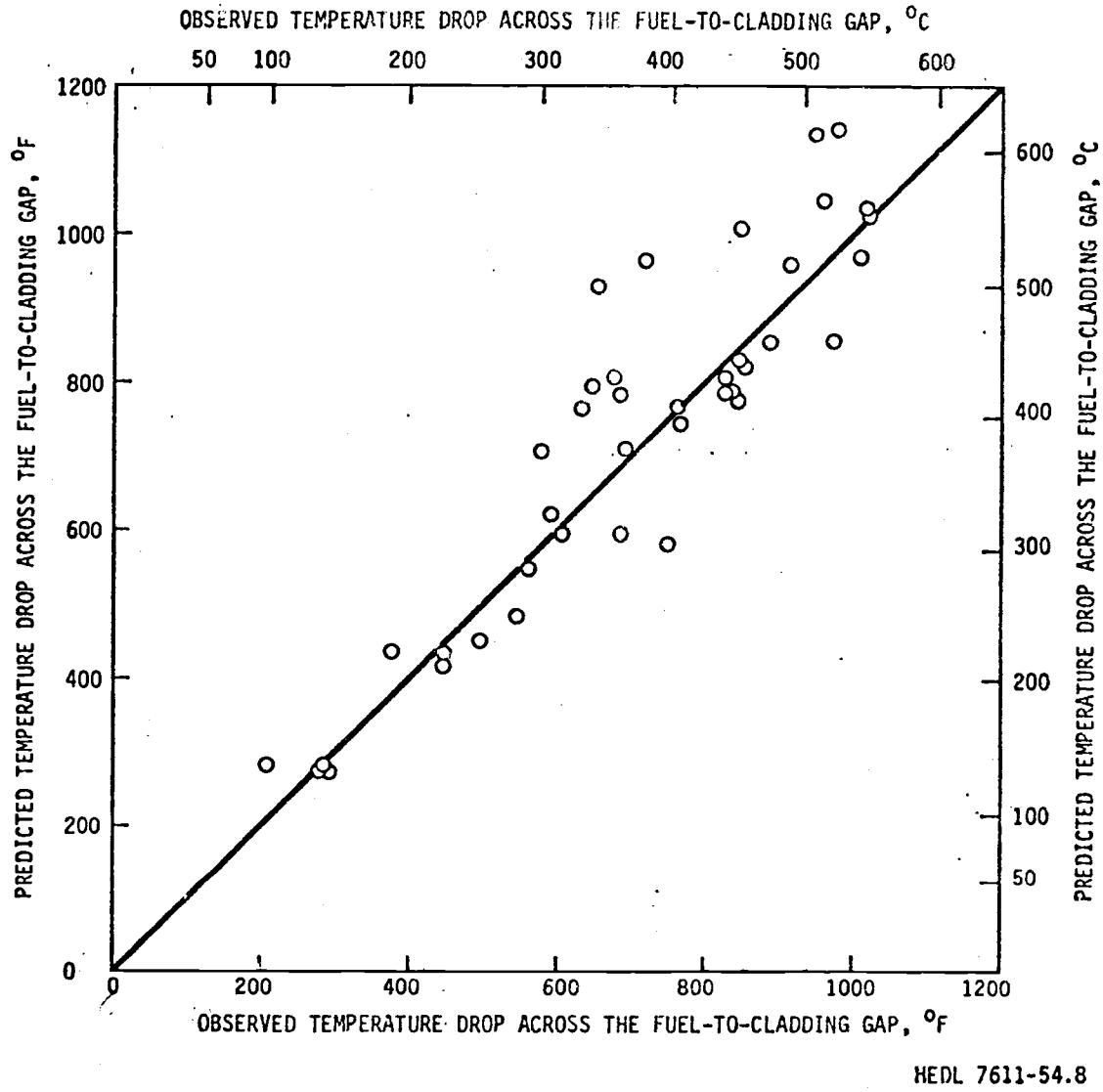

Figure 23. Comparison of Predicted and Calculated Temperature Drops Across the Fuel-to-Cladding Gaps.

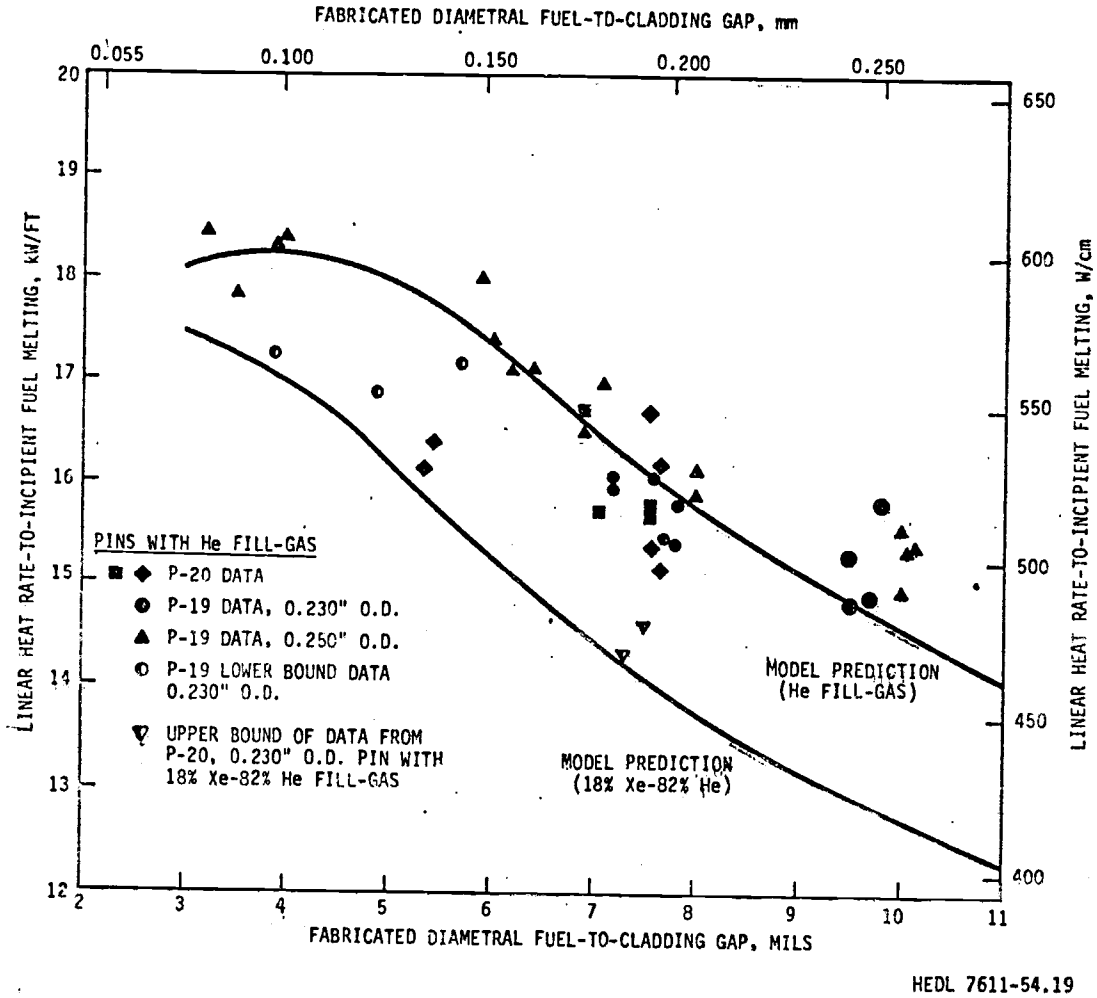

Figure 24. Comparison of Normalized Q'_m Data and Predictions for "Fresh" Fuel.

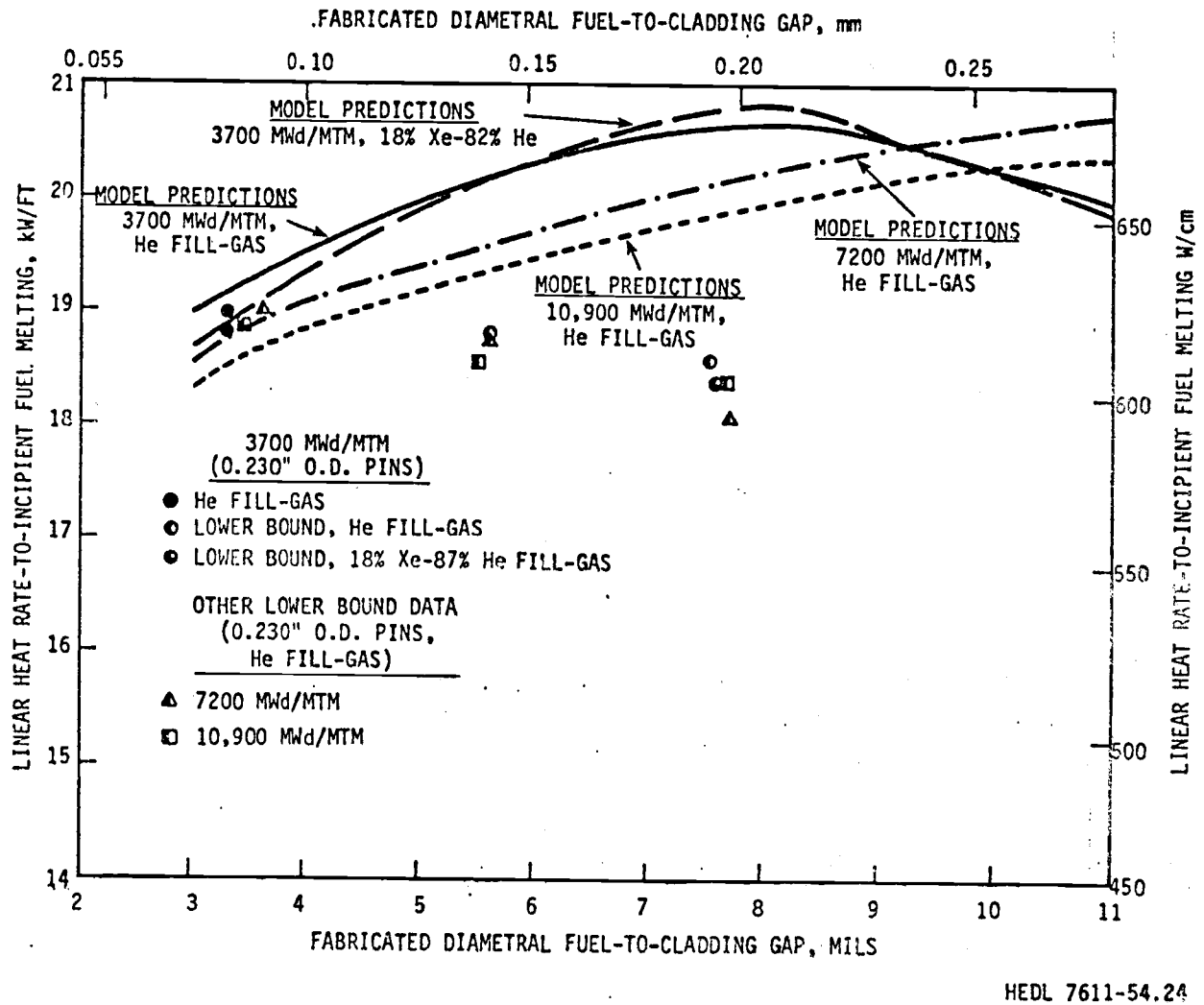

Figure 25. Comparison of Normalized Q'_m Data and Predictions for Preirradiated Fuel.

creep of the contacting roughness asperities (causing greater solid-to-solid heat transfer) and 2) the buildup of solid fission products between the contacting roughness asperities where heat is assumed transferred through the gas alone. The data from these tests are insufficient to characterize this type behavior. Application of this calibrated gap conductance model to burnups higher than 10,000 MWd/MTM may require further evaluation of these mechanisms to assure temperature drops across the gaps are not over predicted resulting in too low Q'_m values being calculated.

For comparison Figure 26 shows the previous normalized[1] P-19 data, "fresh" pins, and the agreement of the original version of SIEX[5] with those. In general there is less data scatter and improved prediction versus data agreement with the present analysis.

Table XVII gives some example breakdowns of the conductance values being summed in the model to give the total gap conductance predicted. Figure 27 indicates the predicted change in total gap conductance with fabricated gap at different burnup levels.

Some comparison of the derived constants with out of reactor laboratory results is warrented even though the roughness values for the surfaces of the materials here were not measured. Values from Ross and Stoute's work are compared here using the roughness assumptions from Section D and assuming Myer's hardness of the cladding is equal to one-third the yield strength[6]:

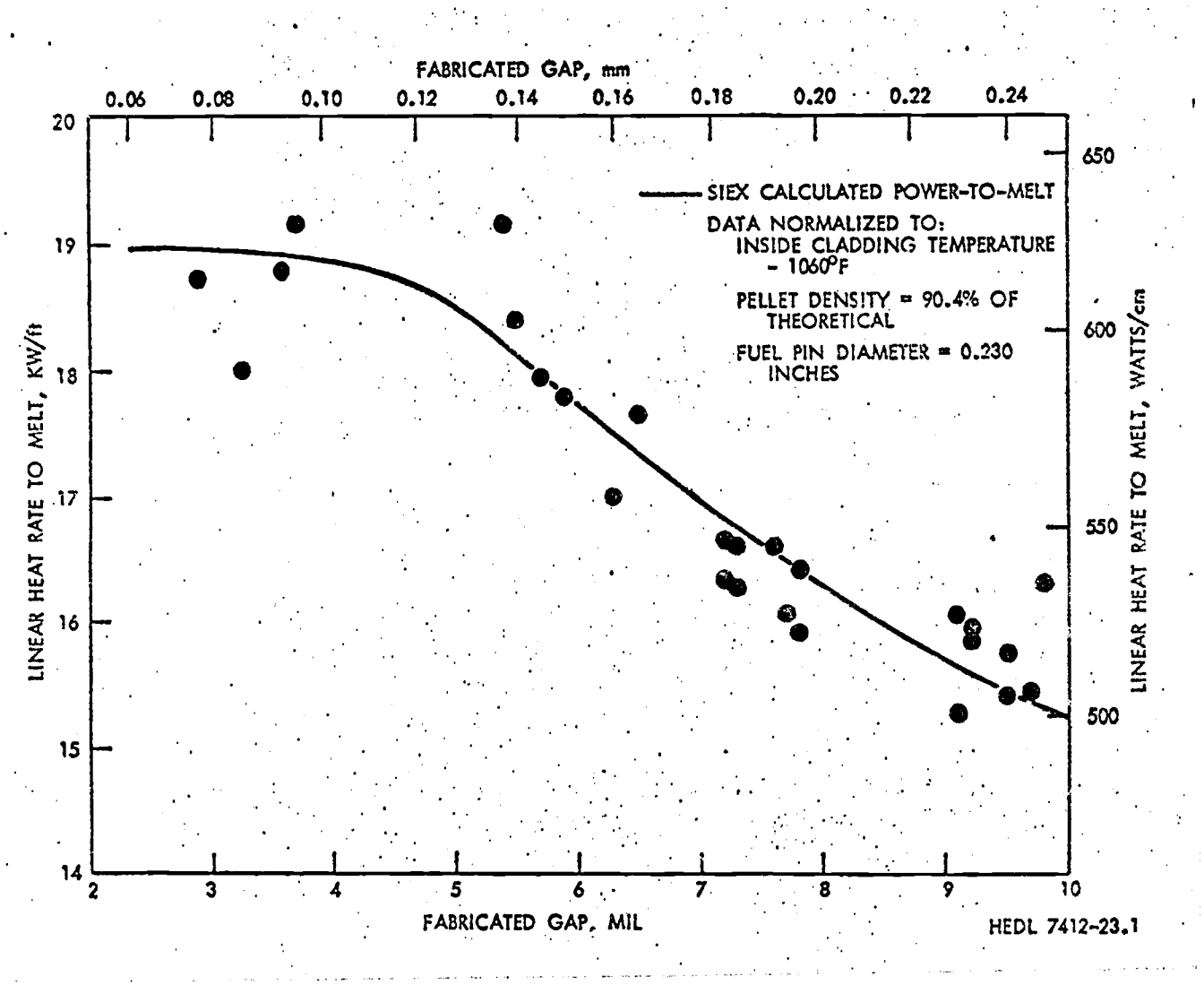

Figure 26. Prediction of Original SIEX Code with Preliminary Analysis of P-19 Data.

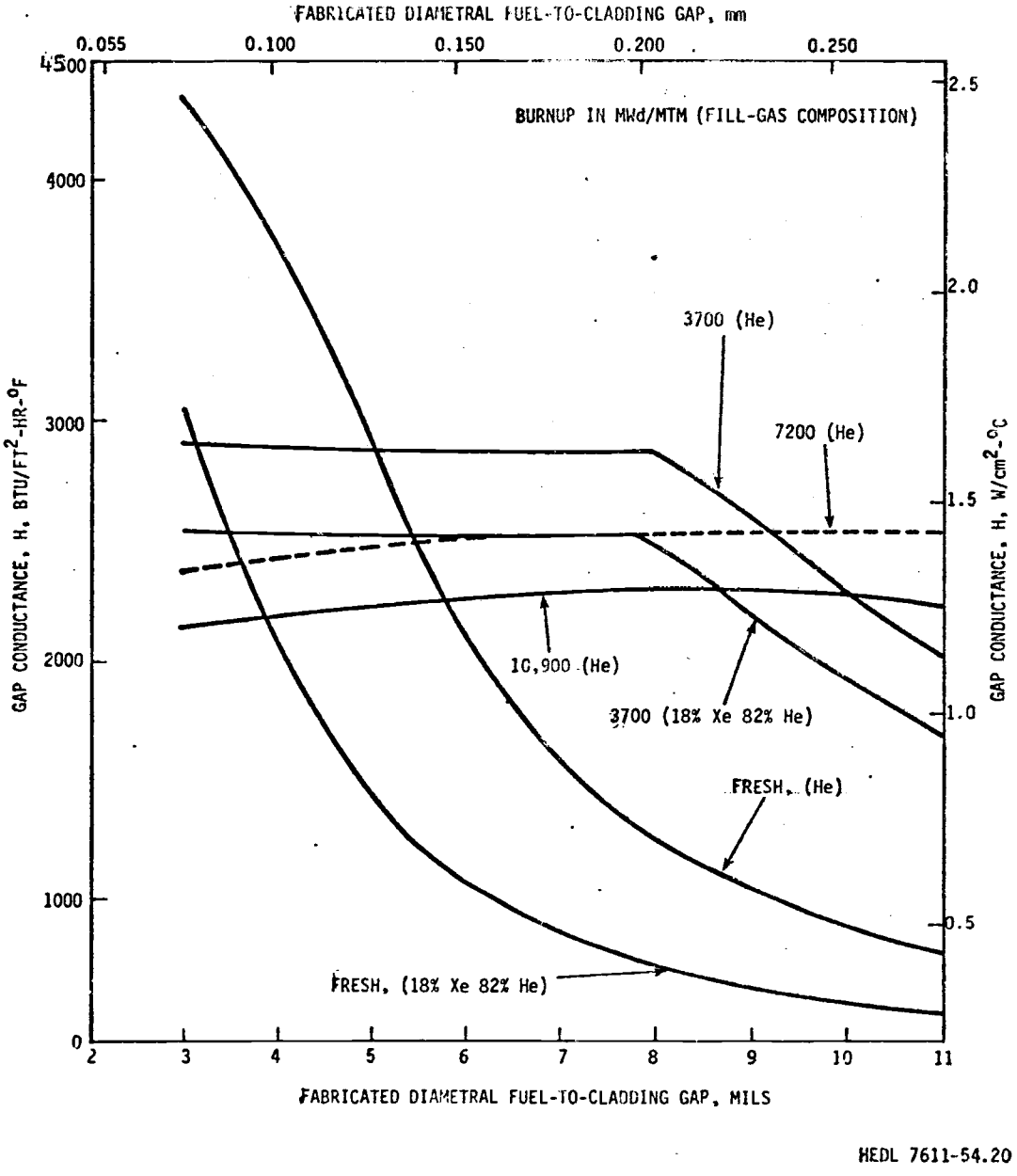

Figure 27. Behavior of Calibrated Gap Conductance Model Predictions with Burnup.

TABLE XVII

CONTRIBUTIONS TO THE TOTAL GAP CONDUCTANCE PREDICTED BY THE CALIBRATED MODEL

Burnup MWd/MTM	Percent Xe In Fill Gas	Fabricated Diametral Fuel-to-Cladding Gap, mils	Calculated Hot Diametral Fuel-to-Cladding Gap, mils	H_G $\frac{W}{cm^2 - °C}$	H_G $\frac{BTU}{ft^2-Hr-°F}$	H_S $\frac{W}{cm^2 - °C}$	H_S $\frac{BTU}{ft^2-Hr-°F}$	H_R $\frac{W}{cm^2 - °C}$	H_R $\frac{BTU}{ft^2-Hr-°F}$
~ 0.0	0.0	4.0	0.0	1.599	2820.	0.516	910.	0.0137	24.
0.0	0.0	5.5	0.2	1.367	2410.	0.0	0.0	0.0157	28.
0.0	0.0	8.0	2.54	0.666	1170.	0.0	0.0	0.0216	38.
~ 0.0	18.0	4.0	0.0	0.903	1590.	0.26	460.	0.0166	29.
0.0	18.0	5.5	0.76	0.661	1160.	0.0	0.0	0.0218	38.
0.0	18.0	8.0	3.24	0.372	655.	0.0	0.0	0.0303	53.
3700	0.0	4.0	0.0	0.866	1530.	0.756	1330	0.0155	27.
3700	0.0	5.5	0.0	0.870	1530.	0.751	1320	0.0157	28.
3700	0.0	8.0	0.0	0.864	1520	0.746	1310	0.0158	28.
3700	18.0	4.0	0.0	0.680	1200.	0.737	1300.	0.0164	29.
3700	18.0	5.5	0.0	0.688	1210.	0.732	1290.	0.0166	29.
3700	18.0	8.0	0.0	0.688	1210.	0.714	1260.	0.0169	30.
7200	0.0	4.0	0.0	0.618	1090.	0.732	1290.	0.0166	29.
7200	0.0	5.5	0.0	0.671	1180.	0.733	1290.	0.0165	29.
7200	0.0	8.0	0.0	0.691	1220.	0.730	1290.	0.0166	29.
10900	0.0	4.0	0.0	0.504	890.	0.716	1260.	0.0173	30.
10900	0.0	5.5	0.0	0.546	960.	0.717	1260.	0.0173	30.
10900	0.0	8.0	0.0	0.570	1000.	0.715	1260.	0.0174	31

	Dynes/cm^2	Ross and Stoute (UO_2 - Zr pairs)	This Study (PuO_2 - UO_2 Stainless Steel)
C_1 (= B[EXP(D·P)]),	P = 9.8×10^7	2.5	3.2
(Equation 18)	P = 4.9×10^8	1.5	2.9
A_1		0.5	1.84
(Equation 15)			

Horn[6] found, apparently fitting data from Ross and Stoute, a value for the constant D of -1.26×10^{-9} (P in Dynes/cm^2) compared to this study's value of -0.2×10^{-9}. As noted previously the lower values of D selected is reasonable with the difference in material pairs.

Because of the range of roughnesses that are possible comparison of the constants independent of roughness (i.e. A_1 and C_1) could vary significantly. However it is to be noted that all the fuels used in these tests were fabricated with methods typical of those used in commercially made LMFBR fuel and thus should be representative and directly applicable to them. In the near future it is recommended that archive fuel samples from these tests be characterized for roughness. This should allow direct comparisons with laboratory results to be made.

G Conclusions

G.1 Power-to-Incipient Melting, Q'_m Data Analysis

Figure 11 illustrates the conclusions that can be drawn from the "fresh" pin data from HEDL P-19 and P-20. With fresh fuel (60 to 90 MWd/MTM) there is a definite dependence of Q'_m on fabricated fuel-to-cladding gap size. The data show a decrease in Q'_m values as the fuel-to-cladding diametral gap increases beyond 0.005 inch (0.13 mm) which is concluded to be due to the fuel and cladding coming out of contact and the heat being transferred only through a gas gap. Normalized Q'_m values ranged from about 18.5 kW/ft (606 W/cm) to 14.5 kW/ft (475 W/cm) over the diametral fuel-to-cladding gap range from 0.003 to 0.010 inch (0.08 to 0.254 mm).

The primary conclusion that can be drawn from the higher burnup data based on this analysis is illustrated in Figure 12. By the time 3700 MWd/MTM is reached the linear heat-rating-to-melting, Q'_m, is at least 18.5 kW/ft and is independent of starting gap size. This is at least a 20% relative improvement over the results found for the "fresh" pins fabricated with pure He fill gas, at a diametral gap of 0.0075 inch (0.13 mm). The improvement in Q'_m observed for the 18% Xenon gas tagged pin was over 25%, from under 15.3 kW/ft (501 W/cm) "fresh" to over 18.3 kW/ft (600 W/cm) at 3700 MWd/MTM. The primary reason for this improvement in thermal performance is early fuel-to-cladding gap closure. This eliminates the initial fabricated fuel-to-cladding gap, in the range tested, as a major variable affecting Q'_m after a small burnup is accumulated.

These test results verify previous less refined analyses and have significant implications about the performance predictions for FFTF/LMFBR type fuel. The higher burnup data indicate that with a short conditioning period (less than 12 full power days or 3700 MWd/MTM) thermal rating of a LMFBR could be increased by 20%. Further, if this mode of operation is used restrictive limits on maximum fabricated gap size can be relaxed. This may allow sintered-to-size fuel pellets to be used, thus allowing more economical fuel fabrication.

G.2 Characterization of the Radial Heat Transfer Path

Analyses of the total radial heat transfer path were made and "best values" developed for calculating temperatures consistant with the present "state of the art" data. A set of recommended heat transfer formulations, similar to those used in SIEX[5], were put forth in Section C for the radial heat path from the coolant to the center of the fuel. Further a set of material properties to be used with these heat transfer formulations were developed and/or described in Section D. This heat transfer system was incorporated into a revised version of the SIEX code, SIEX-M1, to develop a gap conductance model based on the P-19 and P-20 integral Q'_m data.

G.3 Hot Fuel-to-Cladding Gap

The permanent closure of the fuel-to-cladding gaps were measured from ceramography sections from HEDL P-19 and P-20. A mathematic model was correlated to this closure data using original gap size, local heat rate, reactor cycles, local fuel burnup and power history. This model, for the pins from P-19 and P-20 Phase III, is described by Equation 40 and Table XV. It represents the data reasonably well (standard devia-

tion of 0.66 and a percent variation explained of 86) considering the inherent variation in this type of data. This model seeks to account for permanent fuel deformation due to cracking, fission product build up and fuel-cladding inaction.

The best representation to use for fuel thermal expansion was concluded to be the summation of radial thermal expansion rather than that based on a radial average temperature.

G.4 Calibration of the Fuel-to-Cladding Gap Conductance Model

Using Q'_m data (not normalized) from HEDL P-19 and P-20 tests, the heat transfer models and formulations developed, and the models for calculating hot fuel-to-cladding gaps the three constants in the gap conductance model, (Equations 15 and 19) based on work by Ross and Stoute, were calibrated. Since constants A_2 and D could not be calibrated indendently, results from other work was also used.

The values derived for the constants were:

$$A_2 = 100 \text{ cm}^{-1}$$

$$B = 1.65 \times 10^{-3} \text{ cm}$$

$$D = -.2 \times 10^{-9} \text{ cm}^2/\text{Dyne}$$

The predictions of the calibrated model agree well with the data from the in-reactor tests, Figures 23, 24, and 25, and should result in a refined (least uncertainty) method of calculating gap conductances.

G.5 Recommendations for Future Work

It was concluded to be of the most benefit, in the future archive samples from the P-19 and P-20 tests should be characterized for surface

roughness. This will allow the constants independent of roughness to be calculated and compared to past laboratory results. It will also allow verification of uniformity of surface condition of the different fuel batches used in both tests.

BIBLIOGRAPHY

1. R. D. Leggett, R. B. Baker, E. O. Ballard, G. R. Horn and D. S. Dutt , "Linear Heat Rating for Incipient Fuel Melting in UO_2-PuO_2," Trans. Amer. Nucl. Soc., Volume 15, No. 2, page 752, 1972.

2. R. D. Leggett, R. B. Baker, D. S. Dutt, and S. A. Chastain, "Influence of Burnup on Heat-Rating to Melting for UO_2-PuO_2 Fuel," Trans. Amer. Nucl. Soc., Volume 19, October 1974, page 137.

3. "Interim Status Report on Thermal Performance of LMFBR Oxide Fuel HEDL P-19," Compiled by R. D. Leggett, HEDL TME-71-92, June 1971.

4. R. B. Baker, R. D. Leggett and D. S. Dutt, "Interim Report: Effect of Burnup on Heat-Rating-to-Incipient Fuel Melting HEDL P-20," HEDL TME-75-63, UC-79b.

5 D. S. Dutt and R. B. Baker, "A Correlated Code for the Prediction of Liquid Metal Fast Breeder Reactor (LMFBR) Fuel Thermal Performance," HEDL TME-74-55, June 1975.

6. G. R. Horn and F. E. Panisko, "User's Guide for GAPCON: A Computer Program to Predict Fuel-to-Cladding Heat Transfer Coefficients in Oxide Fuel Pins," HEDL TME-72-128, September 1972.

7. A. M. Ross and R. D. Stoute, "Heat Transfer Coefficient Between UO_2 and Zercaloy 2," AECL-1552, June 1962.

8. Richard A. Dean, "Thermal Contact Conductance," Thesis for Masters' Degree Program, University of Pittsburgh, 1963.

9. A. C. Rapeir, T. M. Jones, and J. E. McIntosh, "The Thermal Conductance of Uranium Dioxide/Stainless Steel Interfaces," Intern. J. Heat Mass Transfer, 6, 397, 1963.

10. T. N. Cetinkale and M. Fishender, "Thermal Conductance of Metal Surfaces in Contact," Proc. of the Gen. Discussion on Heat Transfer, Institution of Mechanical Engineers and ASME, September 1951.

11. M. G. Cooper, B. B. Mikic, and M. M. Lovanich, Intern. J. Heat Mass. Transfer, 12, 279-300, 1969.

12. G. Jacobs and N. Todreas, "Thermal Contact Conductance in Reactor Fuel Elements," Nuclear Sci. and Engineer, 50, 283-306, 1973.

13. D. D. Lanning and C. R. Hann, "Review of Methods Applicable to the Calculation of Gap Conductance in Zercaloy - Clad UO_2 Fuel Rods," BNWL-1894, April, 1975.

14. S. McLain and J. H. Martens, Eds., "Reactor Handbook," Volume IV, 2nd Edition, p. 210, Interscience Publishers, New York.

15. F. R. Campbell, R. Des Haies, "The Effect of Gas Pressure on Fuel/Sheath Heat Transfer," Trans. Amer. Nucl. Soc., Volume 21, page 380.

16. R. Holm, "Electrical Contacts," Stockholm, Almquist and Wakrells, 1946, p. 398.

17. A. J. W. Moore, "Deformation of Metals in Static and Sliding Contact," Proc. Roy. Soc., A, 195, 231-246, 1948.

18. H. S. Carslaw and J. C. Jaeger, "Conductance of Heat in Solids," Oxford, 2nd Edition, 1959.

19. Ascoli and E. Germagnoli, "On the Thermal Resistance Between Metal Surfaces in Contact," Energia Nucleare, 3, (2), 113-118, 1956.

20. E. H. Kennard, "Kenetic Theory of Gases," New York, McGraw Hill, 1938.

21. A. J. Chapman, "Heat Transfer," McMillan Co., New York, NY, 617 pp, 1967.

22. R. B. Bird, W. E. Stewart, and E. N. Lightfoot, "Transport Phenomena," John Wiley and Sons, New York, N. Y., 1960.

23. C. M. Cox, F. J. Homan, R. L. Diamond, "LMFBR Fuel Cycle Progress Report," ORNL-TM-3759, February, 1972.

24. K. R. Merkx and G. L. Fox, "SINTER - A Program for Calculating Radial Temperature Distributions in Oxide Fuel Pins Undergoing Sintering," BNWL-1241, UC-80, January, 1970.

25. F. A. Nichols, "Behavior of Gaseous Fission Products in Oxide Fuel Elements" Bettis Atomic Power Laboratory, Pittsburgh, PA., WAPD-TM-570, 1966.

26. R. D. Leggett, R. B. Baker, D. S. Dutt and L. A. Pember, "Central Void Size in Irradiated Mixed-Oxide Fuel Pins," Trans. Amer. Nucl. Soc., Volume 17, page 173, November 1973.

27. M. Knudsen, "The Kinetic Theory of Gases," New York, John Wiley and Sons, Inc. 1946.

28. E. H. Kennard, "Kinetic Theory of Gases," New York, McGraw Hill, 1938.

29. J. H. Jeans, "Kinetic Theory of Gases," Cambridge, University Press, 1940.

30. R. Godesar et al, "COMETHE-II-A Computer Code for Predicting the Mechanical and Thermal Behavior of a Fuel Pin," Nuclear App. and Tech., Vol. 9, August 1970.

31. S. Giuliani and C. Mustacchi, "Heat Transfer in a Fuel Element Gas Gap," European Atomic Energy Community, Joint Nuclear Research Center, Ispra, Italy, 1964, EUR-521-E, UC-80.

32. S. Dushman, "Scientific Foundations of Vacuum Technique," John Wiley and Sons, Inc., New York, 1958.

33. H. Mikami, Y. Endo and Y. Takahima, "Heat Transfer from a Sphere to Rarefied Gas Mixtures," Int. J. Heat Transfer, Vol. 9, p. 1435-1448, Pargamon Press, 1966.

34. A. Boltax, and J. H. Saling, "Oxide Fuel Element Quarterly Progress Report for Period Ending December 31, 1974," WARD-OX-3045-16, UC-796.

35. A. Ullman, R. Acharya and D. R. Olander, "Thermal Accommodation Coefficients of Inert Gases on Stainless Steel and UO_2," Journal of Nuclear Materials 51, (1974), 277-279.

36. Leon Trilling, "The Interaction of Monotomic Inert Gas Molecules with a Continuous Elastic Solid," Surface Science, 21 (1970) p. 337-365.

37. R. B. Bird, W. E. Stewart, and E. N. Lightfoot, "Transport Phenomena," John Wiley and Sons, New York, N. Y., 1960.

38. W. R. Lloyd, D. P. Wilkins and P. R. Hill, "Heat Transfer in Multicomponent Monotomic Gases in Low, Intermediate and High Pressure Regine," IEEE Thermoionic Conversion Specialist Conference, 7th Framingham, Mass., 1968.

39. "LMFBR Fuel Cycle Studies Progress Report," No., 36, ORNL-TM-3759, February 1972.

40. "Purdue University Thermophysical Properties Research Center Data Book," Vol. 2, Chapter 1, December 1966.

41. R. W. Powell, C. Y. Ho and P. E. Liley, "Thermal Conductivity of Selected Materials, National Standard Reference Data Series - National Bureau of Standards - 8, (Category 5 - Thermodynamic and Transport Properties)," November 25, 1966.

42. P. E. Liley, "Thermal Conductivity of 46 Gases at Atmospheric Pressure." Proc. Fourth Symposium on Thermophysical Properties, College Park, MD, J. R. Mogyski, Ed., ASME. April 1968.

43. J. H. Dymond, "High Temperature Transport Coefficients for Rare Gases Neon to Xenon," J. Phys. B: Atom. Molec. Phys., Vol. 4, 1971.

44. G. V. Massey, "The Thermal Properties of Gases for Use in Reactor Heat-Transfer Calculations," United Kingdom Atomic Energy Authority Development and Engineering Group, Downery, Carthness, Scotland, 1960, (DEG Report 14D).

45. V. K. Saxena and S. C. Saxena, "Thermal Conductivity of Krypton and Xenon in the Temperature Range 350-1500"K," Journal of Chemistry Physics, Vol 51, No. 8, October 1969.

46. D. J. Collins and W. A. Menard, "Measurement of the Thermal Conductivity of Noble Gases in the Temperature Range 1500 to 5000 Degrees Kelvin, kelvin," Journal of Heat Transfer, 88c, 52-5.

47. R. S. Brokaw, "Estimating Thermal Conductivity for Non-Polar Mixtures: Simple Emperical Method," Ind. Eng. Chem. 47 (11), pp 2390-2400, 1955.

48. H. Ubisch, "The Thermal Conductivity of Mixtures of Rare Gases at 29°C and 520°C," Arkin Fysik, 16, 1, 93, 1959.

49. E. A. Mason and S. C. Saxena, The Physics of Fluids, Vol. 1, pp 361-369, 1958.

50. J. O. Hirchfelder, C. F. Curtiss, and R. B. Bird, "Molecular Theory of Gases and Liquids," Wiley, New York, 1954.

51. M. M. Paxton, "Mechanical Properties of Prototype FTR Cladding-20% C. W. 316 Stainless Steel Tubing," (App. A & B), HEDL-TME 71-59 Hanford Eng. Develop. Lab., Richland, Washington, April, 1971.

52. J. Belle, "Uranium Dioxide: Properties and Nuclear Applications," Naval Reactors, Division of Reactor Development, USAEC, U. S. Government Printing Office, 1961.

53. Peter C. Held and D. K. Wilder, "High Temperature Hemispherical Spectral Emittance of Uranium Oxides at 0.65 and 0.70 μm," J. Am. Cer. Soc., 52, pp 182-186, 1969.

54. "Handbook of Chemistry and Physics," 57th Edition, Chemical Rubber Publishing Company, Cleveland, Ohio, 1976. p. 3041.

55. F. E. Bard, B. C. Gneiting, and C. M. Cox, "A Thermoelastic Material Properties Correlation for Uranium/Plutonium Mixed Oxides," HEDL-TME 74-12 Hanford Engineering Development Laboratory, Richland, Washington, February, 1974.

56. J. B. Conway, R. M. Fincel, Jr., and R. A. Hein, "The Thermal Expansion and Heat Capacity of UO_2 to 2000°C," Trans. Amer. Nucl. Soc., Vol. 6, p. 153, 1963.

57. ASME Boiler and Pressure Vessel Code, Section III, "Nuclear Power Plant Components," 1971 Edition.

58. C. F. Braun, "Piping Design Guide for LMFBR Sodium Piping," SAN-781-1, February 1, 1971.

59. A. Biancheria, et al, "Oxide Fuel Element Development Quarterly Progress Report, September 30, 1969, WARD-4135-1, Westinghouse Advanced Reactor Division.

60. A. B. G. Washington, "Preferred Values for the Thermal Conductivity of Sintered Ceramic Fuel for Fast Reactor Use," UKAEA Reactor Group, Risley, TRG-Report-2236, September 1973.

61. H. Kleykamp, "Variation in the Thermal Conductivity of an Oxide Fuel Element During Burnup," Karlsruhe Nuclear Research Center, Germany, KFK-1245 (EURFNR-816), July 1970.

62. R. A. Laskiewicz et al, "Thermal Conductivity of Uranium-Plutonium Oxide," GEAP-13733, September 1971.

63. L. A. Lawrence and R. L. Gibby, "Effects of Pore Structure on the Melting Heat Rating of Oxide Fuels," HEDL-TME 72-81, May 1972, UC-25.

64. E. A. Aitken and S. K. Evans, "A Thermodynamic Data Program Involving Plutonium and Urania at High Temperatures," GEAP-5672, October 1968.

65. W. L. Lyon and W. E. Baily, "The Solid-Liquid Phase Diagram for the UO_2-PuO_2 System," GEAP-4878, December 1965.

66. J. K. Krankota and C. N. Craig, "The Melting Point of Plutonia-Urania Mixed Oxides Irradiated to High Burnup," GEAP-13515, July 1969.

67. L. B. Miller, G. H. Golden, R. E. Jarka and K. E. Phillips, "Characterization of the Power in an Experimental Irradiation Subassembly of Mixed-Oxide in EBR-II," ANL/EBR-II-047, Argonne National Laboratory, September 1971.

68. W. E. Warden, "Process Development to Fabricate 90% Dense Fuel for Irradiation Testing," HEDL-TME 71-149, October 1971.

69. J. E. Hanson, "Experiment Description and Hazards Evaluation for the Pacific Northwest Laboratory Mixed Oxide (UO_2-PuO_2) Irradiation in EBR-II, Task A Subtask I Irradiations," BNWL-650, July 1968.

70. L. B. Miller, R. E. Jarka, J. L. Gillette and F. S. Kirn, "Increasing The Central Power in EBR-II," Trans. Amer. Nucl. Soc., Volume 17, page 180-181, November 1973.

71. G. H. Golden, A. Gopalakakrishnan and R. A. Laskiewica, "Correlation and Interpretation of Data Relative to EBR-II Power Level," Proceedings Amer. Nucl. Soc., Irradiation Experimentation in Fast Reactors; September 10-12, 1973.

72. D. S. Dutt, R. B. Baker, S. A. Chastain, "Modeling of Postirradiation Fuel-Cladding Gap in Mixed Oxide Fuels," HEDL-TME 74-19, April 1974.

73. David F. Shanno, "REEP-Nonlinear Estimation Package," IBM Share Program Library, January 27, 1967.

74. D. S. Dutt, D. C. Bullington, R. B. Baker, L. A. Pember, "A Correlated Fission Gas Release Model for Fast Reactor Fuels," Trans. Amer. Nucle. Soc., Vol. 15, No. 1, June 1972.

75. J. H. Kittel, "Guide for Irradiation Experiments in EBR-II," Revision 4, Argonne National Laboratory, Argonne, Illinois, February 1971.

76. J. H. Kittel, "Guide for Irradiation Experiments in EBR-II," Revision 10, Argonne National Laboratory, Argonne Illinois, December 1973.

77. V. F. Jankus and R. W. Weeks, "LIFE-II - A Computer Analysis of Fast-Reactor Fuel-Element Behavior as a Function of Reactor Operating History," First International Conference on Structural Mechanics in Reactor Technology, Berlin, Germany, September 20-24, 1971.

78. M. C. Billone, J. Rest, and R. B. Poeppel, "UNCLE - A Computer Code to Predict the Performance of Advanced Fuels in Breeder Reactors," Trans. Amer. Nucl. Soc. 19, 96 (1974).

79. B. L. Harbourne and W. H. McCarthy, "Axial Fuel Redistribution by Vapor Transport in LMFBR Fuel Rods," Trans. Amer. Nucl. Soc., Volume 23, page 146, 1976.

80. R. C. Martinelli, Trans. ASME 69, 947-959 (1947).

81. D. S. Dutt, R. B. Baker, J. W. Weber and S. A. Chastain, "A Correlated Model for Prediction of the Performance of LMFBR Fuel," Trans. Amer. Nuc. Soc., Vol 22., p. 228, November 1975.

APPENDICES

APPENDIX A

APPENDIX A

Indicators of Extents of Fuel Melting in HEDL P-19 and P-20

The purpose of this appendix is to briefly review the type of indicators that were used for the determination of the extent values found in this report. Both radial and axial extents will be reviewed. Appendix K of Reference 3 discusses some general observations on melt boundaries in past work.

Radial Extent of Melting as Determined from Transverse Ceramography

Transverse ceramography sections removed from selected axial locations of once molten fuel pins were mounted in clear resin and polished. Macrophotographs (Figure A-1), autoradiographs (β-γ, Figure A-2) and a 75x photomosaic (Figure A-3) were then made from the sample in this condition. A strong chemical etch was then used. This etch (80 H_2O_2(30%)20 H_2SO_4) had shown in the past a quality of accenting molten fuel zones. The sample then had another 75x photomosaic (Figure A-4) made from it in this state (usually with oblique lighting which further accentuated the molten fuel zone).

The main determining features for the extents of melting were:

(1) β-γ autoradiographs[A1]: The largest distinct radius of the activity-depleted (white) zone in the annulus of active (dark) and depleted zones in the molten region was taken as an

---

[A1] The extent of an enriched zone in the α autoradiography (Figure A-9) indicates the extent of melting at shut-down. However, it is usually fairly indistinct.

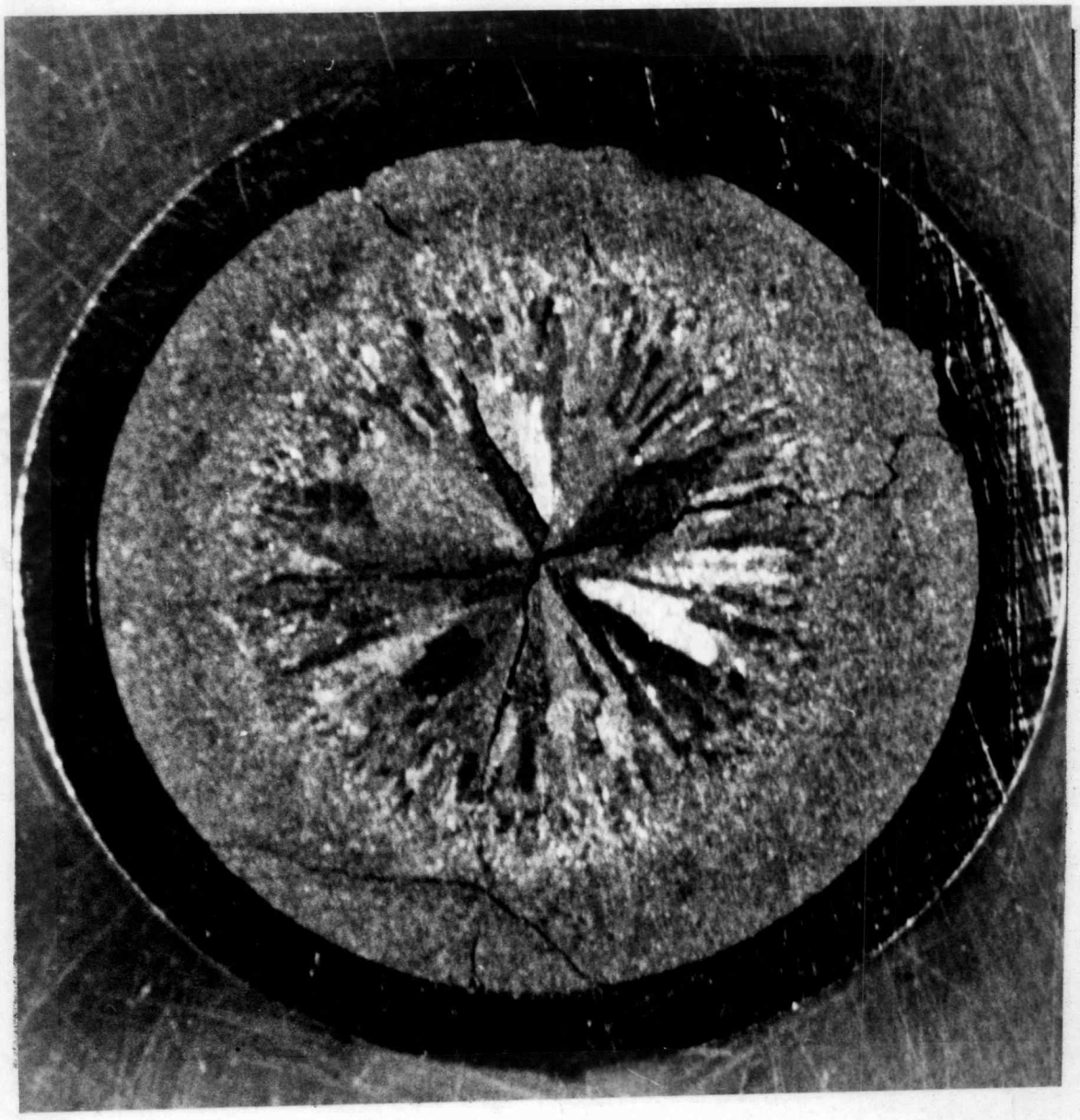

Figure A-1. Example of Marco Photography of a Transverse Fuel Section in "As-Polished" Condition (P-19-35, Sample D).

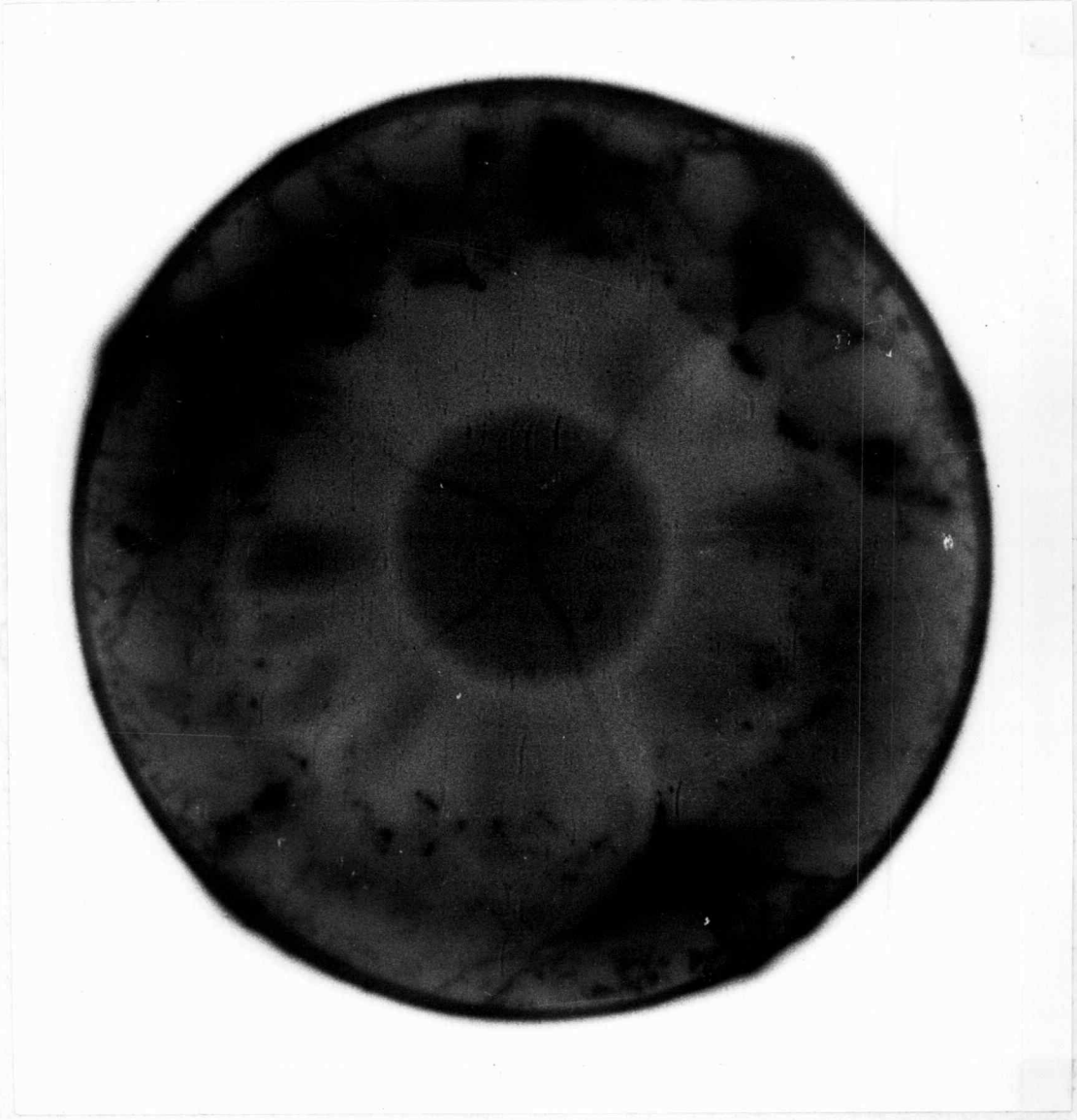

Figure A-2. Example of β-γ Autoradiograph of a Transverse Fuel Section (P-19-35, Sample D).

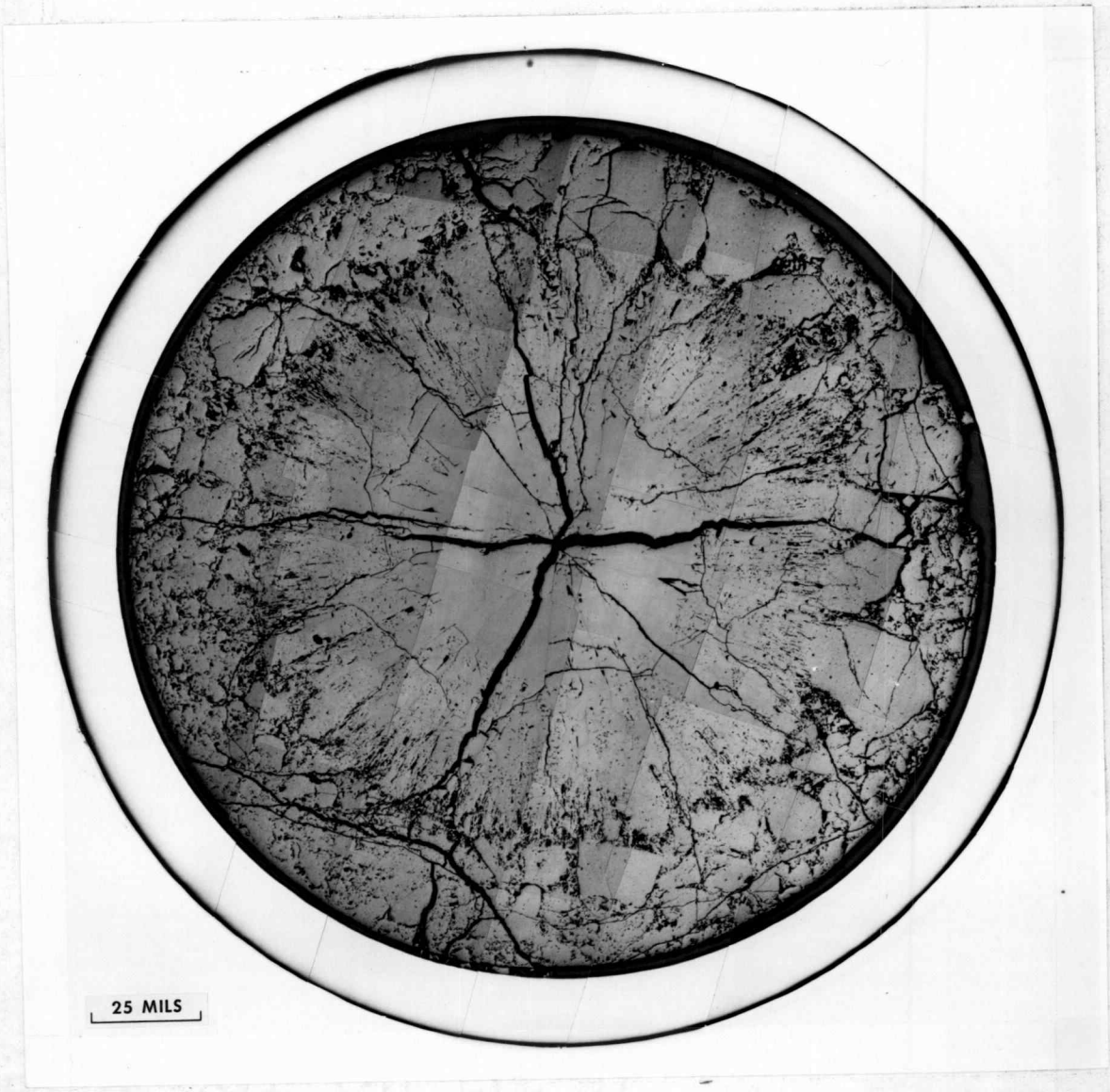

Figure A-3. Example of Photomosaic (Originally 75X) of a Transverse Fuel Section in "As-Polished" Condition (P-19-35, Sample D).

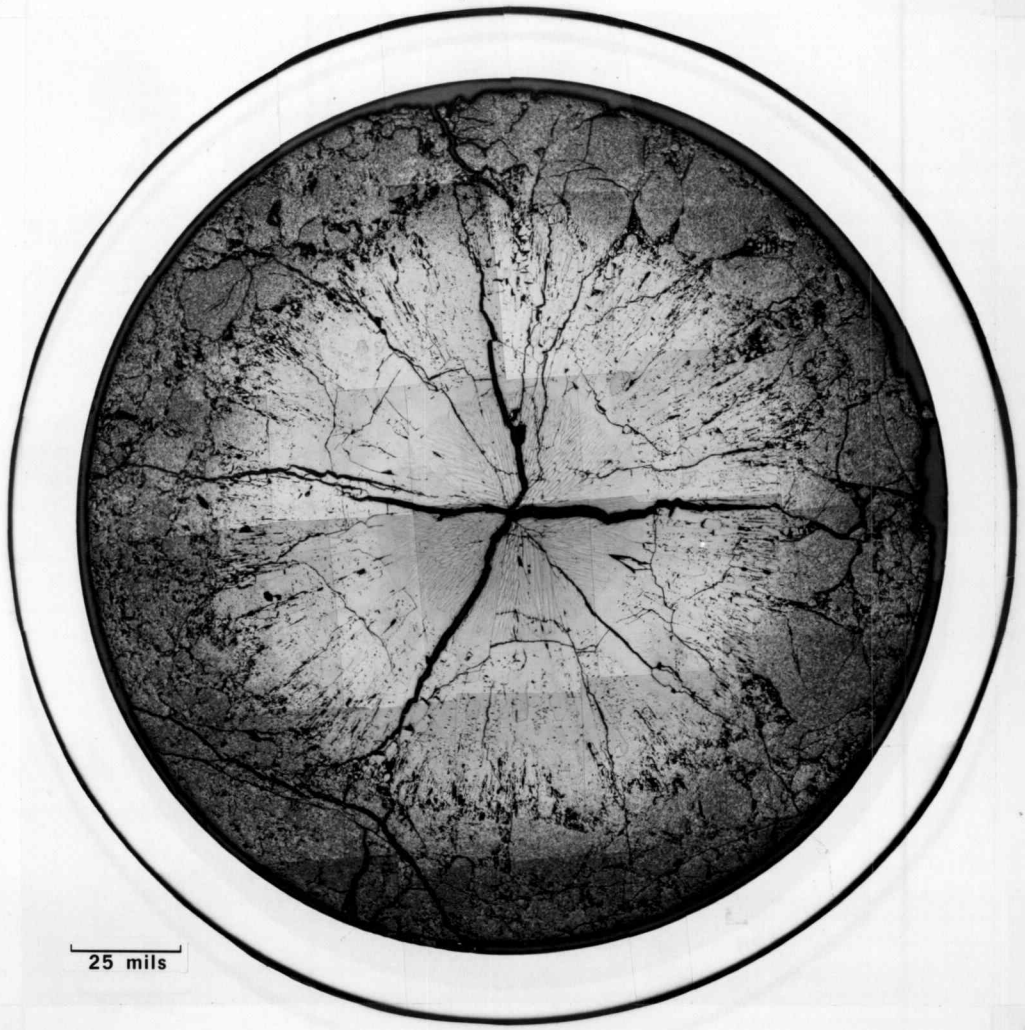

Figure A-4. Example of Photomosaic (Originally 75X) of a Transverse Fuel Section Chemically [$80H_2O_2(30\%)20H_2SO_4$] Etched P-19-35, Sample D).

indicator of furthest extent of melting. The active and depleted zones (Figure A-2 and A-6) are believed to correspond to concentrations of Ruthenium.

(2) 75x Photomosaics

As-polished: The extent coincides with the furthest extent of a zone in the fuel free of small pores (Figure A-3). This can be also seen in Figure A-5, an etched sample.

Chemically Etched: The extent is characterized by a line[A2] (Figure A-5) surrounding the pore free zone when the sample is viewed with oblique lighting.

The radial extents of melting are thus determined using all three of these indicators.

The interpretation of the pore free band in the fuel is that its furthest extent is the maximum extent of fuel melting during the test and the inside diameter is the extent of the melting just prior to the reactor scram when the test was completed. This is supported by the dendritic structure of the fuel in this inside region (Figure A-5).

Axial Extent of Melting as Determined by Longitudinal Ceramography

As shown in Figures 6 and 7[A3] in the text, the axial extent of melting can be characterized fairly well using neutron and betatron

---

[A2]Once molten fuel etches at a different rate than fuel which has not melted causing a "step" at the interface after etching.

[A3]Note the reduced photomosaics in these figures are of samples with a "stain" etch rather than the chemical etch. This was used prior to the chemical etch to obtain fuel restructuring detail.

Figure A-5. Ceramographic Appearance of an Etched Section D from HEDL P-19-35 (This Area is at the Center of the Fuel. Oblique Illumination was Used).

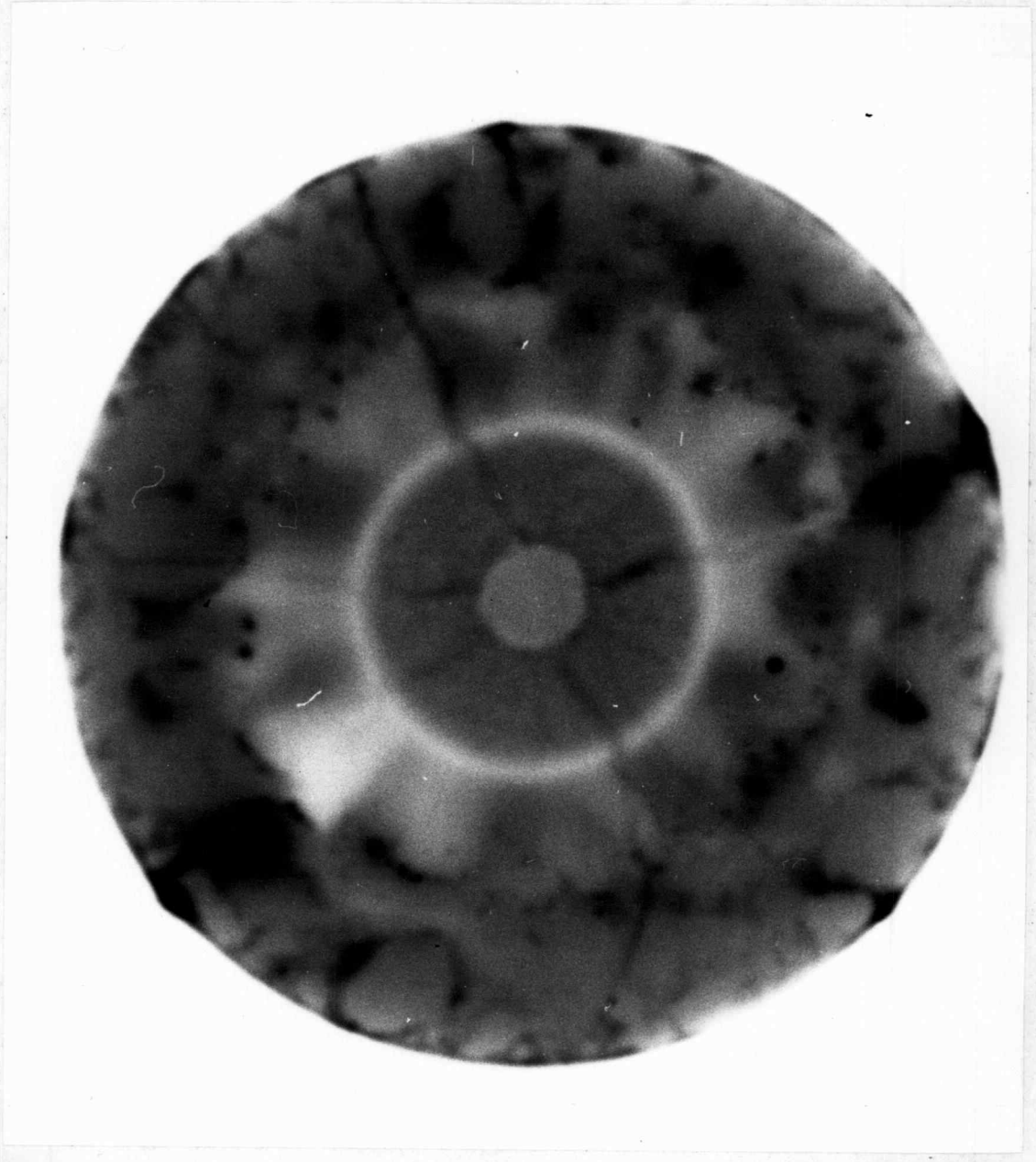

Figure A-6. Example of Molten Zone Extent Indicator on β-γ Autoradiograph. (Note White Continuous Band Around Molten Annulus.)

radiographs. Here the furthest extent of melting from the center is found from the last discontinuity (such as a plug, bubble, etc.) in the central void. Experience has shown this to be a very consistent indicator.

Ceramography samples were cut from the pins and these samples contained the areas which appeared to be the axial extents of melting based on the radiography. Once these samples were ground to the geometric center of the cladding, the longitudinal sections were then prepared like the previously described transverse sections. The same indicators as described previously were then used to determine the furthest axial extent of melting (A-7 thru A-9). One other indicator was also used. This was the central void appearance in the 75x photomosaics. In the unmolten zone the central void is constant in diameter, and its edges are rough from lenticular voids penetrating the walls. In the molten portion of fuel, the central void diameter is eratic and its walls are very smooth.

The P-20 fuel experienced a small amount of molten fuel relocation to the bottom of the fuel column which did not occur in P-19. Here the central void appears to have been filled with molten fuel to the bottom of the fuel column even though the fuel temperatures were not high enough to cause fuel melting locally. The indicators described for the radial extents were used exclusively to determine the bottom axial extents in these cases. Further it should be noted that because of this relocation the extents of melting found from the bottom portions of P-20 pins are probably somewhat lower (conservative) than would be expected.

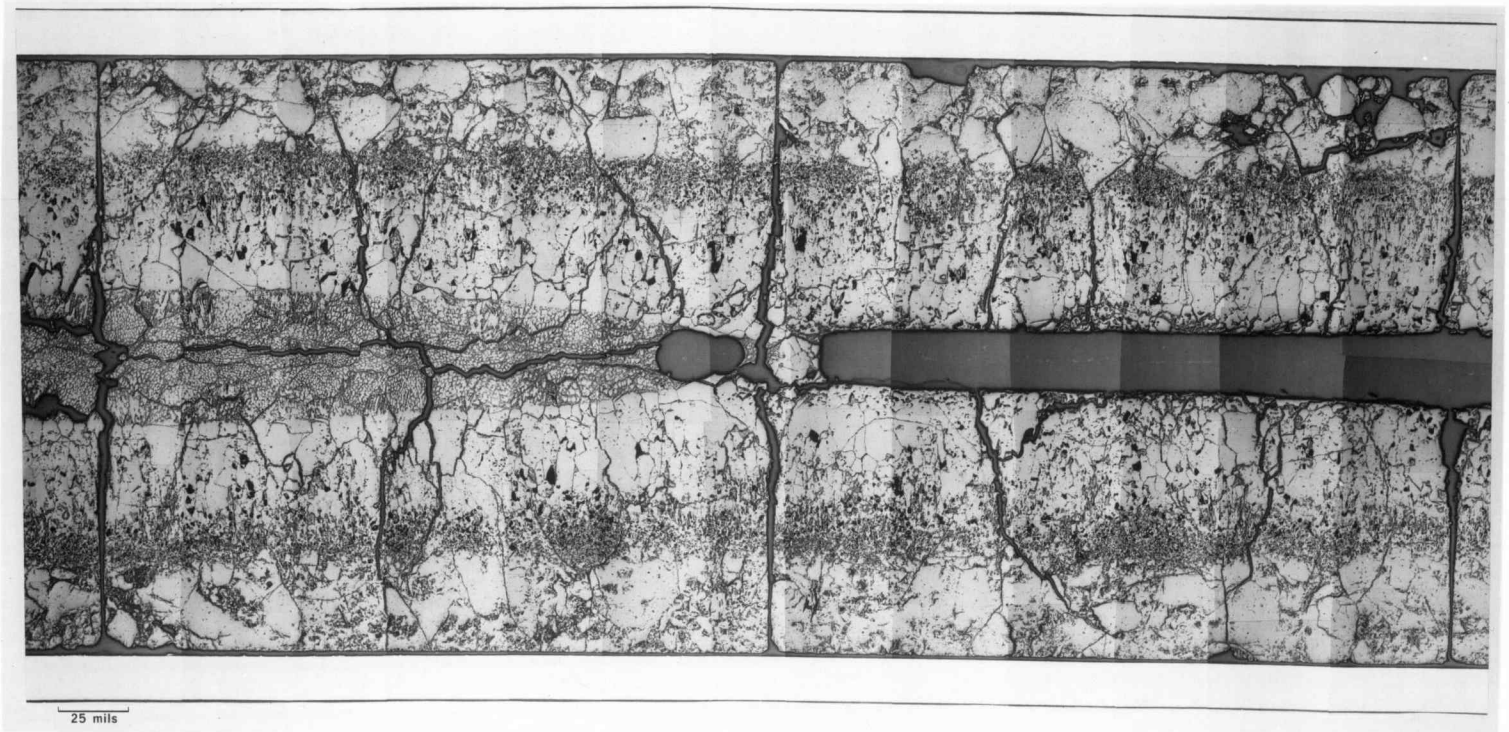

Figure A-7. Example of Molten Fuel Axial Extent in "As-Polished" Longitudinal Sample (P-19-27R, Sample H-1).

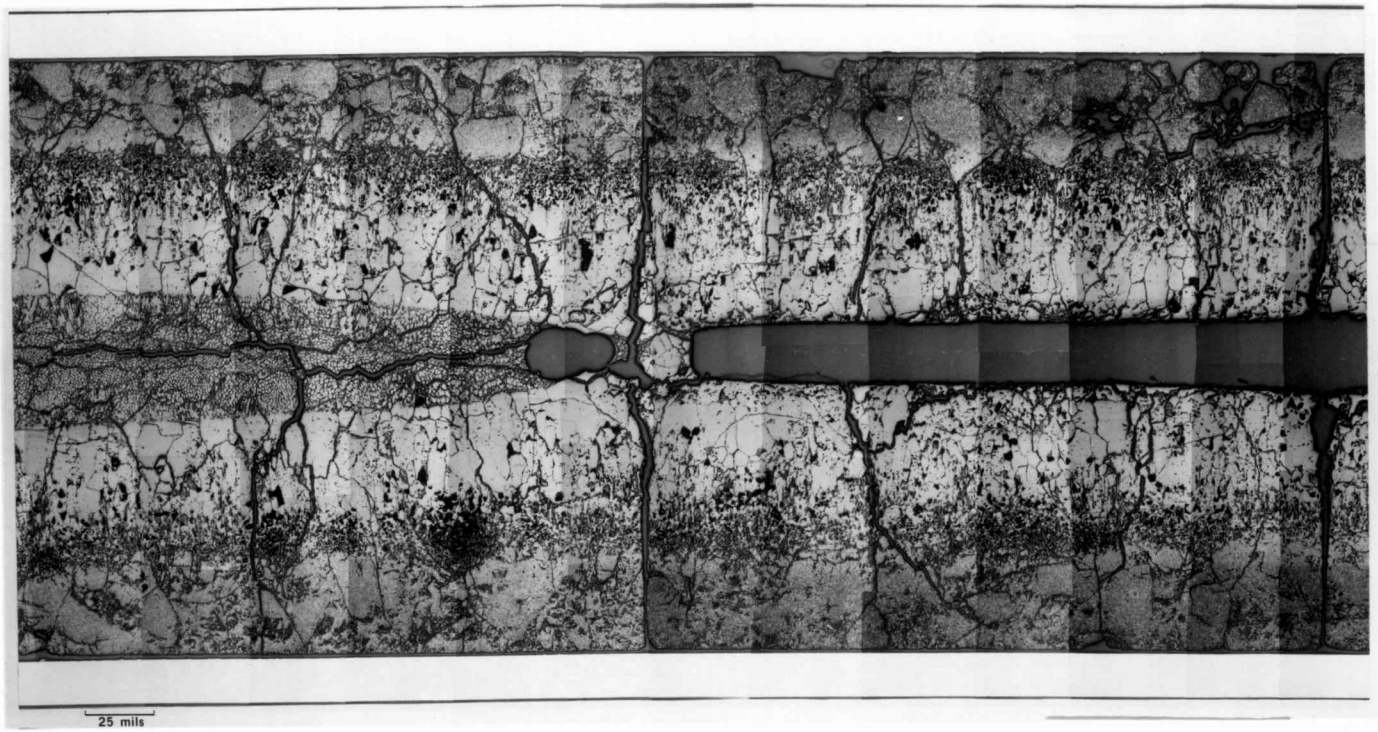

Figure A-8. Example of Molten Fuel Axial Extent After Chemically Etching a Longitudinal Sample (Molten Fuel is to the Left; Note Dendritic Structure).

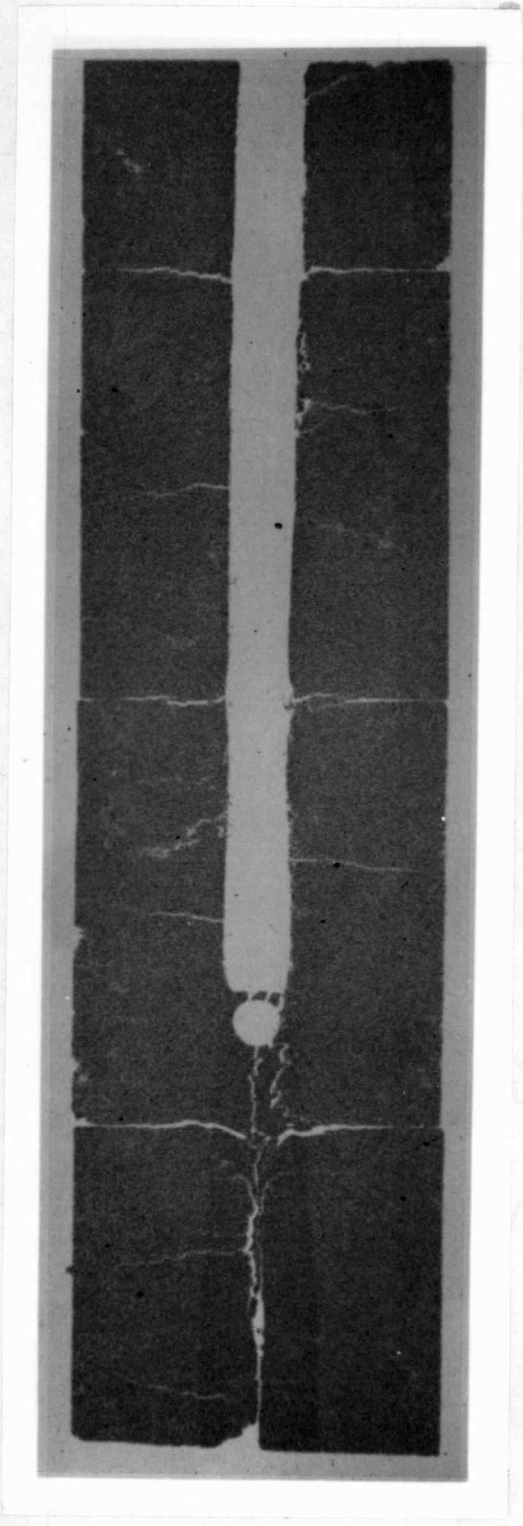

Alpha 10x

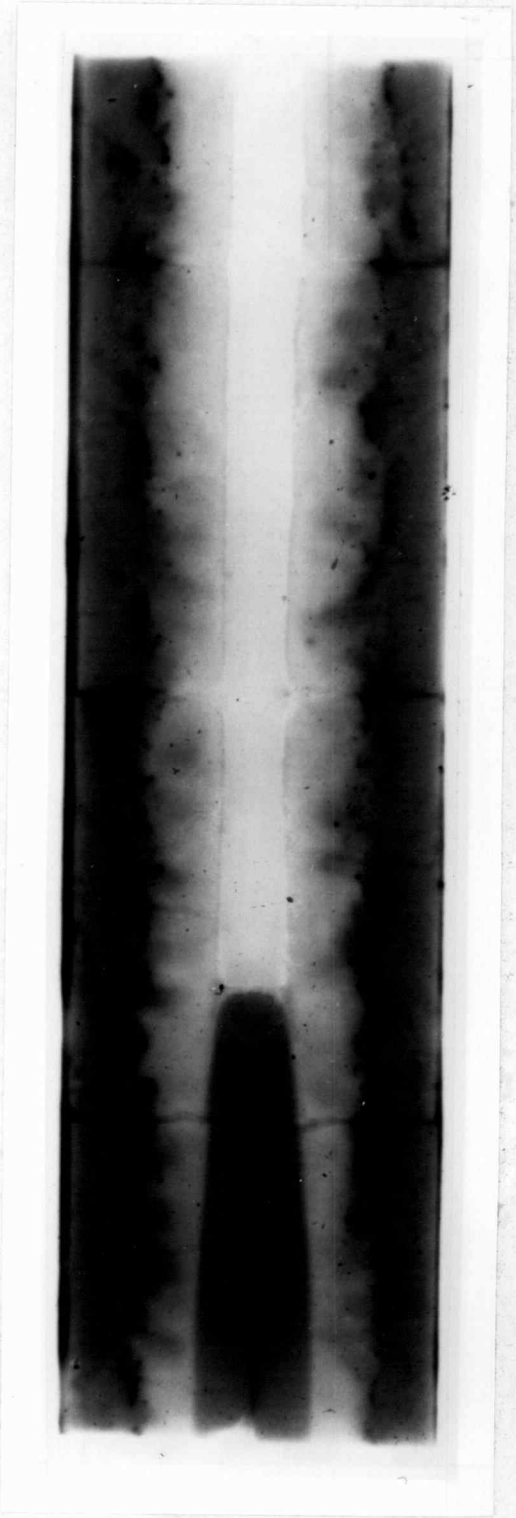

Beta-Gamma 10x

Figure A-9. Examples of Molten Fuel Indicators Present in Autoradiography of Longitudinal Fuel Section (P-20/19-34G).

This is because of the extensive plugging of the central void beyond where melting could occur because of local fuel temperatures.

For the analyses in this report, the axial extents of melting were taken with respect to the central void. Where no fuel plugging occurred at the axial extent of fuel melting, the furthest extent of the melt indicators was taken as the axial extent of melting. If, however there was a once molten fuel plug at an axial extent of melting the extent of this plug (Point A, Figure A-10) was not necessarily used as the axial extent of melting in the analyses. Instead, the first position (Point B, Figure A-10) back from the furthest extent of the plug where the radius of the melt indicators equaled the radius of the local central void, observed in the unmolten fuel beyond the fuel plug, was taken as the axial extent of melting. This then assured that the temperature at the central void was at fuel melting ($\sim$ 5000°F or 2060°C). The technique eliminated the few cases where a false "axial extent" of melting would have been used; caused by molten fuel relocating (being pushed) beyond where the peak fuel temperatures were high enough for melting to occur. The correction in the majority of cases was very small.

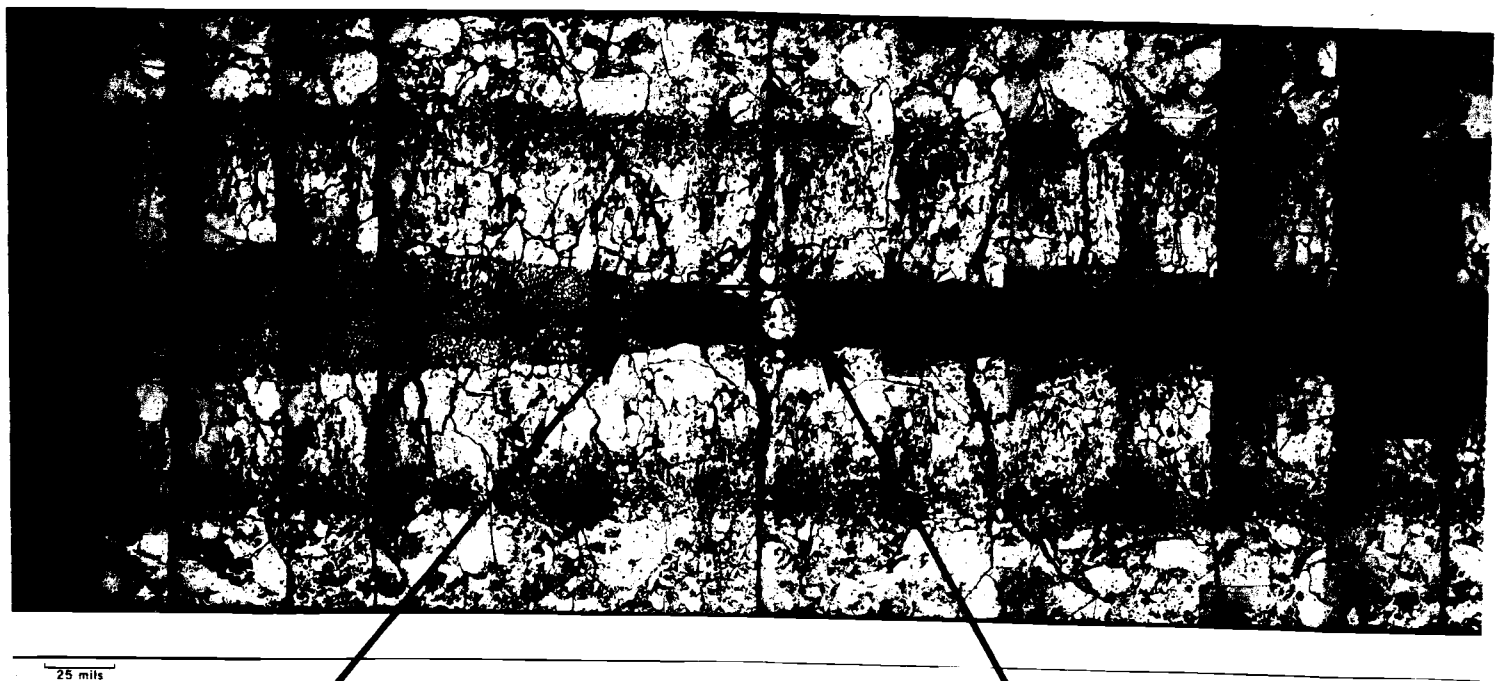

Figure A-10. Axial Extent of Melting with Respect to the Central Void (P-19-27R, Sample H-1).

APPENDIX B

APPENDIX B

Characterization of Axial Power Profiles and Normalization of Pin Powers

Axial Power Profile for HEDL P-19

The axial power profile used for the HEDL P-19 fuel pins was based on a curve taken from an EBR-II Users Guide[75] for U-235 fission rates. This was confirmed with a series of measured burnup values taken from the P-19-33 fuel pin. This pin experienced no fuel melting. Figure B-1 shows this curve and the results of the burnup analyses, which were based on Nd-148. As will be noted in the following section while the burnup values measured in this manner have a large absolute uncertainty the relative values should be very good.

Gamma scan results from P-19-33 and other P-19 fuel pins also confirmed the axial profile shown in Figure B-1.

Axial Power Profile P-20 Phase III

The axial power profile for Phase III was derived from burnup samples taken from four "fresh" pins used in this portion of the test. Samples were taken at various axial locations along the length of the fuel column and then were analyzed for fuel burnup based on Nd-148. Where melting was present in the fuel column, samples were taken where large shrinkage cavities existed (determined by neutron and betatron radiography). This minimized the possibility of fuel from other locations moving into the burnup sample location and remaining there affecting the burnup measurement. Fuel pins irradiated in a fast flux environment should exhibit a uniform radial burnup profile, thus, fuel that relocated out of a section will not affect the burnup measurement.

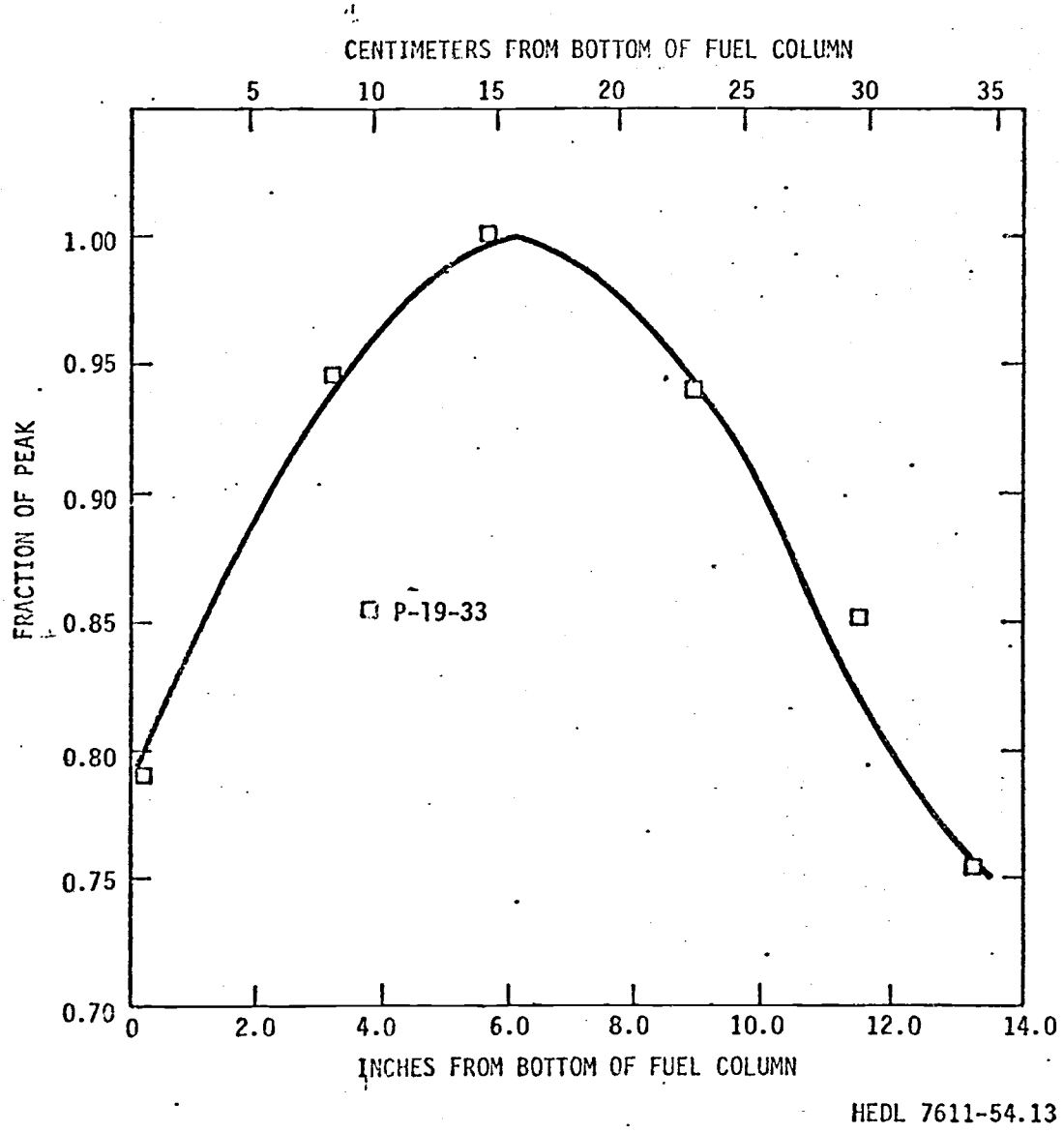

Figure B-1. Axial Power Profile for HEDL P-19 Pins.

The burnup results for each of four pins were normalized to peak values, and these data were then fit with a fourth order polynomial, shown in Figure B-2.

While the uncertainty expected for these low burnup levels (about 90 MWd/MTM) is fairly high (about ± 30%) the precision of the measurements was shown to be much better than this. An exchange of a number of HEDL P-19 and P-20 burnup samples between the HEDL and LASL chemical laboratories showed the largest disagreement in measured burnup of only four percent and the average disagreement found between seven cross-checks was less than one percent.

The power profile in Figure B-2 agreed reasonably well with the profile determined from Zr-95 gamma scan results, but was somewhat different (shifted 0.4 inches toward the top and no peaking at the ends) from the curve described for fission rates of ^{235}U taken from the EBR-II Users Guide[76]. This later result is not unexpected since P-20 Phase III had a special core loading and was experimental (no axial stainless steel reflectors) fuel rather than the driver fuel discussed in the guide.

Estimate of HEDL P-20 Peak Pin Powers Normalized to HEDL P-20 Powers

Peak pin powers were first calculated from post-run fission rate maps provided by the ANL EBR-II project. These were multiplied by 0.91 as noted in the text, Section B.3.a. From the powers and the axial power profile derived above, calculations of local power-to-incipient fuel melting, Q'_m were made for the two "fresh" spare P-19 pins used in P-20 Phase III. Using a version of the SIEX-M1 computer code the Q'_m

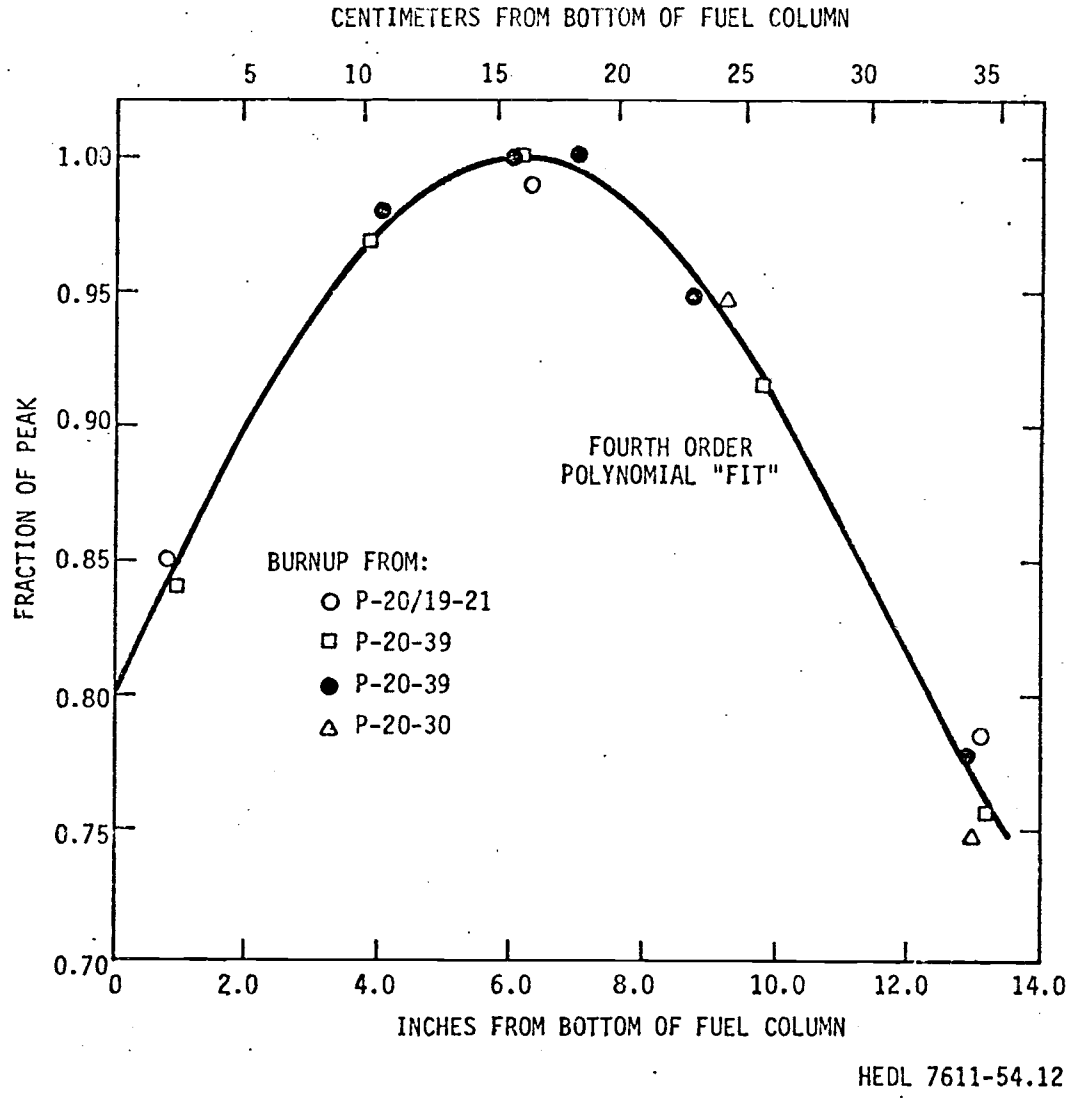

Figure B-2. Axial Power Profile for HEDL Phase III Pins Based on Burnup Analyses.

values were normalized to FFTF conditions of 90.4% T.D. pellet density and 1060°F cladding ID temperature as described in Section B.4 of the text. These results were then compared to normalized Q'_m values found in the HEDL P-19 test for similar gap size pins. The average difference in normalized Q'_m values was found to be 12.6 percent lower for the P-20 values. This indicated, since the normalized Q'_m values should be the same for both experiments with the same fuel-to-cladding gap size and the same fuel, that the powers calculated for P-20 were too low. From this analysis and the supporting data described below, it was decided that the P-20 pin powers should be normalized to the P-19 power[B1]. Adjustment factors were applied to the P-20 powers until normalized data from the two P-19 pins included in P-20 agreed with normalized Q'_m values from P-19 work. It was found the pin powers had to be adjusted up eleven percent for the P-20 pins (thus 2% higher than the original fission rate values supplied by ANL) in order to make the two sets of data agree.

As substantiating evidence that the P-20 test was running at a higher power, the results from Nd-148 burnup analysis from P-19 and P-20 were checked. Burnup measurements from both experiments, as was noted in the previous section on axial power profile, are very consistent in values and have been cross-checked for precision. The ratio of these

---

[B1] Thus relative comparisons of Q'_m could be made. The P-19 powers were chosen as the base to normalize to, rather than P-20 powers calculated from post-run fission rates, because of the in-depth analysis[67] made for P-19 by ANL as opposed to no special calculations made for P-20.

burnup measurements between the two tests should be a reasonably accurate value. Taking the average of the peak burnups from a number of similar pins from each experiment and dividing by the integrated area under the reactor power-time history, (i.e. the total megawatt-hours for the reactor) Figures 3 and 5 of the text, it is found:

$$\underline{\text{P-19}} \qquad \frac{.0061 \text{ At\%}}{287.4 \text{ MW-hr}} = 2.12 \times 10^5 \ \frac{\text{At\%}}{\text{MW-hr}}$$

$$\underline{\text{P-20}} \qquad \frac{.0094 \text{ At\%}}{393.5 \text{ MW-hr}} = 2.39 \times 10^5 \ \frac{\text{At\%}}{\text{MW-hr}}$$

This indicates, assuming a linear relation between reactor power level and fuel burnup, P-20 was operating at 12.7 percent higher power than P-19. Burnup was accumulating this much faster per megawatt-hour in the test fuel for the P-20 test. This confirms the magnitude of the absolute power difference between the P-19 and P-20 tests. The final difference relative to P-19 power calculated by normalizing the Q'_m of the P-19 pins in P-20 was about 9 percent, which is a more conservative value than indicated by the burnup.

Another fact confirming the higher power in HEDL P-20 as compared to P-19 was the response of the "fresh" 0.230 inch OD pin with 0.0055 diametral fuel-to-cladding gap in each test. These pins had different fuel batches, however, their response would be expected to be very similar. The P-19 pin (in P-19) showed no signs of melting even at the peak power region. The P-20 pin had substantial fuel melting. This would indicate P-20 was operating at a higher heat rate than P-19.

APPENDIX C

APPENDIX C

Summary of Results from Analysis of Ceramography and Fission Gas Release from Phaes I and II of HEDL P-20

The purpose of Phase I and II of HEDL P-20 was to accumulate fuel burnup under steady state power conditions of about 14 kW/ft (460 w/cm). After each phase, some pins were removed and others added so three burnup levels (as noted in the text) were achieved. For each Phase I and II pin used in Phase III, a sibling pin was examined without Phase III exposure. Additional pins of interest were also irradiated and examined. The performance results of these highly characterized pins contain valuable data on fuel restructuring and fuel pin response under well defined conditions. The behavior of these pins must be understood before the performance of the P-20 preirradiated Phase III pins can be fully understood. The following summarizes the analysis of these Phase I and II pins with respect to data associated with ceramography samples and fission gas release.

Each of the pins irradiated in Phase I and/or II had three transverse fuel ceramography sections taken from it at about 1.5 inches (3.8 cm), 6.2 inches (15.8 cm), and 12.0 inches (30.5 cm) above the bottom of the fuel column. Along with other data, a 75x photomosaic was made from each of these samples in both the polished and etched condition. Examples of the etched (with "stain" etch) samples from "Phase II only" (7200 MWd/MTM) pins are shown in Figures C-1 and C-2. Each set of mosaics for a sample were then measured for central void, columnar grain region and equiaxed grain region radii. Also, residual fuel-to-cladding gap sizes were measured.

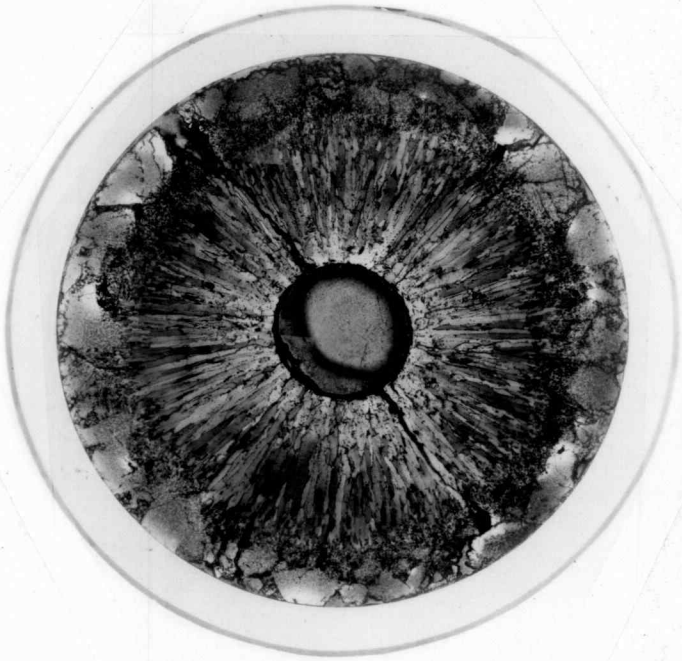

SAMPLE D
1.50 INCHES FROM BOTTOM FUEL COLUMN

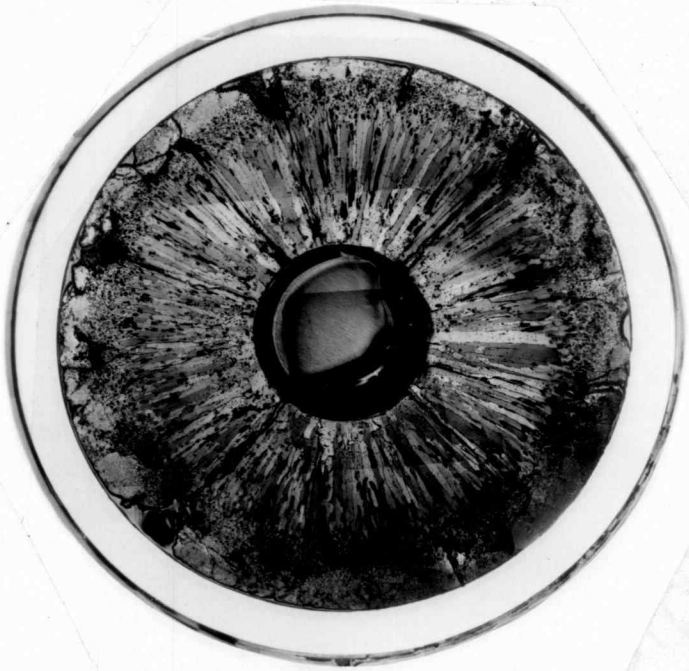

SAMPLE G
6.250 INCHES FROM BOTTOM FUEL COLUMN

Figure C-1. Etched Transverse Fuel Ceramography from HEDL P-20-5.

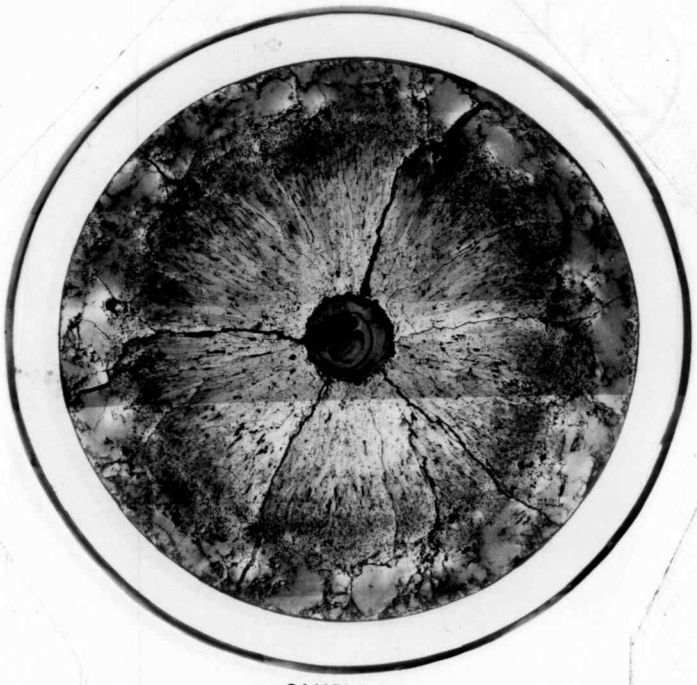

SAMPLE D
1.50 INCHES FROM BOTTOM FUEL COLUMN

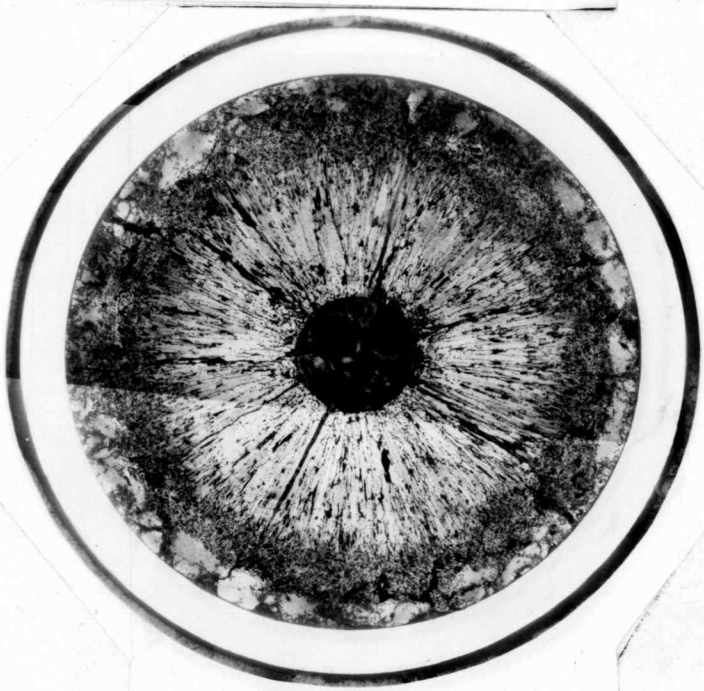

SAMPLE G
6.250 INCHES FROM BOTTOM FUEL COLUMN

Figure C-2. Etched Transverse Fuel Ceramography from HEDL P-20-36.

Figures C-3 and C-4 summarize the results of the measurements of the central void and columnar grain region radii. From this, within the scope and limitations of the test, the following conclusions with respect to the columnar grain region and gap conductance can be drawn:

1) There is no increase in columnar grain region size with time or burnup. The maximum extent was reached by the end of Phase I. This would indicate the temperature drop across the fuel-to-cladding gap is not increasing with time (assuming a constant columnar grain formation temperature).

2) As would be expected, there is a trend of increasing region size as the fabricated gap size increases, indicating the maximum fuel temperatures are dependent on original gap size. However, there is a leveling off of this increase above 0.0075 inch (0.019 cm) gap sizes up to the 0.0096 inch (0.024 cm) gap pin (the largest in the study).

3) The 18% Xe tagged pins showed slightly larger, about 6%, region sizes than the untagged pins. This shows, as expected for a 0.0077 inch (0.20 cm) gap, an increased temperature drop across the gap resulting in higher fuel temperatures. Again, however, there is no increase of region size with time.

4) The low pressure preslugged fuel results show a slightly smaller restructured region (with a 0.0077 inch gap) than the high

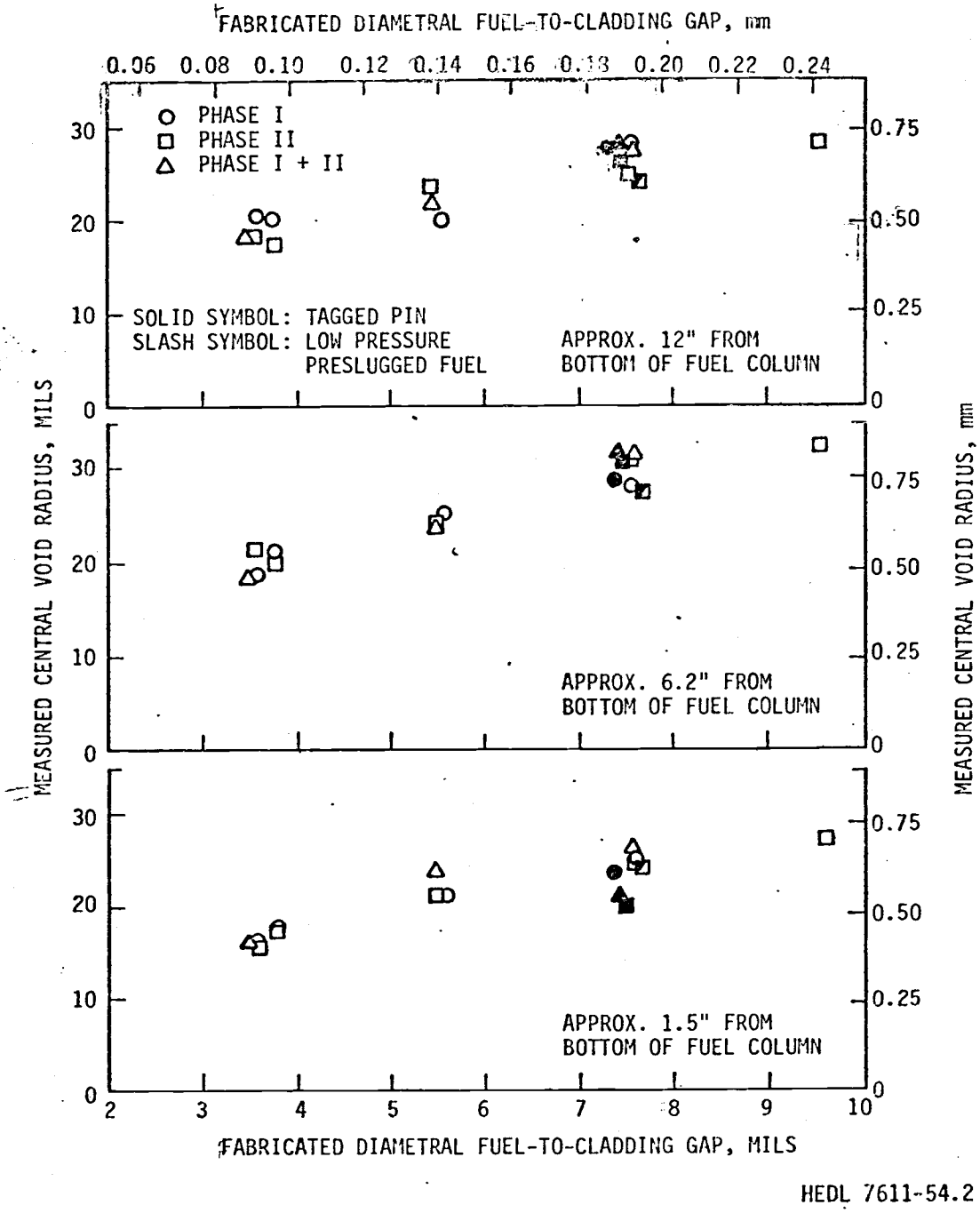

Figure C-3. Measured Fuel Central Void Radii for HEDL P-20 Phase I and II Pins.

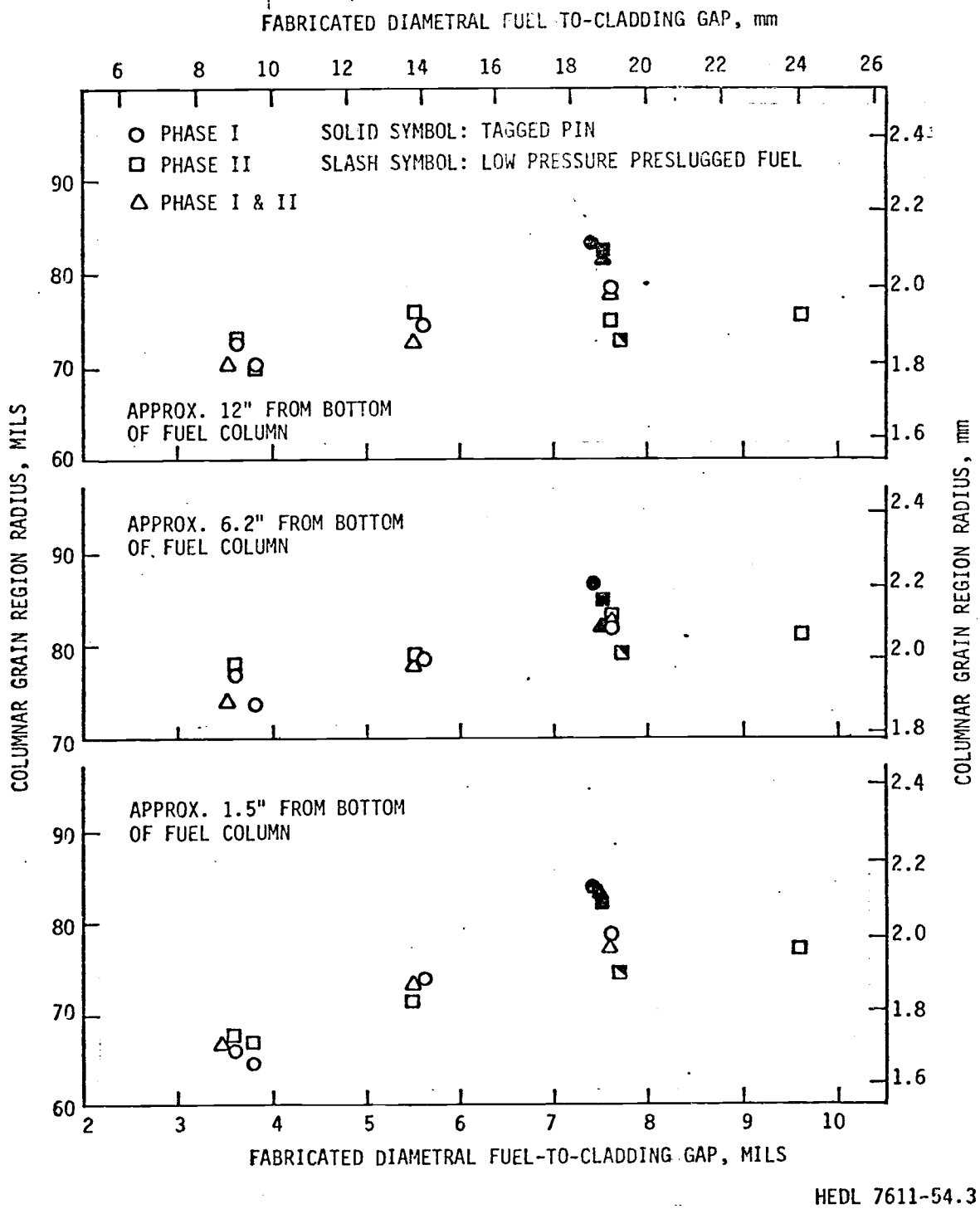

Figure C-4. Measured Columnar Grain Region Radii from HEDL P-20 Phase I and II Pins.

pressure preslugged fuel. The difference between the performance of the two fuel types appears to be minimal[C1].

Thus, maximum fuel temperature appears to occur at Beginning-Of-Life, (BOL). From then on there is an improvement (or, at worst, no change) in the overall heat transfer from the fuel-to-cladding. These maximum temperatures form the maximum extents of the columnar grain regions. Analyses from measurements of this region should relate to this maximum condition not necessarily to the End-Of-Life (EOL) conditions (or time-averaged conditions) of the fuel as is sometimes done.

Results from the central void measurements indicate a marked dependence on gap size and for the most part follow columnar grain size trends. However, the effects of gap voidage moving to the central void[(26)] as will be discussed later, are affecting the central void sizes also. This is evidence in the proportionally larger central void of the 0.096 inch gap pin, while its columnar grain region is no larger than the 0.0075 inch gap fuel.

Figure C-5 summarizes the results of the "equiaxed" grain region measurements. This region is identified in this study as the region where gas (assumed to be fission gas) has noticeably collected on the fuel grain boundaries. This region, the extent of which is most likely

---

[C1]The small difference observed could be accounted for in part by the low pressure preslugged fuel being 0.5% T.D. higher density (hence a potentially higher thermal conductivity than the other) and/or by the fact this fuel also had less absorbed nonhelium gases from fabrication (i.e. if there is an effect on gap conductance at BOL from released absorbed gas this effect would be smaller for the low pressure preslugged fuel.)

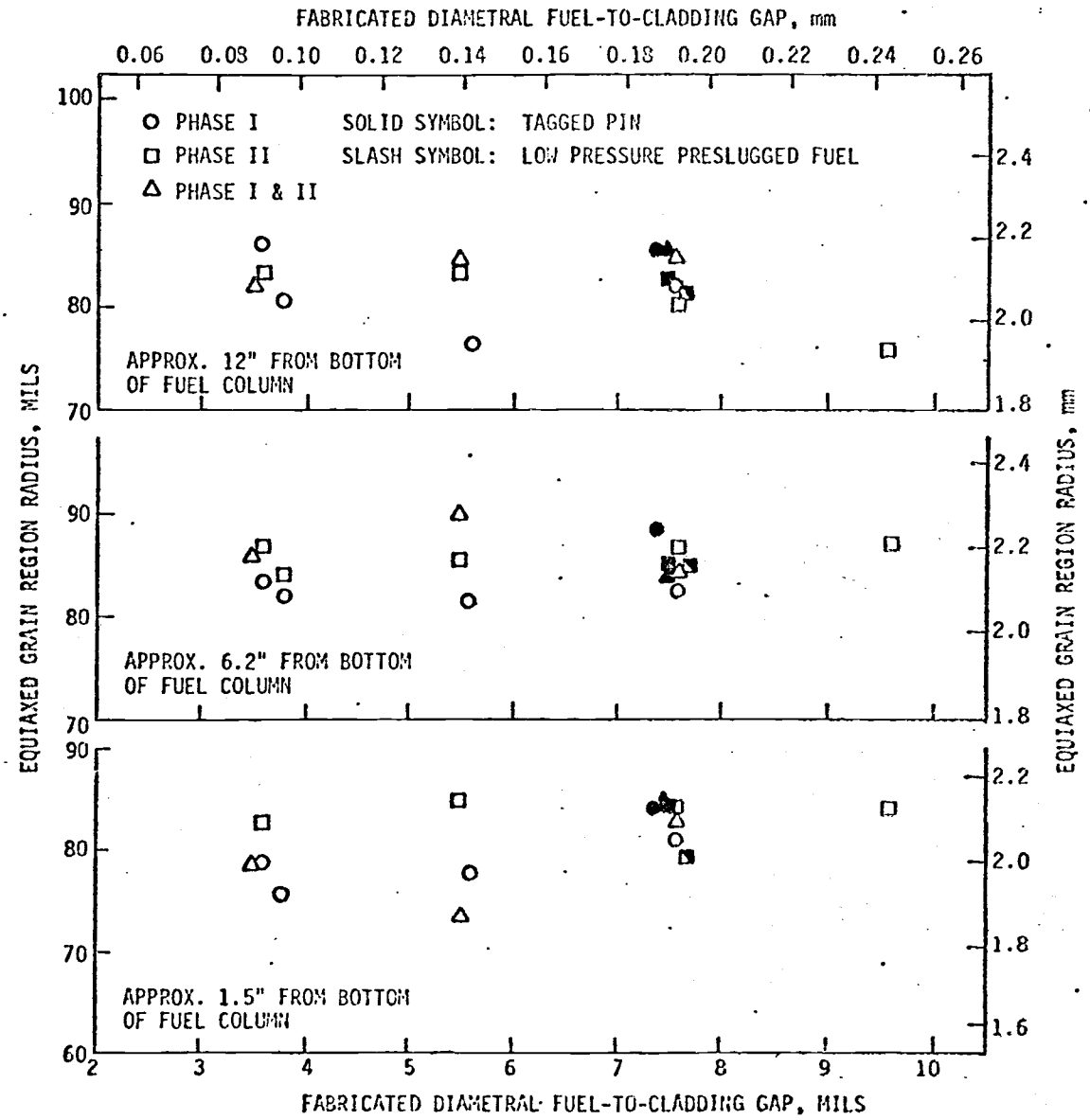

Figure C-5. Measured Equiaxed Grain Region Radii from HEDL P-20 Phase I and II Pins.

dependent on an isotherm and time, is probably much slower forming than the columnar grains, which are formed by fabricated porosity migrating up the thermal gradient. The "equiaxed" region extent is also much more difficult to discern, especially with the high pressure preslugged fuel structure. Thus, the scatter of the measurements can be expected to be greater than that observed for the columnar grain region measurements. Conclusions that may be drawn from Figure C-5 for the equiaxed grain region data are:

1) There appears to be only a slight dependence on original fabricated gap size.

2) There is a small increase in region size with time.

3) There is no observable consistent effect of the Xe tag or the low pressure preslugged fuel on the radius of the equiaxed grain region.

These conclusions suggest that the equiaxed grain regions matured after the fuel temperatures had decreased from their peak values and the fuel-to-cladding gaps, as will be shown in the next paragraph, had closed to about the same size for all the pins. This would cause the isotherm needed for the region to form to be at about the same radial location in all the pins.

Figure C-6 shows the results of measurements of the residual fuel-to-cladding gap. These were measured in a manner similar to that described in Reference 72. Conclusions which may be drawn from these data are:

1) There is a rapid closure of the fuel-to-cladding gap early in life that results in all the gap sizes coming to about the same 0.001 to

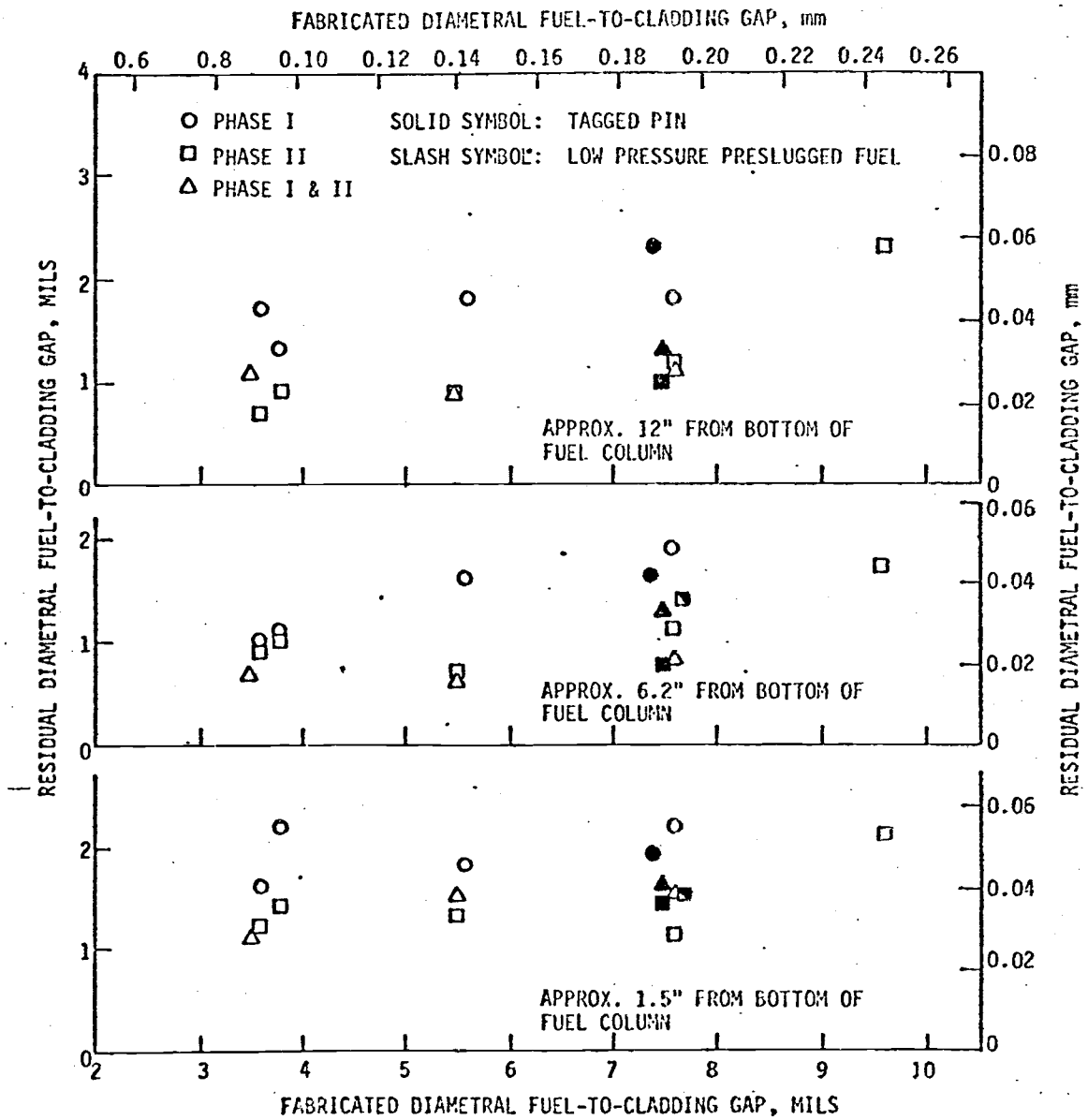

Figure C-6. Measured Residual Diametral Fuel-to-Cladding Gaps from HEDL P-20 Phase I and II Pins.

0.0025 inch (0.03 to 0.06 mm) diametral gap size range by the end of Phase I. Then there is continuing closure at a much slower rate.

2) As discussed in Reference 72 there is an apparent local power, time/burnup/reactor cycles, and original gap size dependence for the closure (note difference in measurements at the three axial positions).

These data support the preceeding conclusions for the restructuring region data; that there is a maximum gap size (maximum temperature drop across the gap) at BOL that accounts for ealy maximum fuel temperatures that drop with time.

In summary, the ceramography data lead to the conclusion that, within the range of this test, there is a maximum fuel-to-cladding gap size very early in life, resulting in a maximum temperature drop across the gap and maximum fuel temperatures. This maximum accounts for the extent of the columnar grain region. There is then rapid fuel-to-cladding gap closure to the levels seen in Figure C-6. After that, the gap size is fairly stable and the maturing (as gas is formed) "equiaxed" grain region forms as observed in Figure C-5. The columnar extent does not change with time since the maximum temperatures at BOL are never surpassed.

Figure C-7 summarizes the results of the calculation of the fission gas release based on measurements of fission gas recovered and burnups from Phase I and II sibling pins. The dependence of percent fission gas release for "Phase I only" pins shows the expected decreasing trend with decreasing gap size. There would be less gas released in pins with lower fuel temperatures (i.e. small gaps). However, for the "Phase II

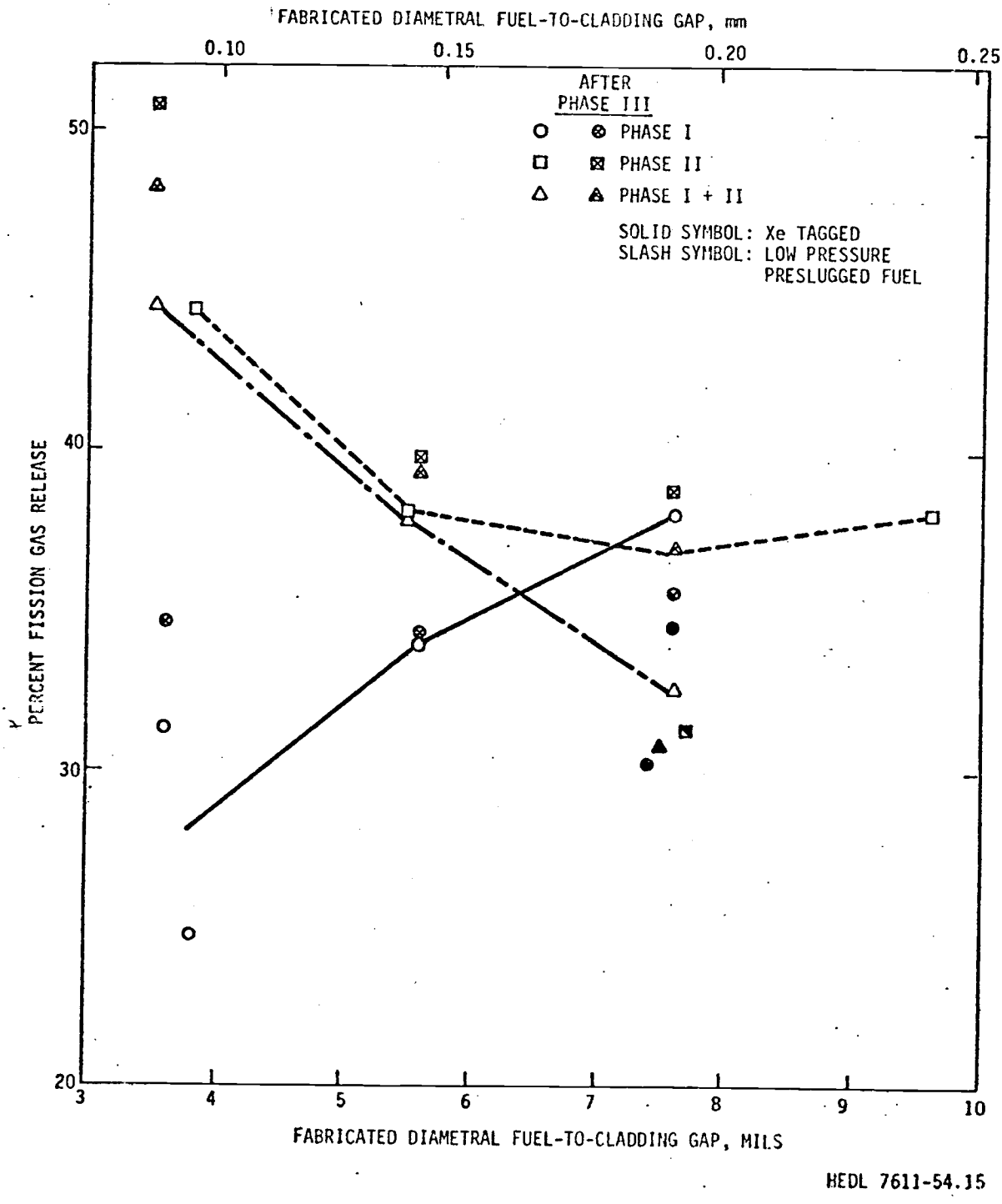

Figure C-7. Percent Fission Gas Release Found for HEDL P-20 Phase I and II Pins.

only" and Phase I plus II pins there is an unexpected increase in percent fission gas release in going from large to small original gaps.

The reason for this burnup dependent behavior no doubt lies partially with the results of data already reviewed. That is, see Figure C-8, the fuel temperatures, including the fuel centerline temperature (T_{ℓ}), appear at first (BOL) to be very dependent on fabricated gap size, fuel temperatures of pins fabricated with small gaps are less than ones fabricated with large gaps ($T_{\ell}^{S} < T_{\ell}^{L}$), which is substantiated by the measurements of columnar grain radii. After a short period of time however, the rapid gap closure brings all the gap sizes to about the same overall dimensions. Thus, the temperature drop across the gaps, ΔT_{GAP}, become very similar for all the pins. As further burnup occurs, the mechanism proposed in Reference 26 occurs. The fuel cracks and the cracks heal in the restructured zones moving part of the fuel-to-cladding gap volume to the central void. This forms central voids larger than possible just by densification of the columnar grain region and larger gaps lead to larger central voids. It is also noted that the columnar grain regions remain smaller in the small gap pins than in the large gap fuel pins. Since the gaps are now all about the same size, the temperature drop across them must be about the same and the drop across the fuel itself controls the fuel centerline temperatures. The fuel in the smaller gap has less restructuring so it could be running at higher centerline temperatures, ($T_{\ell}^{S} > T_{\ell}^{L}$) Figure C-8 (see Section B.5 of text).

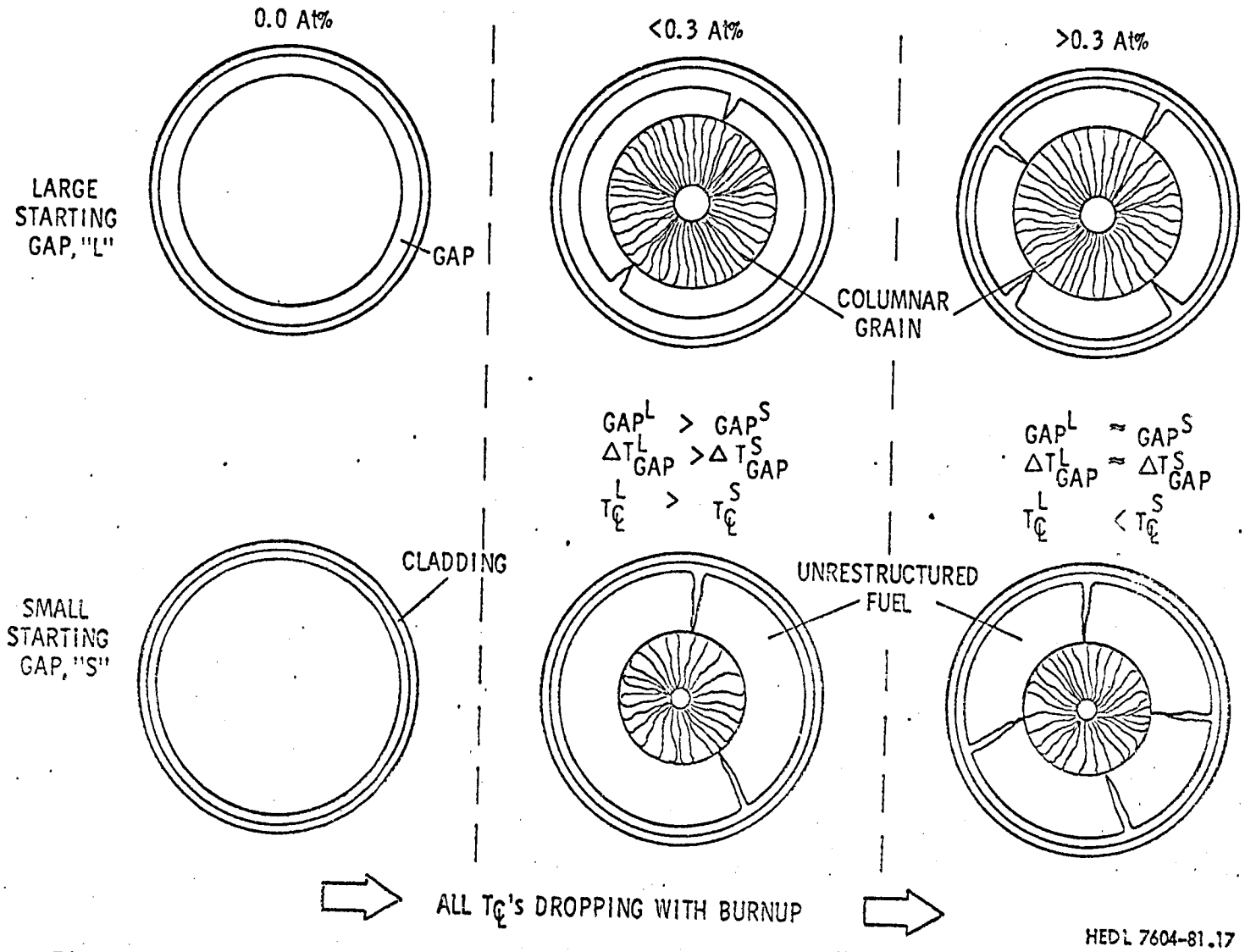

Figure C-8. Fuel and Temperature Behavior with Burnup.

All these mechanisms could lead to the small gap pins actually operating at higher fuel temperatures than the larger gap pins[C2]. Fuel smeared density[C3] and original gap size are then the actual controlling influences on fuel temperature after BOL operating; with fuel temperatures increasing with decreasing gap size and decreasing with decreasing smeared density. The opposite would be true at BOL. Thus, since gas release is expected to be time, grain structure and fuel temperature dependent, this drop in temperature in the large gap pins could cause the observed results. This concept of fuel temperature behavior is supported by the results of the measured extents of equiaxed grain regions all being about the same size for all the different gap sizes. The distance from the equiaxed grain boundary isotherm to the central void edge will be greater for small gap pins (i.e. smaller central void), suggesting higher centerline temperatures.

[C2]This same conclusion is noted in the text because of the behavior of the Phase I pins in Phase III (i.e. only the 0.0035 inch fuel-to-cladding ap pin melting while larger gap pins did not).

[C3]It is noted for these P-20 pins that a decrease in original fuel-to-cladding gap size means an increase in smeared density since there is a constant fuel pellet density. Smeared density has been shown to be the controlling factor in central void size(26). Lower smeared density leads to larger central voids and lower fuel centerline temperatures.

APPENDIX D

APPENDIX D

NOMINCLATURE

Table D-I Notation

Symbol	Description	Units
A	Average surface area at fuel-to-cladding gap	cm^2
A_C, A_F	Surface area of cladding and fuel, respectively, at the fuel-to-cladding gap	cm^2
A_1	Empirical constant relating α to surface roughness (H_S model)	$cm^{1/2}$
A_2	Empirical constant equal to $(A_1\bar{R}^{1/2})^{-1}$	cm^{-1}
a	Accommodation coefficient	--
a_{ij}	Accommodation coefficient for each surface (i = 1, 2) and each component (j = 1, 2, 3, 4, 5) making up the gas in the fuel-to-cladding gap	--
$\bar{a}$	Harmonic mean of accommodation coefficients at each surface ($\bar{a} = \frac{2a_1a_2}{a_1 + a_2}$)	--
B	Fitting parameter relating roughness to d_{CF} [$d_{CF} = Be^{DP} = C_1(R_C + R_F)$]	cm
Bu	Local fuel burnup (residual gap model)	$\frac{MWd}{kgM}$
b	Dimensionless constant in the brokaw gas mixture equation	--
C_1	Empirical constant relating surface roughness to d_{CF}	--

C_a	Constant of proportionality in accommodation coefficient model	--
C_p, C_v	Specific heat, at a constant pressure and volume, respectively, of the gas in the gap	$\frac{Cal}{gm - °K}$
$C_{p,Na}$	Specific heat of sodium at a constant pressure	$\frac{Cal}{gm - °K}$
$\overset{\alpha}{C}_{vj}$	Specific heat at a constant volume for each gas component (j = 1 to 5) of the gas in the fuel-to-cladding gap (per mole)	$\frac{Cal}{mole - °K}$
D	Fitting parameters associated with the decrease of d_{CF} with interface pressure	$\frac{cm^2}{dyne}$
D_e	Coolant equivalent diameter	cm
d_{CF}	Effective distance between fuel and cladding surfaces involved in heat transfer through the gas when surfaces are in "contact"	cm
d, Δd	Diameter, and change of a diameter in fuel due to thermal expansion	cm
F	Function dependent on surface roughness and waviness (H_S model)	--
G	Fabricated diametral fuel-to-cladding gap	mils, (cm)
G_p	Postirradiation diametral fuel-to-cladding gap at room temperature	mils, (cm)
g	Jump distance	cm

g_c, g_F	Jump distance at the cladding and fuel surfaces respectively	cm
H	Unit thermal conductance through fuel-to-cladding gap (gap conductance or gap coefficient)	$\frac{W}{cm^2\text{-}°C}$
H_{Con}	Unit thermal conductance at fuel-to-cladding gap due to convection	$\frac{W}{cm^2\text{-}°C}$
H_{eq}	Equivalent film coefficient, H_F, which accounts for test pins being encapsulated	$\frac{W}{cm^2\text{-}°C}$
H_F	Film coefficient between sodium coolant and cladding outside surface	$\frac{W}{cm^2\text{-}°C}$
H_G	Unit thermal conductance through gas in fuel-to-cladding gap	$\frac{W}{cm^2\text{-}°C}$
H_S	Unit thermal conductance through solid-to-solid contact at fuel-to-cladding gap	$\frac{W}{cm^2\text{-}°C}$
H_R	Unit thermal conductance due to radiant heat transfer between fuel and cladding	$\frac{W}{cm^2\text{-}°C}$
h	Myers' hardness of cladding	$\frac{dynes}{cm^2}$,(psi)
K	Boltzman constant	$\frac{Erg}{°K}$
k	Thermal conductivity	$\frac{W}{cm - °C}$
$\bar{k}$	Average thermal conductivity of gas in the fuel-to-cladding gap	$\frac{W}{cm - °C}$
k_C	Cladding thermal conductivity at inner surface	$\frac{W}{cm - °C}$
k_F	Fuel thermal conductivity at outer surface	$\frac{W}{cm - °C}$

k_G	Thermal conductivity of gas in fuel-to-cladding gap	$\frac{W}{cm - °C}$
k_M	Thermal conductivity of gas mixture	$\frac{W}{cm - °C}$
k_m	Harmonic mean of thermal conductivities of the fuel and cladding at the interface, $(k_m = \frac{2k_1k_2}{k_1 + k_2})$	$\frac{W}{cm - °C}$
k_{SM}	Thermal conductivity of gas mixture by simple mixing	$\frac{W}{cm - °C}$
k_{RM}	Thermal conductivity of gas mixture by reciprocal mixing	$\frac{W}{cm - °C}$
M_F	Mass flow rate of sodium coolant	$\frac{gm}{sec}$
M_G	Atomic mass of gas in fuel-to-cladding gap	$\frac{gm}{mole}$
M_i	Atomic mass of i'th type atom making up a wall molecule	$\frac{gm}{mole}$
M_W	Molecular mass of wall molecules	$\frac{gm}{mole}$
N	Exponent which may be pressure dependent (H_S model)	--
N_C	Number of full power reactor cycles	--
N_i	Number of atoms of atomic mass M_i making up wall molecule	--
Nu	Nusselt number (coolant - pin system)	--
n	Number of contact spots between fuel and cladding per unit area	--
O/M	Stoichiometry of the fuel	--
P	Apparent interface pressure between fuel and cladding	$\frac{Dynes}{cm^2}$

P_f	Fraction of porosity in the fuel	--
P_G	Pressure of gas in fuel-to-cladding gap	$\frac{\text{Dynes}}{\text{cm}^2}$
Pr	Prandtle number (coolant-pin system)	--
Q'	Linear heat rate or linear power	$\frac{\text{kW}}{\text{ft}}$, $(\frac{\text{W}}{\text{cm}})$
Q'_i	Linear heat rate or linear power at a specific axial location	$\frac{\text{kW}}{\text{ft}}$, $(\frac{\text{W}}{\text{cm}})$
Q'_m	Linear heat rate-to-incipient fuel melting ("power-to-melt")	$\frac{\text{kW}}{\text{ft}}$, $(\frac{\text{W}}{\text{cm}})$
Q'_1, Q'_2	Time-averaged local linear heat rate (1) and maximum local linear heat rate (2) respectively	$\frac{\text{kW}}{\text{ft}}$
q	Heat flow rate	W, $(\frac{\text{Btu}}{\text{hr}})$
q_v, q_{vb}	Volumetric heat generation in the unrestructured fuel (v) and the restructured fuel (vb) respectively.	$\frac{\text{W}}{\text{cm}^3}$
q_G, q_s, q_r, q_{con}	Heat flow rate through the gas, the contact points, radiant heat transfer, and convective heat transfer, respectively, at the fuel-to-cladding gap.	W, $(\frac{\text{Btu}}{\text{hr}})$
R	Mean gas constant	$\frac{\text{Cal}}{\text{gm} - {}^\circ\text{K}}$
$\bar{R}$	$(\frac{R_F^2 + R_C^2}{2})^{1/2}$	cm
R_a	Thermal resistance through contact a spot between fuel and cladding per unit area	$\frac{\text{cm}^2\text{-}{}^\circ\text{C}}{\text{W}}$
R_c, R_F	Arithmatic mean of surface roughness of the cladding and the fuel respectively.	cm

Re	Reynolds number (coolant-pin system)	--
r	Radius in the fuel	cm
r_b	Radius of columnar grain region OD	cm
r_c	Radius of cladding inner surface	cm
$r_{c,\ OD}$	Radius of cladding outer surface	cm
r_{cv}	Radius of central void in the fuel	cm
r_F	Radius of fuel outer surface	cm
r_M	Fabricated central void	cm
S_r, S_o	Integral of fuel conductivity at the radius r (at temperature T_r) and r_F (at temperature T_o), respectively, with respect to T	$\frac{W}{cm}$
T	Temperature	°C
$\bar{T}$	Average temperature of gas in the fuel-to-cladding gap	°C
T_a	Absolute temperature	°K
T_C	Temperature of cladding ID	°C
T_{CG}	Isotherm above which columnar grains form	°C
T_F	Temperature at the fuel outside surface	°C
T_I	Sodium coolant temperature	°C
T_{In}	Sodium coolant inlet temperature	°C
T_M	Melting temperature of fuel	°C
T_o	Temperature at the fuel outside surface	°C
T_r	Temperature at arbitrary radius in fuel	°C
ΔT_C	Temperature drop through cladding	°C
ΔT_F	Temperature drop through unrestructured fuel region	°C

ΔT_{Fl}	Temperature drop between the coolant and the cladding	°C
ΔT_G	Temperature drop between fuel and cladding	°C
ΔT_{RF}	Temperature drop through restructured fuel region	°C
W_{bC}, W_{bF}	Emissive power of a black body at the temperature of the cladding and fuel respectively	$\frac{W}{cm^2}$
$\bar{W}$	Average atomic weight of gas in the fuel-to-cladding gap	$\frac{gm}{mole}$
X	Thickness of material	cm
X_G	Hot radial fuel-to-cladding gap size	cm
x_i	Axial distance along fuel column	cm
X_i	Mole fraction of each component (i = 1, 2, 3, 4, 5) of gas making up the gas mixture in the fuel-to-cladding gap	--
y_C	Yield strength of cladding	$\frac{dynes}{cm^2}$, (psi)

α	Average radius of surface contact spots between fuel and cladding	cm
α_C, α_F	Thermal expansion of the cladding and fuel respectively.	$°C^{-1}$
ε	Characteristic energy in interaction of gas molecules, from Lennard Jones potential function	W-sec
ε_C, ε_F	Emissivity of the cladding and fuel surfaces respectively	--
γ	$\frac{C_p}{C_v}$	--
$\gamma_1, \gamma_2, \gamma_3$	Fitting coefficients for pure gas models	--
μ	Absolute vescosity of the gas	$\frac{gm}{cm\text{-}sec}$
Ω	Mean free path of gas molecules	cm
Ω_k	Collision integral dependent on the dimensionless temperature KT/ε	--
ρ	Fraction of fuel theoretical density (TD) in fabricated fuel	--
ρ_{CG}	Fraction of fuel theoretical density (TD) in columnar grain zone	--
σ	Stefan Boltzman constant	$\frac{W}{cm^2\text{-}°K^4}$
σ_L	Characteristic diameter from Lennard-Jones potential function	cm

τ_0, τ_1	Temperature of gas molecule on surface of a solid body at temperature τ	°C
τ_2	Temperature of gas molecule after striking solid body	°C
Θ_i, Θ_r	Angle of incident (i) and reflection (r)	°
Θ_j (j=1 to 6)	Fitting coefficients for residual fuel-to-cladding gap model	--

Table D-II Description of Selected Terms and Names

Term	Description
Power-to-Melt (Q'_m)	The linear heat rate needed-to-cause the centerline of the fuel to be just at the fuel melting temperature. The linear heat rate-to-cause incipient fuel melting.
Linear Heat Rate	The heat rate or power produced at a location in the fuel, if it is assumed there is a unit length of the fuel operating at this power level (example of units: kW/ft).
Diametral Fuel-to-Cladding Gap	The cladding tube inside surface diameter minus the fuel outside surface diameter. This is used instead of radial gap, to avoid confusion with observations where the radial gap may vary around the circumference because the fuel is not centered within the cladding ID.
Fuel Burnup	A measure of fuel consumption by fissioning. It can be described as a (1) percent of fuel atoms that have undergone fission (atom percent burnup, At%) or (2) the amount of energy produced per unit weight of fuel present (megawatt days per metric tonne of fissionable metal, MWd/MTM).

	Thus burnup is a function of the length of time of operation and the power level during that time.
Fission	The splitting of a heavy nucleus (i.e. ^{235}U) into two approximately equal parts (which are nuclei of lighter elements), accompanied by the release of a relatively large amount of energy ($\sim$ 200 Mev) and generally one or more neutrons.
Fission Products	The nuclei (fission fragments) formed by fission of heavy elements (i.e. ^{235}U), plus the nuclides formed from the fission fragments' radioactive decay.
Fast Flux	A neutron flux made up of neutrons with energies greater than .1 Mev.
Breeder Reactor	A fission type reactor that produces more fissionable material than it consumes.
LMFBR's	Liquid Metal Fast Breeder Reactors are liquid metal cooled (in this case with sodium) breeder type fission reactors characterized as having a fast (high energy) neutron flux. The LMFBR produces heat from the fissioning process, that can be used to generate electricity, and generates more fissionable material

than it uses.

FFTF	The Fast Flux Test Facility is under construction near Richland, Washington. This will be the primary test installation in the United States LMFBR program. Its normal power level will be 400 MW thermal.
EBR-II	The Experimental Breeder Reactor Number Two is located in Idaho Falls, Idaho. It is a smaller sodium cooled fast flux reactor used for present irradiation of LMFBR fuels and materials. Its normal operating power is 60 MW thermal.
HEDL	Hanford Engineering Development Laboratory operated by the Westinghouse Hanford Company for the U. S. Energy Research and Development Administration (ERDA).